รายงานวิจัยฉบับสมบูรณ์

โครงการ

เอพิแทกซีวิวิธพันธุ์และจุดบกพร่อง : การศึกษาพื้นฐานจากรอยกัดของละอองโลหะที่วิ่งด้วยตนเอง

Heteroepitaxy and dislocations: fundamental studies using self-running droplets trails

โดย รองศาสตราจารย์ ดร.ทรงพล กาญจนชูชัย และคณะ

เมษายน ๒๕๖๑

สัญญาเลขที่ RSA5880049

รายงานวิจัยฉบับสมบูรณ์

โครงการ

เอพิแทกซีวิวิธพันธุ์และจุดบกพร่อง : การศึกษาพื้นฐานจากรอยกัดของละอองโลหะที่วิ่งด้วยตนเอง

Heteroepitaxy and dislocations: fundamental studies using self-running droplets trails

ผู้วิจัย

รศ.ดร. ทรงพล กาญจนชูชัย

และคณะ

สังกัด

คณะวิศวกรรมศาสตร์

จุฬาลงกรณ์มหาวิทยาลัย

สนับสนุนโดยสำนักงานกองทุนสนับสนุนการวิจัยและจุฬาลงกรณ์มหาวิทยาลัย

(ความเห็นในรายงานนี้เป็นของผู้วิจัย สกว. และจุฬาลงกรณ์มหาวิทยาลัย ไม่จำเป็นต้องเห็นด้วยเสมอไป)

สารบัญ

กิตติกรรมประกาศ 1
บทคัดย่อ 2
Abstract 3
Executive Summary 4
เนื้อหางานวิจัย 5
1. ปีที่ 1 5
2. ปีที่ 2 6
3. ปีที่ 3 6
Output 7
ภาคผนวก 1 8
ภาคผนวก 2 17
ภาคผนวก 3 33

กิตติกรรมประกาศ

โครงการวิจัย เอพิแทกซีวิวิธพันธุ์และจุดบกพร่อง : การศึกษาพื้นฐานจากรอยกัดของละอองโลหะที่วิ่งด้วยตนเอง (Heteroepitaxy and dislocations: fundamental studies using self-running droplets trails) ตามสัญญาเลขที่ RSA5880049 ระยะเวลาดำเนินโครงการไม่เกิน 3 ปี นับตั้งแต่วันที่ 1 กรกฎาคม พ.ศ. 2558 ถึง 30 มิถุนายน พ.ศ. 2561 ได้รับเงินทุนทั้งสิ้น 1.5 ล้านบาท (จาก สกว. 750,000 บาท จากจุฬาฯ 750,000 บาท) ผลจากโครงการได้รับการตีพิมพ์ในวารสารวิชาการระดับนานาชาติ 3 บทความ

โครงการนี้ได้รับการสนับสนุนจากหลายฝ่าย ข้าพเจ้าขอขอบคุณ สกว. จุฬาลงกรณ์มหาวิทยาลัย คณะวิศวกรรมศาสตร์ ภาควิชาวิศวกรรมไฟฟ้า และสถาบันวิจัยแสงซินโครตรอน (องค์การมหาชน) สำหรับทุนวิจัย เครื่องมือ อุปกรณ์ และสถานที่ ขอขอบคุณบุคลากรจาก 1) ห้องปฏิบัติการวิจัยสิ่งประดิษฐ์สารกึ่งตัวนำ ได้แก่ ศาสตราจารย์ ดร.สมศักดิ์ ปัญญาแก้ว ศุภโชค ไทยน้อย ขวัญเรือน ไทยน้อย พรชัย ช่างม่วง และพัฒนา พันธุวงศ์ และ 2) ระบบลำเลียงแสง 3.2Ub ได้แก่ ดร.ชนรรค์ เอื้อรักสกุล ดร.พัฒน์ โพธิ์ทองคำ ดร.วุฒิไกร บุษยากร และทิพย์อุษา วงศ์พินิจ ที่ให้ความกรุณาและช่วยเหลือข้าพเจ้าและนิสิตในที่ปรึกษาโดยตลอด

ทรงพล กาญจนชูชัย

บทคัดย่อ

รหัสโครงการ : RSA5880049

โครงการ : เอพิแทกซีวิวิธพันธุ์และจุดบกพร่อง : การศึกษาพื้นฐานจากรอยกัดของละอองโลหะที่วิ่งด้วยตนเอง

นักวิจัย : รศ.ดร.ทรงพล กาญจนชูชัย และคณะ จุฬาลงกรณ์มหาวิทยาลัย

E-mail Address : songphol.k@chula.ac.th

ระยะเวลาโครงการ : 1 กรกฎาคม พ.ศ. 2558 ถึง 30 มิถุนายน พ.ศ. 2561

โครงการวิจัยมีวัตถุประสงค์เพื่อศึกษาว่า ดิสโลเคชันที่อินเตอร์เฟสของชิ้นงานที่สังเคราะห์โดยวิธีเอพิแทกซีวิวิธพันธุ์นั้นมีอิทธิพลอย่างไรต่อละอองโลหะบนผิวของแผ่นฐานสารกึ่งตัวนำ อาศัยตำแหน่งปัจจุบันและร่องรอยการเดินทางของละอองเป็นเครื่องมือในการศึกษาประวัติและลักษณะสมบัติของดิสโลเคชัน ผลการศึกษาทำให้เข้าใจวิวัฒนาการและสัณฐานของโครงสร้างระดับไมโครและนาโนเมตรบนผิวสารกึ่งตัวนำตระกูล III-V ต่าง ๆ หลายประการอันรวมถึง ๑. การคลายตัวของชั้นอินเดียมอาร์เซไนด์ที่บางมากบนสนามความเครียดลายตารางที่ปลูกโดยวิธีเอพิแทกซีวิวิธพันธุ์ ๒. การควบคุมการไหลของโครงสร้างลวดและรอยกัดระดับนาโนเมตรบนผิวระนาบ (110) อาศัยอนุภาคนาโน และ ๓. อันตรกิริยาระหว่างดิสโลเคชันที่อินเตอร์เฟสกับละอองโลหะที่กำลังเคลื่อนที่ด้านบน นำไปสู่การเคลื่อนที่ของละอองที่หักเลี้ยวในลักษณะเดียวกับลายตารางอันเป็นแบบรูปพื้นฐานของวงจรรวมทุกชนิด ความเข้าใจระดับพื้นฐานนี้จะนำไปสู่การพัฒนาสารประกอบกึ่งตัวนำทั้งชนิดใหม่และปัจจุบันที่ใช้กันแพร่หลายในอุตสาหกรรมโฟโตนิกส์และออปโตอิเล็กทรอนิกส์

คำหลัก : เอพิแทกซีวิวิธพันธุ์ ดิสโลเคชัน ละออง สารกึ่งตัวนำ

Abstract

Project Code : RSA5880049

Project Title : Heteroepitaxy and dislocations: fundamental studies using self-running droplets trails

Investigator : Songphol Kanjanachuchai et al., Chulalongkorn University

E-mail Address : songphol.k@chula.ac.th

Project Period : 1 July 2015 – 30 Jun 2018

The project aims to study the interfacial dislocations (formation and characteristics) in heteroepitaxy when the epilayers are strained, using self-running droplets and trails as a guide to the history and character of the dislocations. Several key issues regarding the structural evolution and morphology of micro and nanostructures on various III-V semiconductor surfaces are identified and explained. These include i) the relaxation of ultrathin heteroepitaxial InAs layer on cross-hatch stress fields, ii) the controlled growth of nanoscale wires and grooves from self-running droplets on (110)-oriented surface using nanoparticles, and iii) the interaction between interfacial dislocations and self-running droplets that result in droplets running and turning in cross-hatched pattern basic to all integrated circuits. These fundamental understandings will add to the development of existing and novel compound semiconductors prevalent in photonics and optoelectronics industries.

Keywords : Heteroepitaxy, dislocations, droplets, semiconductors

Executive Summary

ฟิล์มบางสารกึ่งตัวนำที่ปลูกบนบนแผ่นฐานที่มีค่าคงตัวแลตทิซไม่เท่ากันโดยเทคนิคเอพิแทกซีวิวิธพันธุ์มักเกิดดิสโลเคชันอันเป็นสิ่งไม่พึงประสงค์ โดยเฉพาะหากเกิดใกล้บริเวณไวงาน อย่างไรก็ตาม หากดิสโลเคชันเกิด ณ บริเวณที่ไกลจากบริเวณไวงาน ก็จะมีประโยชน์แก่การศึกษาระดับพื้นฐานในหลายแง่มุม เช่น การศึกษาเกี่ยวกับอิทธิพลที่ดิสโลเคชันมีต่อการก่อตัวของชั้นที่บางในระดับอะตอม (ภาคผนวก 1) หรืออิทธิพลที่มีต่อการก่อกำเนิดการนำทาง หรือการขัดขวางการเคลื่อนที่ของละอองโลหะที่ขับเคลื่อนด้วยตนเองบนผิวสารกึ่งตัวนำตระกูล III-V ระหว่างการระเหิด (ภาคผนวก 3) หากระหว่างการระเหิด มีอนุภาคนาโนอยู่บนพื้นผิว อนุภาคฯ จะเร่งให้วัสดุสลายตัวเร็วขึ้นโดยอนุภาคฯ จะถูกกำจัดออกไปและถูกแทนที่โดยลวดโลหะและหลุมที่ถูกกัดเป็นเส้น กว้างในระดับนาโน (ภาคผนวก 2) แม้โครงการวิจัยนี้มิได้มีผลงานในระดับอุปกรณ์ที่พร้อมใช้งาน แต่ผลงานวิจัยก็ได้เผยให้เห็นถึงโครงสร้างนาโน สัณฐาน และพลวัตที่ใหม่หลายประการอันเป็นประโยชน์ต่อการผลิตวงจรรวมในอนาคตซึ่งอาจสร้างโดยกลไกประกอบตนเอง

Heteroepitaxy of semiconductor films on lattice-mismatched substrates often results in dislocations which are undesirable, particularly when they occur near device active areas. However, their presence away from active device areas prove to be useful in certain aspects of fundamental studies. For examples, they are able to influence the formation of complex ultrathin layers (Appendix 1), the nucleation, guiding, and blocking of self-propelled droplets on III-V surfaces during incongruent evaporation (Appendix 3). When nanoparticles are present on the surface, they accelerate material decomposition and play a sacrificial role in the nucleation of nanowires and nanogrooves (Appendix 2). Though no functioning devices are demonstrated, this project reveals many novel nanostructures, morphologies and dynamics which may serve as a fabrication route toward future self-integrated circuits.

เนื้อหางานวิจัย

เนื้อหางานวิจัยตลอดระยะเวลา 3 ปีของโครงการสามารถอธิบายตามลำดับได้ดังนี้

1. ปีที่ 1

ชั้นฟิล์มบางอินเดียมอาร์เซไนด์ (InAs) ที่ปลูกลงบนผิวลายขีดไขว้ InGaAs/GaAs มีการเปลี่ยนแปลงสภาพหลังปลูกหลายลักษณะซึ่งนำไปสู่โครงสร้างผิวในแบบต่าง ๆ ตั้งแต่ลวดควอนตัมที่เรียงเป็นแนวเดียวกัน ไปถึงควอนตัมด็อต และพีระมิดที่สูงเป็นไมครอน รูปร่างต่าง ๆ เหล่านี้เกิดจากผลของการแข่งขันระหว่างการแพร่อะตอมที่ไม่สมมาตร สนามความเครียดจากพื้นผิวด้านล่าง และความพยายามในการลดพลังงานรวมของระบบ ลักษณะผิวต่าง ๆ ที่ค้นพบแสดงให้เห็นถึงสถานะกึ่งเสถียรระหว่างสถานะสองและสามมิติอันอาจนำไปสู่อุปกรณ์ใช้งาน เช่น เซนเซอร์ หรืออาจใช้เป็นเครื่องมือในการศึกษาพื้นฐานของระบบควอนตัม

หลังจากการสังเคราะห์โครงสร้าง GaAs/LM-InGaAs บนแผ่นฐาน GaAs ทีมวิจัยได้ศึกษาประเด็นต่อไปนี้

1) การผ่อนคลายความเครียดของชั้นฟิล์มที่บางกว่าความหนาวิกฤต (subcritical thickness) โดยการแอนนีล (ก่อนการ decompose เพื่อให้เกิด running droplets) ในระบบปลูกผลึกด้วยลำโมเลกุล (MBE)

2) ปรากฏการณ์ self-running droplets โดยเทคนิค LEEM ที่สถาบันวิจัยแสงซินโครตรอน (SLRI) ช่วง 20-25 ธค. 2558 (samples: CHP151210B, CHP151217A) และ 6-10 มิย. 2559 (samples: CHP160325, CHP160423)

ผลจากประเด็น 2) นำไปสู่การวางแผนทดลองเพิ่มเติมซึ่งได้ดำเนินการในปีที่ 3

ผลจากประเด็น 1) หรือโครงสร้าง GaAs/LM-InGaAs บนแผ่นฐาน GaAs โดยการ anneal ได้ข้อสรุปกล่าวคือ การปลูกผลึกและการ anneal นำไปสู่โครงสร้าง quantum wire และ pyramids ที่น่าสนใจ โดยเฉพาะ quantum wire ที่มีบทประยุกต์ต่อวงจร quantum ขนาดเล็ก โครงสร้าง wire และ pyramids เป็นผลจากการแข่งขันของกลไก 3 ชนิด ได้แก่

ก. การผ่อนคลายความเครียดเพื่อลดพลังงานรวมของชั้นเอพิ (epilayer) เอง

ข. การที่อะตอมกลุ่ม III เคลื่อนที่ในทิศ [1-10] ได้เร็วกว่าในทิศ [110] ซึ่งตั้งฉากกัน และ

ค. สนามความเครียดจากจุดบกพร่องด้านล่าง (interfacial dislocations) ที่โน้มน้าวอะตอมผิวให้เคลื่อนตัวไปในทิศที่มันต้องการ

ผลการทดลองโดยละเอียดปรากฏดัง **ภาคผนวก 1**

2. ปีที่ 2

ในปีที่ 2 การทดลองถูกออกแบบใหม่โดยมุ่งหวังที่จะอธิบายการก่อ nanowire และ nanochannel อันเป็นผลจากปรากฏการณ์ running droplet บนผิวระนาบ (110) ของสารประกอบกึ่งตัวนำ III-V ต่าง ๆ ดังต่อไปนี้

1) ผิว GaAs, InAs, InP แบบ epiready

2) ผิว InP ที่ปกคลุมโดยอนุภาคนาโนทองคำ (Au nanoparticles, AuNPs)

ผลการทดลองแสดงให้เห็นว่า การระเหิดผิวสารกึ่งตัวนำภายใต้ภาวะสุญญากาศ นอกจากจะทำให้เกิด droplets แล้ว ยังอาจทำให้เกิด nanowire บนผิวบางชนิดได้ด้วย กลไกการเกิด nanowire ที่พบนั้นแตกต่างโดยสิ้นเชิงจากกรรมวิธีการผลิต nanowire แบบอื่น ประเด็นสำคัญที่เป็นผลโดยตรงจากงานวิจัยนี้ได้แก่

ก. ผิว GaAs(110) ที่กำลังระเหิดทำให้เกิดหลุมรูปตัว V ซึ่งสะสม Ga เหลวถึงจุดหนึ่งจะขับ Ga เป็นเส้นยาวออกมา เส้นดังกล่าวยาวหลาย 10 μm แต่แคบในระดับ 100 nm จึงเรียกลวดนาโน (nanowire)

ข. ผิว InAs(110) ที่กำลังระเหิดก็สามารถให้ nanowire ได้เช่นกัน แต่ผิว InP(110) นั้นไม่สามารถให้ nanowire ได้เนื่องจากมีผิวหลังระเหิดที่เรียบมาก

ค. ผิว InP(110) ที่เรียบมากนั้นอาจทำให้ขรุขระขึ้นอาศัย AuNPs ซึ่งจะถูกสลายไปในการขุดเจาะผิวก่อนที่จะนำไปสู่การก่อ nanowire ในที่สุด

ผลการทดลองโดยละเอียดปรากฏดัง **ภาคผนวก 2**

3. ปีที่ 3

ปีที่ 3 เป็นการทดลอง self-running droplets (ณ SLRI จ. นครราชสีมา) ที่ต่อยอดจากปีที่ 1 อาศัยวัสดุที่ได้สังเคราะห์เพิ่มเติมช่วงปีที่ 2 โดยเทคนิค MBE (ณ SDRL จุฬาฯ) การทดลองมีวัตถุประสงค์หลัก 2 ประการ

1) เพื่อศึกษารายละเอียดเชิงตำแหน่ง คือ ตำแหน่งการก่อตัวของละอองโลหะหมู่ III ขณะที่ผิวหน้าระเหิด

2) เพื่อศึกษาพลวัต คือ พฤติกรรมของละอองขณะที่เคลื่อนที่ผ่านดิสโลเคชันแบบต่าง ๆ

ผลการทดลองแสดงให้เห็นว่า โครงข่ายมิสฟิตดิสโลเคชันมีผลทั้งต่อตำแหน่งตั้งต้นของการก่อละอองโลหะและผลกระทบต่อการเคลื่อนที่ของละอองหลังจากที่ละอองโลหะเคลื่อนที่ออกจากตำแหน่งก่อตัว เราพบลักษณะการเคลื่อนที่ของของเหลวที่ไม่สามารถพบเห็นทั่วไป เช่น การเลี้ยวแบบหักศอกเป็นมุม 90 หรือแม้กระทั่งการสะท้อนกลับเป็นมุม 180 ทิศทางเคลื่อนที่ดังกล่าวสามารถอธิบายได้ในเชิงคุณภาพอาศัยปัจจัยต่าง ๆ ดังนี้

ก. สนามความเครียดอันเนื่องจากโครงข่ายดิสโลเคชันที่ฝังอยู่ใต้ละออง ณ ระนาบอินเตอร์เฟสระหว่างแผ่นฐาน GaAs และชั้นเฮเทอโรเอพิแทกซี InGaAs

ข. แรงขับเคลื่อนจากศักย์เคมีและเกรเดียนต์ของความเครียดอันเป็นบ่อเกิดของการไหลแบบมาแรงโกนี

ปรากฏการณ์ข้างต้นอาจมีประโยชน์ต่อกระบวนการหลิตหรืออุปกรณ์อิเล็กทรอนิกส์ที่ใช้ละอองโลหะเป็นสารตั้งต้นหรือเป็นตัวเร่งปฏิกิริยา เช่น เทคนิคเอพิแทกซีละอองสำหรับการสร้างโครงสร้างควอนตัมนาโน เทคนิค VLS สำหรับปลูกนาโนไวร์หรือการสร้างวงจรรวมที่สามารถประกอบตนเอง

ผลการทดลองโดยละเอียดปรากฏดัง **ภาคผนวก 3**

Output

Output ของโครงการคือบทความวิจัยในฐานข้อมูล ISI (Clarivate Analytics) 3 บทความ ได้แก่

1. W. Eiwwongcharoen, N. Nakareseisoon, S. Thainoi, S. Panyakeow, **S. Kanjanachuchai**, "Ultrathin epitaxial InAs layer relaxation on cross-hatch stress fields," *CrystEngComm* **18**, 5852 (2016). **ภาคผนวก 1**
2. **S. Kanjanachuchai** and P. Photongkam, "Planar Self-Assembly of Submicron and Nanoscale Wires and Grooves on III–V(110) Surfaces", *Crystal Growth & Design* **17**, 4413-4421 (2017). **ภาคผนวก 2**
3. **S. Kanjanachuchai**, T. Wongpinij, S. Kijamnajsuk, C. Himwas, S. Panyakeow, P. Photongkam, "Preferential nucleation, guiding, and blocking of self-propelled droplets by dislocations", *Journal of Applied Physics* **123**, 161570 (2018). **ภาคผนวก 3**

ภาคผนวก 1

CrystEngComm

PAPER

Cite this: *CrystEngComm*, 2016, **18**, 5852

Ultrathin epitaxial InAs layer relaxation on cross-hatch stress fields

Win Eiwwongcharoen, Nitas Nakareseisoon, Supachok Thainoi, Somsak Panyakeow and Songphol Kanjanachuchai*

Received 13th May 2016,
Accepted 21st June 2016

DOI: 10.1039/c6ce01127f

www.rsc.org/crystengcomm

Thin, highly-strained InAs layers epitaxially grown on GaAs/InGaAs cross-hatch surfaces undergo postgrowth transformations that yield several morphologies ranging from aligned quantum wires to quantum dots and micron-scale pyramids. The shape varieties result from the multiple pathways created from the combined/competitive effects of asymmetric adatom diffusions, subsurface stress fields and misfit energy minimization. These morphologies reveal the multiple outcomes of metastable states between the two- and the three-dimensional transition that if properly captured and engineered may open up new windows of opportunities both in devices such as sensors and in fundamental quantum studies.

Introduction

Strain relaxation in epilayers during lattice-mismatched heteroepitaxy plays a central role in the growth and engineering of III–V single crystals—an important class of optoelectronic material. III–V nanostructures such as InGaAs quantum dots (QDs) and quantum wells are almost always embedded in a wider bandgap material, enabling the fabrication of near-infrared devices such as lasers and diodes.[1,2] The reliability of these devices is due largely to the fact that the nanostructures are capped. Uncapped nanostructures such as surface QDs, on the other hand, suffer from sudden crystal termination and the unavoidable presence of dangling bonds which act as non-radiative recombination centres, making surface QDs much less optically active than buried QDs.[3] These crystalline imperfections need not be detrimental nor prevent applications, however. Using stacked structures, Liang *et al.* found that it is possible for carriers to transfer from buried QDs to surface QDs, increasing the luminescence efficiency of the latter.[4] Ajlani *et al.* in contrast capped surface QDs with graphene and evidenced an electron transfer mechanism from graphene to QDs which similarly increases the optical efficiency of the latter.[5] Even water molecules in air can passivate some of the dangling bonds, allowing uncapped InGaAs nanostructures to be used as a humidity sensor.[6] When surface functionalized, InAs QDs can exhibit optical properties that respond to the biochemical characteristics of the functional groups.[7,8] These examples indicate that surface III–V nanostructures can sense and detect ions and molecules in a similar fashion to silicon-based, ion-sensitive field-effect transistors,[9] and possibly with greater responsivity and optical output due to the higher electron mobility and the direct bandgap nature, respectively. The sensing characteristics of these surface III–V nanostructures would depend on the structural parameters that most affect the quantized states of the confined carriers: size, shape and strain.

The existing literature on surface III–V nanostructures is dominated by InAs/GaAs QDs—InAs QDs on GaAs (001) substrates—formed *via* Stranski–Krastanow growth mode when the two-dimensional (2D) equivalent thickness of the InAs epilayer θ exceeds a critical thickness θ_c of approximately 1.7 monolayer (ML). For optical applications, InAs/GaAs QDs are grown up to $\theta \approx 1.7$–2.5 ML, resulting in InAs QD ensembles with a typical QD size of 30 nm in diameter and 8 nm in height.[10] If $\theta \gg 2.5$ ML, strain relaxation is incoherent, dislocations emerge, and the QDs would be optically inactive.[11] If $\theta < 1$ ML, no relaxation occurs as the submonolayer can accommodate all the misfit. This leaves the InAs epilayers with two thickness regions which are optically active and with the possibilities of morphological control: the thin ($\theta_c < \theta < 2.5$ ML) and the ultrathin (1 ML $< \theta < \theta_c$) regions. While it is generally accepted that growth in the thin region always results in QDs, growth in the ultrathin region is much less investigated and somewhat controversial as it yields several possible morphologies. Platelets, wires and even QDs[12–15] have been reported—an indication that the ultrathin region is highly sensitive to growth conditions, making morphological control difficult, limiting potential applications that take advantage of surface-sensitive properties.

Here, we report the first attempt to control the morphology of ultrathin InAs layers *via* strain engineering. Using InGaAs/GaAs cross-hatch pattern (CHP) templates which

Semiconductor Device Research Laboratory, Department of Electrical Engineering, Faculty of Engineering, Chulalongkorn University, Bangkok 10330, Thailand. E-mail: songphol.k@chula.ac.th; Fax: +66 22186523; Tel: +66 22186524

form as a result of interfacial misfit dislocations, we grow ultrathin InAs layers on InGaAs/GaAs CHPs, let the 2D epilayers relax, and find a multitude of quasi-one- and three-dimensional morphologies ranging from near-parallel wires to platelets to pyramids with heights in discrete atomic steps. The origins of these rich morphologies are explained in terms of competitive effects between asymmetric adatom diffusions, subsurface stress fields and misfit energy minimization.

Experimental

Ultrathin InAs films are grown on epi-ready GaAs (001) ± 0.5° substrates by solid-source molecular beam epitaxy (MBE) with real-time surface monitoring by reflection high-energy electron diffraction (RHEED). Starting from *in situ* oxide desorption of the GaAs substrate at 610 °C, the substrate temperature T_{sub} is reduced to 580 °C for the growth of the 300 nm GaAs planarizing layer. T_{sub} is then further reduced to 500 °C in order to grow the 25 nm $In_{0.2}Ga_{0.8}As$ CHP layer, followed by the 6 nm GaAs spacer layer, and the ultrathin InAs layer at 470 °C. The thin GaAs spacer not only serves as a strain adjusting layer but also prevents In from the CHP to reach the growing surface. These ensure that the critical thickness θ_c is not affected by the CHP.[16] Two sets of samples are grown. Each set comprises three samples having different InAs layer thicknesses (θ = 1.4, 1.5, 1.6 ML). The two sets are grown identically up to the ultrathin InAs layer. After the required thickness is reached, the samples in one set (referred to hereafter as set A) are quenched, while those in the other set (B) are annealed at the same T_{sub} of 470 °C for 4 min 30 s under an As beam equivalent pressure (BEP) of 8×10^{-6} torr. Throughout growth and during postgrowth annealing, the RHEED pattern is streaky, a characteristic typically taken to indicate that the three-dimensional (3D) structure, particularly QDs, is absent or negligible, and that the surface is "flat". RHEED is thus insensitive to surface changes in the ultrathin regions investigated here. After cooling to below 100 °C, the sample is removed; its surface is characterized by tapping-mode atomic force microscopy (AFM) in air using a probe whose tip radius is smaller than 10 nm. Optical characterization by photoluminescence (PL) is carried out using the excitation from the 5145 Å line of Ar^+ laser. The optical signal is dispersed by a grating spectrometer (Horiba iHR320) and detected using a cooled (77 K) InGaAs photodiode using standard lock-in detection.

Results and discussion

The relaxation of ultrathin InAs layers is strongly affected by the underlying CHP layers and the annealing conditions. The orthogonal dislocations making up the CHPs influence material distribution around them while the longer annealing times allow surface flattening and the formation of quasi-periodic quantum wires whose periodicity is dictated by the epilayer thickness. Detailed surface morphologies of sets A (quenched) and B (annealed) samples are discussed in sequence as follows.

A. Morphologies of quenched, ultrathin InAs layers

Set A samples are quenched the instant the ultrathin InAs layers reach the desired thicknesses. The morphologies of as-grown 1.4-, 1.5- and 1.6-ML InAs are shown in the 5×5 μm^2 AFM images in Fig. 1a–c, respectively, and the 2×2 μm^2 images in Fig. 1d–f, respectively. The morphologies of the three samples are similar and can be described as elongated, semi-ordered platelets with sporadic discontinuities along the [110] and [1$\bar{1}$0] directions. The elongation of all InAs platelets in the [1$\bar{1}$0] direction is a general result of greater mobility of III atoms (In) on III–V surfaces grown under V-rich conditions, and thus is a prominent feature of all surface structures in this work.

A typical platelet is bounded by a 1 ML (a/2, where a = 0.606 nm is the lattice constant of InAs) or a 2 ML step. A platelet may be free-standing, having distinct boundaries as exemplified by platelet *i* in Fig. 1a, or it can have fuzzy/wavy boundaries as exemplified by platelet *ii*. Cusps can be seen at the boundaries of many platelets (see Fig. 1d and e). Since cusps are less energetically favourable than curved terraces (see Fig. 1f), the existence of cusps is thus an indication of coalescent events just before or during quenching.

Platelet coalescence predominantly occurs in the [110] and [1$\bar{1}$0] directions and can be qualitatively explained by the schematic drawings in Fig. 2 which classify coalescent events into three types. One, lengthwise coalescence (in the [1$\bar{1}$0] direction) as shown in Fig. 2a leads to elongation and thus a final platelet with increased aspect ratio. Examples of platelets that form as a result of lengthwise coalescence are platelets *i* and *ii* in Fig. 1a, and P1 and P2 in Fig. 1d. Two, widthwise coalescence (in the [110] direction) as shown in Fig. 2b leads to widening and thus a final platelet with reduced aspect ratio. An example of widthwise coalescence is platelet *iii* in Fig. 1a; its width is approximately twice those of platelets *i* and *ii*. Three, oblique coalescence as shown in Fig. 2c leads to cusps or, given sufficient time and energy, curved edges. Curved ML steps are prevalent in samples which have been subject to long annealing times.[17] Some of the cusps and curved edges are pointed out in Fig. 1d–f. The three types of coalescence can describe the morphologies of all platelets, though those that reside in the vicinity of dislocation lines will inevitably be modified by dislocation-related stress fields to be described later.

The average platelet size increases as the epilayer thickness θ increases from 1.4 ML in Fig. 1a and d to 1.5 ML in Fig. 1b and e but decreases slightly as θ reaches 1.6 ML in Fig. 1c and f. The platelets in Fig. 1a and d are elongated: the size in the [1$\bar{1}$0] direction is ~0.5–1 μm but in the [110] direction is much smaller at ~0.1–0.2 μm, giving platelets an aspect ratio of 3–10. The average platelet width when θ = 1.4 ML is ~150 nm (see the marker in Fig. 1d), indicating that the platelets grow in the step flow mode as the average

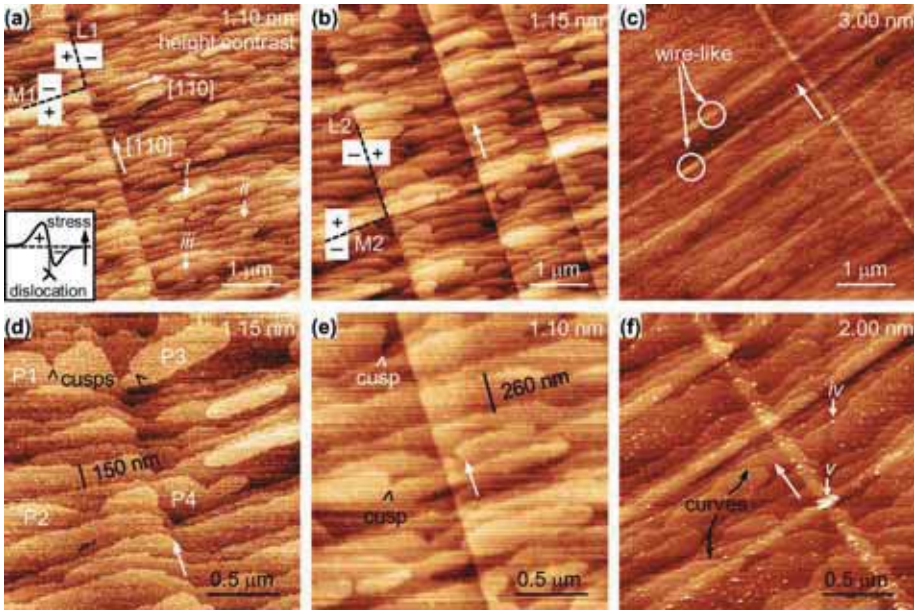

Fig. 1 AFM images of quenched, ultrathin InAs layers on cross-hatch pattern templates as InAs thickness increases from (a, d) 1.4 ML to (b, e) 1.5 ML and (c, f) 1.6 ML. The white arrows, unless otherwise stated, point in the [110] direction. The surface is populated by platelets that accumulate (denoted +) on one side and deplete (–) from the other side of [110] dislocation lines L*n* and [1$\bar{1}$0] dislocation lines M*n* where *n* is 1 in (a) or 2 in (b). The inset in (a) plots a typical surface stress profile due to a buried dislocation.

platelet width is close to pre-existing surface steps which for a substrate miscut of 0.1° are spaced approximately 150 nm apart. As θ increases from 1.4 to 1.5 ML, the average platelet widens to ~260 nm (see the marker in Fig. 1e). Platelets tend to expand in plane instead of out of plane which would increase the heights. In-plane expansion mostly occurs widthwise, *i.e.* in the [110] direction as schematized in Fig. 2b. As θ further increases to 1.6 ML, however, the average platelet slightly shrinks as seen in Fig. 1c and f. This is a direct result of material redistribution at the onset of QD nucleation. (Had the In shutter been kept open for 10 s longer—an additional time to reach θ_c ~1.7 ML for an InAs growth rate of 0.01 ML s^{-1}—QDs would fully develop.) At the onset, energetic adatoms, particularly those along the edges/kinks, coalesce to form small islands, eroding boundaries and shrinking platelets. As adatoms redistribute, small quasi-3D islands ~1 nm high (see, for example, *iv* in Fig. 1f) begin to flourish across the surface while ~5 nm high QDs (*v* in Fig. 1f) emerge from some cross-hatch intersections—the most preferred QD nucleation sites on CHPs.[18]

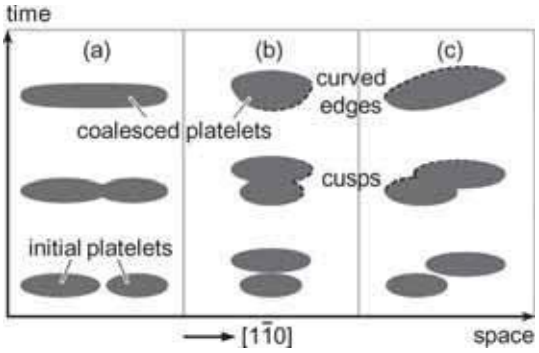

Fig. 2 Space–time map describing morphological evolution as platelets coalesce (a) lengthwise, (b) widthwise and (c) obliquely. The bottom (top) row shows the initial (final) morphology.

Platelets on the cross hatches, unlike those between the hatches, are not randomly distributed, but are guided in the orthogonal [1$\bar{1}$0] and [110] directions by the underlying misfit dislocations. They are also affected by preferential adatom diffusions in the [1$\bar{1}$0] direction. These crystallographic effects combine to yield platelets with different characteristics along the two dislocation directions.

The [110] dislocation lines such as L1 in Fig. 1a and L2 in Fig. 1b (leftward slant) cause platelets to accumulate (labelled +) on one side and to deplete (–) on the other side of the dislocation lines. Asymmetric material deposition around a dislocation results from the fact that atoms on one side of the dislocation are under compression, and on the other side tension. The asymmetric strain originates from the dislocation network at the InGaAs/GaAs interface, ~30 nm from the surface. The dislocation network comprises misfit dislocations along the orthogonal [110] and [1$\bar{1}$0] directions, and threading dislocations which glide on the $a/2\langle 110\rangle\{111\}$ slip system.[19] Surface stress above a dislocation in III–V heteroepitaxy is well understood,[18,19] and a typical stress profile in the [110] and [1$\bar{1}$0] directions is schematically shown in the inset in Fig. 1a. The sign of the stress profile reverses at the dislocation–surface intersection; it is this stress reversal that results in adatoms being drawn to one side but rejected from the opposite side of dislocations—the physical origins of platelet accumulation and depletion, respectively.

The [1$\bar{1}$0] dislocation lines such as M1 in Fig. 1a and M2 in Fig. 1b (rightward slant) cause platelet accumulation/

depletion similar to the [110] dislocation lines as explained above. But platelets on the [1$\bar{1}$0] dislocation lines have a greater tendency to merge as the sharp ends of their boundaries touch, resulting in the formation of wire-like platelets. With greater deposition thickness, the wire-like structures such as those pointed out in Fig. 1c emerge. Such surface structure can perhaps be described as planar quantum wires, a kind of nanowire whose height is only a few atomic steps. This is possibly the precursor to the nanowire on dislocation which was predicted[20] but never observed in the InAs/GaAs system.

The influence of buried dislocations over the relaxation of the ultrathin InAs layers above is not unique. Dislocations have been known to affect surface mass transport in various ways and at various scales: from guiding the running direction of μm-scale, self-propelled liquid droplets[21] to serving as preferential nucleation sites of nanoscale QDs.[22] The results above further demonstrate that the effects of dislocations are felt right down to atomically thin layers. Next, the effects will be shown to be persistent. Unless frozen in time, the morphologies above would further evolve.

B. Morphologies of annealed, ultrathin InAs layers

Set B samples are annealed for 4 min 30 s at T_{sub} of 470 °C, a condition which provides sufficient energy and time for the ultrathin platelets described above to further relax prior to quenching. During postgrowth annealing, the surface is under an As-rich condition as the In shutter is closed while the As shutter remains open. Despite continuous bombardment of As_4, surface adatoms are mobile under several driving forces. The resulting morphologies of the post-annealed 1.4-, 1.5- and 1.6-ML InAs are shown in the 5 × 5 μm^2 AFM images in Fig. 3a–c, respectively, and the 2 × 2 μm^2 images in Fig. 3d–f, respectively. The morphologies of all samples are similar. There are almost no distinct platelets as they have mostly coalesced with their neighbours to form wavy wires in the 1.4- and 1.5-ML samples, or near-straight wires in the 1.6-ML sample. As θ increases, the wires are increasingly parallel and periodic. Three key changes thus occur as a result of annealing.

Firstly, the platelets transform into wires in the [1$\bar{1}$0] direction and are spaced quite regularly in the [110] direction. Fig. 4a compares the line profiles 1–1′, 2–2′ and 3–3′ of the three samples around the areas not directly on the cross hatches as correspondingly labelled in Fig. 3a–c, respectively. The profiles in Fig. 4a show that the wires have triangular cross sections and the mean spacing between adjacent wires (x) decreases from 180 to 150 and 120 nm as θ increases from 1.4 to 1.5 and 1.6 ML, respectively. The mechanisms responsible for the transformation are the coalescence in Fig. 2 as explained earlier. The 4 min 30 s annealing merely allows the platelets to further elongate in the [1$\bar{1}$0] direction, and thus to merge and interconnect. Once merged, the cusps and curved edges just formed would be, following the terrace-ledge-kink model's minimum energy consideration,[23] smoothened and ultimately straightened. The wires only slowly merge in the [110] direction as a result of repulsive step–step interaction.[24] This keeps the wires on the flat areas well separated (at least for 4 min 30 s), with spacing inversely proportional to the availability of surface adatoms, in good agreement with the observed trend.

Secondly, the small and large dots present in the quenched 1.6-ML sample (Fig. 1c and f) disappear upon

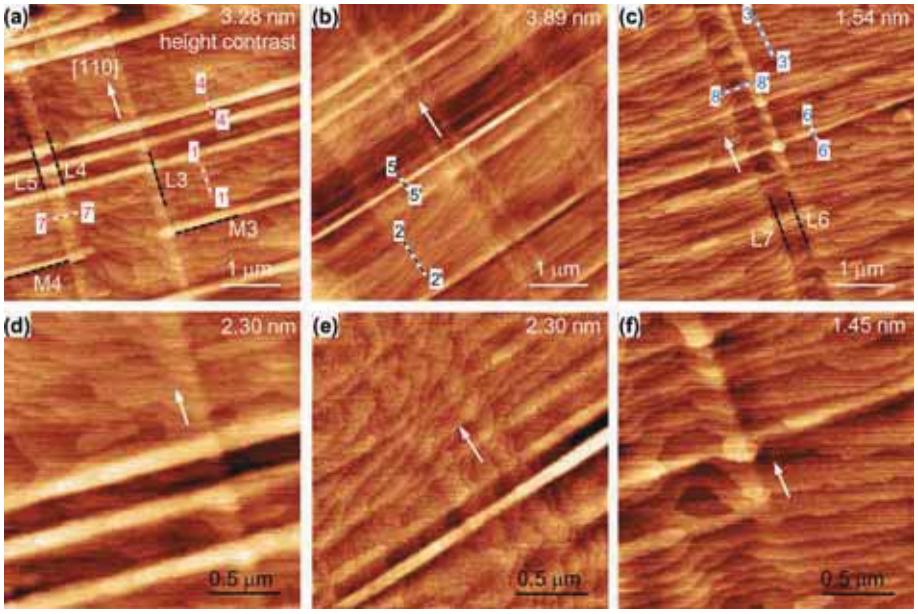

Fig. 3 AFM images of annealed, ultrathin InAs layers on cross-hatch pattern templates as InAs thickness increases from (a, d) 1.4 ML to (b, e) 1.5 ML and (c, f) 1.6 ML. Height profiles along the lines 1–1′ to 8–8′ are shown in Fig. 4 and discussed in the main text. The white arrows point in the [110] direction.

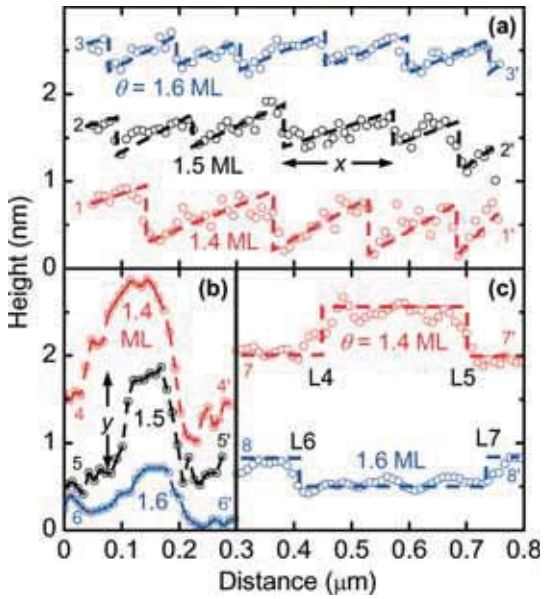

Fig. 4 Height profiles along the lines 1–1′ to 8–8′ in Fig. 3 corresponding to regions (a) between cross hatches, (b) on cross hatches and (c) between adjacent dislocation lines. (a) Shows average wire spacing (x) decreases as θ increases. (b) Shows step height (y) across dislocation lines decreases as θ increases. (c) Shows raised (lowered) steps between dislocations L4 and L5 (L6 and L7). Profiles are offset for clarity.

annealing (Fig. 3c and f). There are two possible explanations. The In adatoms could desorb from the surface during annealing. Heyn *et al.* showed that QDs can be dissolved if the temperature rises above 460 °C when the As beam is interrupted.[25] But we found that under an As_4 BEP of 8×10^{-6} torr and a typical growth temperature of 470 °C In desorption can be significantly reduced. It is highly probable that In desorption is negligible; otherwise, the overall thickness of the epilayer would decrease with a concomitant increase in the spacing—contrary to our observation. A more possible explanation is morphological instability which manifests itself in the form of In agglomeration and redistribution, giving rise to a metastable surface that exhibits a re-entrant behaviour where small quasi-QDs appear and disappear as θ approaches θ_c.[26]

Thirdly, the platelets spill over and thus planarize the cross hatches. The platelets may be bounded by the dislocations in the early stages of formation but during annealing can diffuse and coalesce with those on the opposite side of the dislocation line, flattening and obscuring the cross hatches. The greater the deposited material, the more flattened the CHPs. This is illustrated by the line profiles 4–4′, 5–5′ and 6–6′ in Fig. 4b taken across representative [1$\bar{1}$0] dislocation lines of the three annealed samples shown in Fig. 3a–c, respectively. As θ increases, the platelet height (y) decreases—challenging conventional expectation (thicker materials yield taller structures). This somewhat peculiar trend is a result of competition between the misfit strain in the epilayer and the stress fields originating from underneath. At the low end of θ (1.4 ML), the misfit energy is small. The adatoms are thus bounded by the stress fields, resulting in tall platelets. At the high end of θ (1.6 ML), the misfit energy is high. The adatoms are more energetic and can cross the stress fields, spilling over the compression–tension reversal line, joining up nearby platelets. Material spilling has an averaging effect, enabling the formation of longer and more uniform wires—albeit with a reduced average height.

While the main morphologies of the samples are satisfactorily explained by the three key changes described above, there are several areas that deserve greater scrutiny as they further illustrate the nature of the underlying CHP and provide additional insights into the combined effects of dislocation interaction and strain relaxation.

First, the areas between the [110] dislocations L4 and L5 in Fig. 3a are taller, or have more materials, than the vicinity as seen in the upper line profile (7–7′) in Fig. 4c. Material accumulation between two parallel dislocations indicate that the stress fields of the dislocations L4 and L5 interfere constructively (material accumulation sides overlap). Second, the areas between the [110] dislocations L6 and L7 in Fig. 3c are shallower, or have less materials, than the vicinity as seen in the lower line profile (8–8′) in Fig. 4c. Material depletion between two parallel dislocations indicate that the stress fields of the dislocations L6 and L7 interfere destructively (material depletion sides overlap). Third, the [1$\bar{1}$0] dislocations M3 and M4 in Fig. 3a are separated by ~2 μm. They may thus be interpreted as two unrelated dislocations. But M3 and M4 look suspiciously collinear; for two unrelated dislocation lines to exist on the same atomic plane is statistically improbable. They are more likely two halves of the same half-loop dislocation which, judging from the ~2 μm gap, most likely originated from the substrate. Fourth, the dislocation L4 in Fig. 3a can no longer accumulate material towards the bottom end of the figure. This and the fact that L4 intersects the orthogonal dislocation M4 strongly indicate dislocation blocking.

These observations attempt to explain the nature and behaviour of buried dislocations from the surface morphology of ultrathin epilayers. But without same-area corroboration with other techniques such as transmission electron microscopy (TEM), the explanations remain speculative. Obtaining correlation with TEM would however be impractical as TEM has limited fields of view and its destructive nature means that same-area plan-view and cross-sectional micrographs are not possible. Despite the speculative nature, the potential applications of such simple means to studying dislocation dynamics non-destructively must not be overlooked as such fundamental information is key to many facets of crystal engineering.

The stark differences between the morphologies of sets A and B samples clearly indicate that annealing affects the final morphology by providing more time for adatoms to move. However, it is not clear whether the parallel steps observed as a result of 4 min 30 s annealing are the final, stable shape, or whether the steps are metastable and will evolve into yet another shape given even longer annealing time.

C. Extended annealing of ultrathin InAs layers

Additional 1.6-ML InAs samples are grown identically to those in sets A and B and annealed at the same T_{sub} of 470 °C but with much longer annealing times of 1 or 2 hours. It was found that the surfaces of all samples subjected to the prolonged annealing are almost completely planarized: no wires and almost no steps are observed in the areas between the cross hatches while the cross hatches appear as ~1 nm steps. This level of flatness is the same as that of as-grown InGaAs CHP on GaAs before the growth of InAs layer.[27] This means that at T_{sub} of 470 °C the platelets/wires continue to coalesce lengthwise and widthwise, resulting in a planarized surface within the first hour.

Unexpectedly, towards the end of a 2 hour annealing of one of the 1.6-ML samples, the As_4 partial pressure fluctuates a short while before stabilising. Such a fluctuation in our system is at times caused by temporary disruption in the liquid nitrogen supplies cooling the cryoshroud and at other times by As ingot displacement in the crucible which for solid-source MBE rarely but does occur. The accidental pressure disruption results in a drastic change in morphology. Repeated experiments were carried out to confirm that the following morphology is caused by the reduction of As_4 BEP. Platelets now return, but not as the familiar hemi ellipsoids in Fig. 1 nor triangular wires in Fig. 3. Instead, the platelets are stacked in the growth direction which make them look like a pyramid having a rhombus base with micron-scale sides and nanoscale heights. Fig. 5a shows the AFM image of a typical area, depicting stacked platelets not directly on (lower half of the figure) and directly on (upper half) a dislocation (white dashed line). The stacked platelets on the dislocation have crisp, straight edges. Geometry indicates that the platelets are bounded by planes in the {611} family which when projected onto the (001) surface make an angle of $\alpha \approx 35°$ with the $[1\bar{1}0]$ direction as shown in Fig. 5b. The angles at the base of the rhombus are thus 2α and $180° - 2\alpha$ as shown in the schematic drawing in Fig. 5a. When viewed using white-light interferometry, the platelets are seen to concentrate along the $[1\bar{1}0]$ dislocation lines. Fig. 5c shows the AFM image of one of the tallest structures on a dislocation line. Line profiles across the stacked platelets p–p′ in Fig. 5a and q–q′ in Fig. 5b are shown in Fig. 5d. The discontinuities in the line profiles indicate that the rhombus platelets are mono-atomic (step height a) or bi-atomic ($2a$) steps. This morphology is unexpected and the ~6 nm height is surprising.

The expected morphology when group V partial pressure drops during III–V epitaxy is the formation of group III liquid droplets. During annealing, a drop in V partial pressure at a high T_{sub} usually causes the surface to lose group V atoms significantly if T_{sub} exceeds the congruent temperature T_c, resulting in the formation of III droplets.[28] For bulk InAs (001), the literature value of T_c is 440 °C.[29] Thus, it is expected that at T_{sub} of 470 °C, the surface should be populated by In droplets or—if the In droplets are re-crystallized when the As_4 BEP recovers—by InAs QDs. The AFM images in Fig. 5 show that neither of these scenarios occurred. This is most likely because the background As_4 pressure prevents the InAs surface from sublimation. Zhou *et al.* reported a systematic study of GaAs sublimation as a function of As flux F and concluded that T_c increases linearly with F.[30] Though no equivalent information for InAs exists in the literature, the relationship should be applicable to other III–V arsenides.

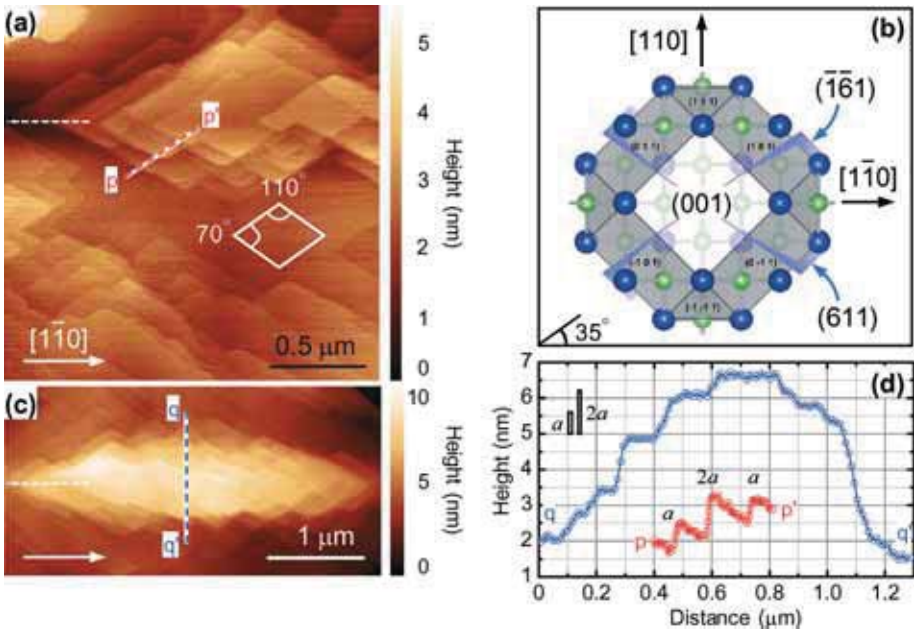

Fig. 5 (a, c) AFM images of stacked platelets on dislocation lines (white dashed lines). (b) A crystal model showing that the lines created by the intersections of the ($\bar{1}\bar{6}$1) and (611) planes with the (001) surface make ±35° angles with the $[1\bar{1}0]$ direction. (d) Height profiles along the lines p–p′ and q–q′ in (a) and (c), respectively.

Removal of the InAs layer under As_4 partial pressure should thus occur well above the literature value of T_c (440 °C) obtained under ultra-high vacuum (UHV) evaporation. In fact, a standard practice for growth rate calibrations of InAs on GaAs substrates is to form sacrificial InAs QDs which are later re-evaporated at 520 °C or higher. The absence of In droplets and InAs QDs is thus due to the background As_4 pressure (F) being so high that $T_{sub} < T_c(F)$.

The observed pyramidal morphology is surprisingly tall. The line profiles in Fig. 5d show that the apex of a pyramid can reach up to 6 nm above the base—far thicker than the deposited thickness of 0.48 nm (2D equivalent thickness of 1.6-ML InAs), raising questions regarding the source of materials and the responsible mechanisms.

The materials arise (literally) from the epilayer immediately below InAs: the 6 nm GaAs spacer. Despite the low probability of InAs re-evaporation at the conditions used, the temporary dip in As_4 pressure does give surface III atoms added mobility —both in the growth plane and normal to it. The As-deficit surface allows In atoms to move further or to be dislodged more often before being re-incorporated into the lattice, resulting in increased in-plane diffusion. The out-of-plane motion of atoms results from Ga trying to climb the steps as shown in the schematic drawing in Fig. 6. Ga climbing results in removal of Ga atoms from the base and removal of In atoms from the top of the pyramid. The latter is equivalent to etching. It is widely reported that under III-rich surface conditions, III droplets form and etch the underlying surface[31] and under UHV conditions the droplets are so free that they etch and run.[21,32] The preference of Ga atoms to reach the apex and for In atoms to move in the opposite direction has been explained in the case of GaAs-capped InAs QDs due to chemical potential.[33] As the 6 nm GaAs spacer is depleted and the InGaAs pyramid is formed, the chemical potential between the pyramid and the layer beneath (InGaAs CHP) decreases and no further In–Ga exchange takes place. The height of the pyramid is thus limited to the spacer thickness.

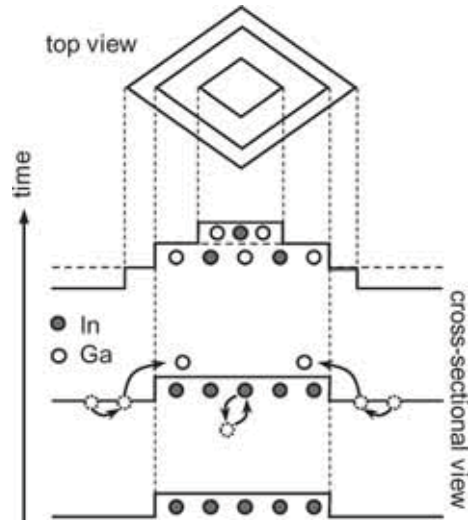

Fig. 6 Schematic diagram describing how stacked platelets (top view and top panel of the cross-sectional view) are formed as a result of out-of-plane In and Ga atoms motion around the initial InAs monoatomic step (bottom panel). Arsenic atoms are not shown for clarity.

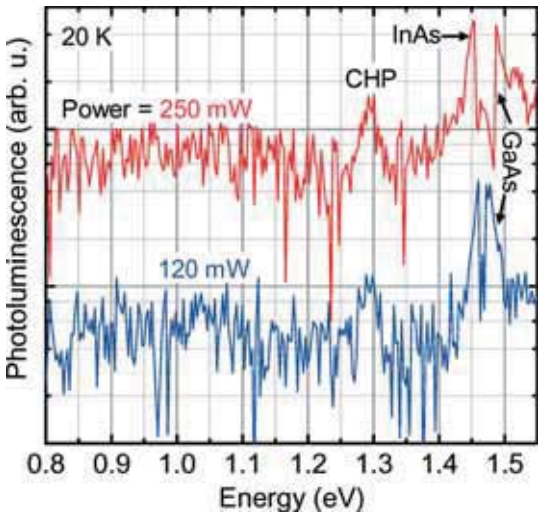

Fig. 7 Photoluminescence spectra of the annealed, 1.5-ML InAs sample whose morphology appeared earlier in Fig. 3b and e.

These ultrathin InAs structures are optically active even though they are uncapped. As an example, PL spectra of the annealed 1.5-ML sample whose morphologies appeared earlier in Fig. 3b and e are shown in Fig. 7. The PL signals shown are measured at 20 K with 120 and 250 mW laser power. Both signals are noisy and weak—up to two orders of magnitude weaker than those obtained from capped InAs QDs using the same setup.[34] The signals contain three distinct peaks: 1, the 1.49 eV peak due to the GaAs substrate; 2, the 1.30 eV peak due to the underlying CHP (InGaAs) layer[34] and 3, the 1.45 eV peak due to the ultrathin InAs layer. The ultrathin layer is nominally InAs. Its actual chemical makeup may be more accurately described as InGaAs since In atoms in the ultrathin layer can exchange positions with Ga atoms in the substrate. The CHP peak indicates that the presence of the underlying dislocations does not severely impact the optical quality of the overlying layers, in good agreement with previous studies.[35,36] In addition, though the surface layer is not optimized in terms of luminescence efficiency, it is evident from the spectra that the ultrathin InAs layer is the most optically efficient. Its peak position at 1.45 eV agrees well with that of a previous report.[26] PL measurements are taken down to 0.8 eV in order to show the absence of emission between 0.8 and 1.2 eV, a typical emission range of buried and surface QDs.[4] The strong and single emission band is useful as optical feedback in sensor applications.

Conclusions

The relaxation of ultrathin InAs layers on InGaAs cross-hatch patterns results in many morphologies that depend principally on misfit (InAs thickness) and annealing conditions (temperature, time, As_4 pressure). Understanding the

pathways of these strain-modulated, ultrathin layers is of fundamental and technological importance as the layers can serve as a material platform for quantum interaction studies and for applications that take advantage of their surface sensitivity and shape asymmetry. In electronics, the critical dimension of transistors shrink from the μm scale in the 1950s to nanoscale starting in 1999, driving current research on low-dimensional materials such as QDs, nanowires and graphenes.[37] It is thus not unreasonable to project that platelets and wires with heights measured in atomic steps described here would be of interest, or even inevitable, in future generations of electronic devices. In the near term, the approaches taken to interpret the morphology of ultrathin layers around dislocations may aid studies in heterogeneous deposition on chemically stripe-patterned substrates[38] and may have a wide applicability in heteroepitaxy. Dislocation decoration, for example, by nanoparticles generally yields just the location information.[39] Decoration by ultrathin layers, in contrast, results in platelet morphology that not only points to where the dislocations are but also hints at their nature and dynamics.

Acknowledgements

This work was carried out under financial support from Thailand Research Fund (RSA5880049), Chulalongkorn University, AOARD and NSTDA Research Chair Grant (FDA-CO-2558-1407-TH).

References

1 D. Bimberg, M. Grundmann and N. N. Ledentsov, *Quantum Dot Heterostructures*, Wiley, Chichester, 1999.
2 R. Samti, F. Raouafi, M. Chaouach, M. Maaref, A. Sakri, J. Even, J.-M. Gerard and J.-M. Jancu, *Appl. Phys. Lett.*, 2012, **101**, 012105.
3 Z. L. Miao, Y. W. Zhang, S. J. Chua, Y. H. Chye, P. Chen and S. Tripathy, *Appl. Phys. Lett.*, 2005, **86**, 031914.
4 B. L. Liang, Z. M. Wang, Y. I. Mazur and G. J. Salamo, *Appl. Phys. Lett.*, 2006, **89**, 243124.
5 H. Ajlani, R. Othmen, M. Oueslati, A. Cavanna and A. Madouri, *J. Vac. Sci. Technol., B*, 2013, **31**, 020602.
6 M. J. Milla, J. M. Ulloa and A. Guzman, *ACS Appl. Mater. Interfaces*, 2014, **6**, 6191.
7 A. Madhukar, S. Lu, A. Konkar, Y. Zhang, M. Ho, S. M. Hughes and A. P. Alivisatos, *Nano Lett.*, 2005, **5**, 479.
8 C.-Y. Zhang, H.-C. Yeh, M. T. Kuroki and T.-H. Wang, *Nat. Mater.*, 2005, **4**, 826.
9 P. Bergveld, *Sens. Actuators*, 1981, **1**, 17.
10 J. Wu and P. Jin, *Front. Phys.*, 2015, **10**, 108101.
11 I. Daruka and A. L. Barabási, *Phys. Rev. Lett.*, 1997, **79**, 3708.
12 C. Priester and M. Lannoo, *Phys. Rev. Lett.*, 1995, **75**, 93.
13 G. M. Guryanov, G. E. Cirlin, A. O. Golubok, S. Y. Tipissev, N. N. Ledentsov, V. A. Shchukin, M. Grundmann, D. Bimberg and Z. I. Alferov, *Surf. Sci.*, 1996, **352–354**, 646.
14 A. Polimeni, A. Patanè, M. Capizzi, F. Martelli, L. Nasi and G. Salviati, *Phys. Rev. B: Condens. Matter Mater. Phys.*, 1996, **53**, R4213.
15 T. Alexander, V. Dubrovskii, Y. Musikhin, V. Ustinov, G. Cirlin, N. Polyakov, Y. Samsonenko and P. Werner, *Int. J. Nanosci.*, 2007, **6**, 339.
16 L. Seravalli, G. Trevisi and P. Frigeri, *CrystEngComm*, 2012, **14**, 1155.
17 G. E. Cirlin, G. M. Guryanov, A. O. Golubok, S. Y. Tipissev, N. N. Ledentsov, P. S. Kop'ev, M. Grundmann and D. Bimberg, *Appl. Phys. Lett.*, 1995, **67**, 97.
18 S. Kanjanachuchai and T. Limwongse, *J. Nanosci. Nanotechnol.*, 2011, **11**, 10787.
19 A. M. Andrews, J. S. Speck, A. E. Romanov, M. Bobeth and W. Pompe, *J. Appl. Phys.*, 2002, **91**, 1933.
20 I. A. Ovid'ko and A. G. Sheinerman, *J. Phys.: Condens. Matter*, 2004, **16**, 2161.
21 S. Kanjanachuchai and P. Photongkam, *Cryst. Growth Des.*, 2015, **15**, 14.
22 S. Y. Shiryaev, F. Jensen, J. L. Hansen, J. W. Petersen and A. N. Larsen, *Phys. Rev. Lett.*, 1997, **78**, 503.
23 J. Venables, *Introduction to Surface and Thin Film Processes*, Cambridge University Press, 2000, pp. 5–7.
24 H. Ibach, *Surf. Sci. Rep.*, 1997, **29**, 195.
25 C. Heyn, D. Endler, K. Zhang and W. Hansen, *J. Cryst. Growth*, 2000, **210**, 421.
26 R. Heitz, T. R. Ramachandran, A. Kalburge, Q. Xie, I. Mukhametzhanov, P. Chen and A. Madhukar, *Phys. Rev. Lett.*, 1997, **78**, 4071.
27 T. Limwongse, S. Panyakeow and S. Kanjanachuchai, *Phys. Status Solidi C*, 2009, **6**, 806.
28 B. A. Trisna, N. Nakareseisoon, W. Eiwwongcharoen, S. Panyakeow and S. Kanjanachuchai, *Nanoscale Res. Lett.*, 2015, **10**, 184.
29 M. Yano, H. Yokose, Y. Iwai and M. Inoue, *J. Cryst. Growth*, 1991, **111**, 609.
30 Z. Y. Zhou, C. X. Zheng, W. X. Tang, D. E. Jesson and J. Tersoff, *Appl. Phys. Lett.*, 2010, **97**, 121912.
31 C. Heyn, S. Schnull, D. Jesson and W. Hansen, *Nanoscale Res. Lett.*, 2014, **9**, 285.
32 S. Kanjanachuchai and C. Euaruksakul, *Cryst. Growth Des.*, 2014, **14**, 830.
33 R. Songmuang, S. Kiravittaya and O. G. Schmidt, *J. Cryst. Growth*, 2003, **249**, 416.
34 T. Chokamnuai, P. Rattanadon, S. Thainoi, S. Panyakeow and S. Kanjanachuchai, *J. Cryst. Growth*, 2013, **378**, 524.
35 S. L. Golovynskyi, L. Seravalli, G. Trevisi, P. Frigeri, E. Gombia, O. I. Dacenko and S. V. Kondratenko, *J. Appl. Phys.*, 2015, **117**, 214312.
36 S. Kanjanachuchai, M. Xu, A. Jaffré, A. Jittrong, T. Chokamnuai, S. Panyakeow and M. Boutchich, *Semicond. Sci. Technol.*, 2015, **30**, 055005.
37 *The International Technology Roadmap for Semiconductors (ITRS)*, http://www.itrs.net/.
38 C. Honisch, T.-S. Lin, A. Heuer, U. Thiele and S. V. Gurevich, *Langmuir*, 2015, **31**, 10618.
39 B. Yang, F. Yuan, Q. Liu, N. Huang, J. Qiu, T. Staedler, B. Liu and X. Jiang, *ACS Appl. Mater. Interfaces*, 2015, **7**, 2790.

ภาคผนวก 2

CRYSTAL GROWTH & DESIGN

August 2017
Volume 17
Number 8
pubs.acs.org/crystal

INTEGRATING THE FIELDS OF CRYSTAL ENGINEERING AND CRYSTAL GROWTH FOR THE SYNTHESIS AND APPLICATIONS OF NEW MATERIALS

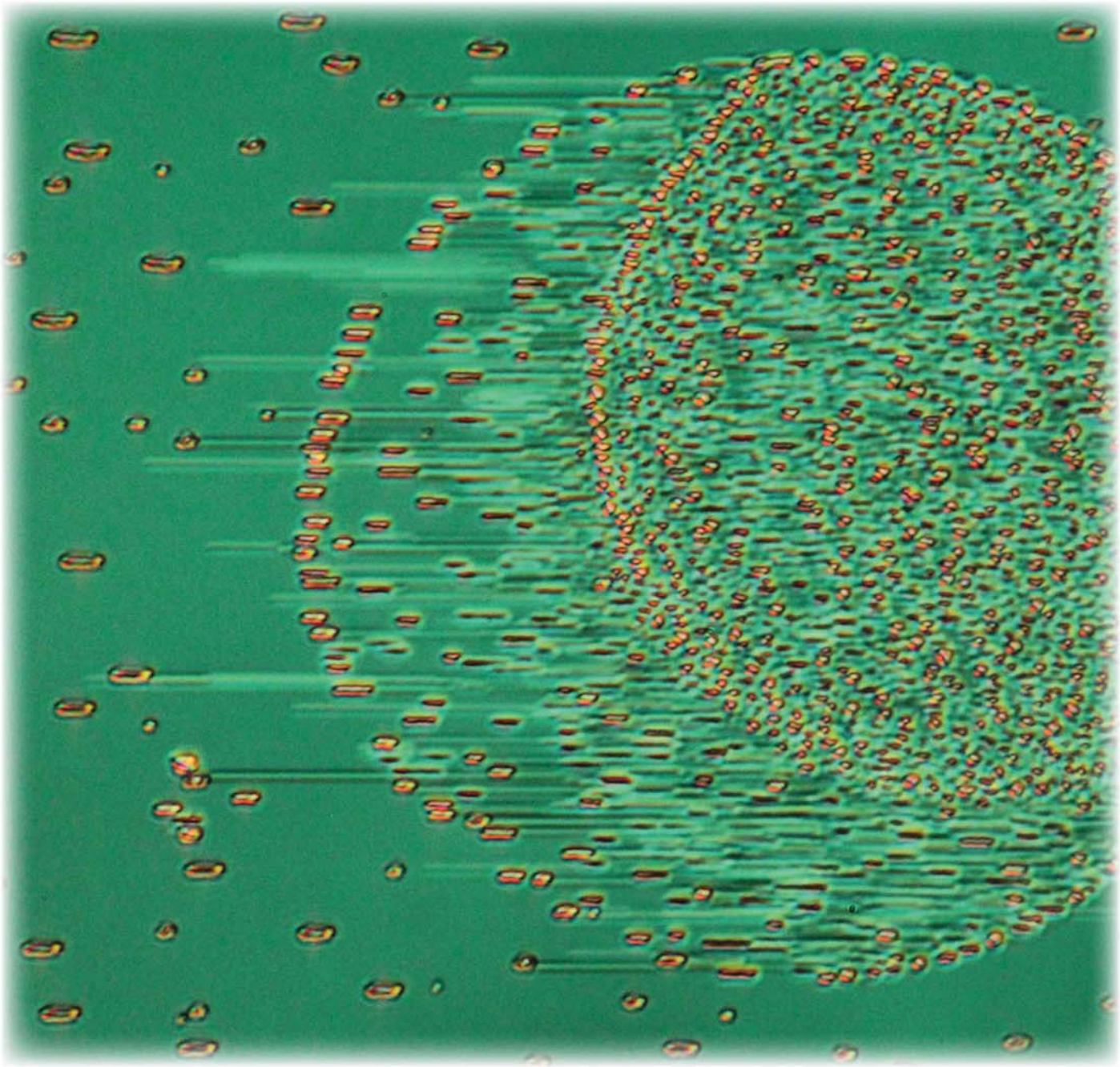

ACS Publications
Most Trusted. Most Cited. Most Read.

www.acs.org

CRYSTAL GROWTH & DESIGN

Article

pubs.acs.org/crystal

Planar Self-Assembly of Submicron and Nanoscale Wires and Grooves on III–V(110) Surfaces

Songphol Kanjanachuchai*,† and Pat Photongkam‡

†Semiconductor Device Research Laboratory, Department of Electrical Engineering, Faculty of Engineering, Chulalongkorn University, 254 Phayathai Road, Bangkok 10330, Thailand

‡Synchrotron Light Research Institute (Public Organization), Ministry of Science and Technology, Nakhon Ratchasima 30000, Thailand

Supporting Information

ABSTRACT: Metallic Ga and In submicron and nanowires (NWs) tens of microns long naturally form via a self-propelled mechanism on the (110) surfaces of GaAs and InAs, respectively, during noncongruent sublimation in ultrahigh vacuum. Under stringent conditions, low-energy electron microscopy uncovers GaAs and InAs(110) surfaces on the brink of decomposition rapidly assemble planar wires of their cations in the ⟨$\bar{1}$10⟩ direction. For InP(110), wire formation is unfavorable due to a smooth decomposing front but can be assisted by Au nanoparticles (NPs), which sacrifice themselves to form rough pits via solid–liquid–vapor etching. The resulting self-assembled and AuNP-assisted NWs grow crystallographically in a self-sustainable manner, unless they are obstructed and consumed by stationary microdroplets, leaving emptied grooves. The findings reveal a hitherto hidden natural process on the surfaces of binary crystals capable of producing elementary submicron and nanoscale wires without extrinsic materials, paving the way for the controlled fabrication of planar NWs, grooves, and NW/groove arrays with lengths approaching circuits or even chips scale and with potential applications in self-integrated circuits, plasmonics, and fluidics.

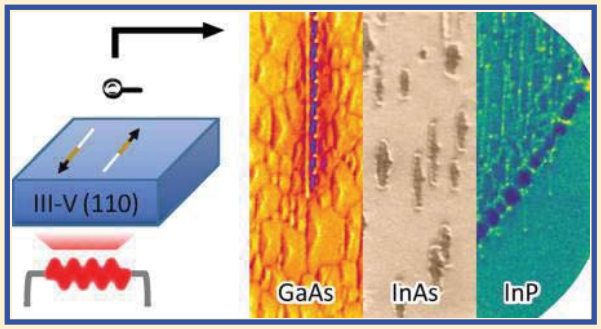

INTRODUCTION

When single crystals of III–V semiconductors such as GaAs and InP are sublimated in vacuum the greater loss of group-V atoms often results in the agglomeration of the low melting point group-III atoms on the surface in the form of droplets,[1] which recently gained considerable attention as metallic droplets on their own serve useful optical functions in plasmonics and photovoltaics[2,3] and, when used as templates for growth, serve to nucleate many important optoelectronic devices, particularly quantum dots (QDs) and nanoholes through droplet epitaxy (DE)[4−7] and nanowires (NWs) through vapor–liquid–solid (VLS)-based growth.[8−10] When a droplet serves to catalyze crystal growth, changes of process parameters that affect the droplet will directly impact the final morphologies and hence the properties of the ensuing devices. In the case of VLS-based growth of vertical NWs, for example, changes in droplet statics during growth affect the wall profile or the tapering characteristics, while kinetics and thermodynamic changes affect crystallization process, which may alter droplet direction and thus the branching and kinking geometries.[11−13] In the case of VLS-based growth of planar NWs, it is implicit that droplets change their positions by crawling on,[12,14−17] or even reacting with,[18,19] the surface to enable growth. Understanding the varieties of shapes and movements of catalytic liquids on semiconductor surfaces is thus a matter of great technological importance. Low melting point group-III liquids, in particular, play a central role in the DE-based growth of QDs and molecules[4,5] and in the VLS-based growth of self-assisted or self-catalyzed III–V NWs.[20] The formation of group-III liquids on III–V surfaces can be accomplished using an external (for example, by dissociating metal organic precursors) or an internal source (by noncongruent sublimation). Regardless of the sources, the resulting group-III liquids are essentially hemispherical and dispersed randomly, limiting the templated self-assembled structures to mostly isolated QDs and NWs, placing practical limits to functioning circuits.

In this work, several unprecedented group-III liquid and void morphologies in the submicron and nanoscale are reported. Using *in situ* microscopy, we reveal a planar self-assembly mechanism capable of producing droplet chains and extremely long metallic wires and grooves on III–V(110) surfaces without external material source or lithography. The mechanism manifests itself in a narrow temperature window during sublimation, is spontaneous, and results from competition among the various interfacial energies, the liquid surface energy, and crystallographic etching. When Au nanoparticles (NPs) are employed, accelerated decomposition at the NP sites results in

Received: May 18, 2017
Revised: June 17, 2017
Published: June 19, 2017

DOI: 10.1021/acs.cgd.7b00707
Cryst. Growth Des. 2017, 17, 4413−4421

planar nanowires and grooves with widths dictated by the NP diameter. The resulting micro- and nanostructures provide a useful morphology that could be adopted or optimized for various functions such as transport channels in micro/nanofluidics,[21] high-density interconnection in microelectronics,[22] semiconducting NW arrays in optoelectronics,[23] and metallic/hole arrays in plasmonics.[2]

EXPERIMENTAL SECTION

The experiments involve heating GaAs, InAs, and InP(110) epi-ready substrates above their congruent temperatures (T_C) under ultrahigh vacuum (UHV) in Elmitec's spectroscopic photoemission and low-energy electron microscope (SPELEEM) following our previous procedure.[24] Each as-received substrate is scribed to shape, mounted on a Mo holder, loaded into the system, outgassed overnight, and annealed at increasing temperatures until the surface undergoes significant morphological transformation as a result of noncongruent sublimation. The Mo holder has at its backside a W filament for radiative heating, and at its front side a thermocouple welded to the sample base plate, which measures the sample temperature with ±20 °C uncertainty after calibration. The sample is outgassed and sublimated under UHV by controlling the W filament current I_F. During sublimation, the pressure is maintained in the $1-5 \times 10^{-9}$ Torr range and never exceeds 10^{-8} Torr. After oxide desorption, I_F is stepped such that the temperature increases by ∼2−5 °C every ∼5−10 min. While ramping up the temperature, the surface is imaged in real time via LEEM using low electron energy E typically lower than 5 eV. The presence of surface metals can be confirmed *in situ* using photoemission electron microscopy (PEEM) by shining 4.88 eV ultraviolet (UV) photons from a Hg arc lamp and forming the image using photoelectrons.

Ex situ morphology is studied using field-emission scanning electron microscopy (SEM, JEOL 7610F), differential interference contrast (DIC) optical microscopy (Nikon ME600P), and white-light interferometry (WLI, Polytec's MSA-400).

To study the catalytic effects of NPs on sublimation, solution containing AuNPs (mean diameter 20 nm, Prime Nanotechnology Co.) is sprayed onto the surface of interest at room temperature. The sample is then oven-dried at a maximum temperature of 150 °C for 2 h to remove the solvent. The diameter of the spray nozzle is 3 mm. Dried atomized droplets vary in diameter from a few 10s to a few 100s of micrometers. The spraying action is manual; no attempts are made to control the droplet size.

RESULTS AND DISCUSSION

The (110) surfaces of GaAs, InAs, and InP subject to Langmuir evaporation undergo complex morphological evolution. Between the early stages of noncongruent sublimation where small group-III droplets nucleate and the late stages where large droplets form by coalescence, there exists an intermediate stage where planar, submicron and nanoscale wires and grooves form by self-assembly, and reported here for the first time. The difficulties in observing these transitional structures lie in the stringent temperature, imaging, and timing conditions required, which explain why they have evaded detection despite decades of sublimation experiments involving III−V compounds.[1,25−27] Using LEEM, a highly surface sensitive *in situ* electron microscopy, we reveal the existence of these technologically important structures, explain how they evolve, and demonstrate how their sizes can be partly controlled using NPs. The results are divided into three parts. First, the evolution of sublimating GaAs(110) surface and the rich morphologies will be independently described. These will then be compared with other III−V(110) surfaces in the second part. One of the key findings is the presence of nanowires and grooves with densities proportional to the roughness of the decomposing front. With this insight, the third part proceeds to demonstrate how NPs can be used to locally increase the surface roughness, thus enticing nanowires and grooves to form at or close to the intended positions.

1. GaAs(110). The morphological evolution of sublimating GaAs(110) surface to be described in this section occurs at a substrate temperature T_S around 680 °C, higher than the congruent temperature T_C of ∼625 °C for GaAs(001)[27] and ∼655 °C for GaAs(111)A.[28] As the temperature approaches 680 °C, the *in situ* mass spectrometer registers an appreciable signal for As (75 amu), and the GaAs(110) surface starts to roughen. Before describing the results for GaAs(110), it is best to summarize how other orientations of GaAs roughen as they are sublimated.

Thermal roughening of GaAs surfaces is generally crystallographic, with etch pits bounded by the slow-etching {111} planes. The etch pits on GaAs(001) and (111)A thus take the square and triangular shapes, respectively.[27,28] The pits are continually filled with Ga as they act as sinks for surface Ga atoms, forming liquid Ga droplets. As sublimation continues, the Ga droplets etch deeper into the substrate, grow, and propel themselves from the pits once they reach a critical diameter of 1.9 μm.[29] These mobile Ga droplets have been observed on sublimating GaAs(001), (111)A, and (111)B and are typically referred to as self-running or self-propelled droplets.[27−29] It is thus reasonable to expect that the sublimation of GaAs(110) results in crystallographic pits followed by self-propelled, micron scale droplets.

The sublimation of GaAs(110) indeed results in crystallographic pits. However, the etch pits are somewhat asymmetric, becoming more evident as large pits grow at the expense of small pits. This is illustrated in the *in situ* LEEM images in Figure 1a−c (see also Supporting Video V1). The contrast in the images reflects the topography of thermal etch pits. At the center of each pit lies a V-shaped dimple a few to a few tens of nanometers deep, depending on the sublimation time. The V shape indicates symmetric etching along the equivalent $[\bar{1}10]$ and $[1\bar{1}0]$ directions (hereafter referred to as the $\langle\bar{1}10\rangle$ direction[30]), and asymmetric etching in the orthogonal direction due to the different etch rates between the (111)A- and (111)B-type facets bounding the V-shaped pits in the $[001]$ and $[00\bar{1}]$ directions, respectively. This asymmetry is due to the greater chemical activity of the high valence, As face with respect to the low valence, Ga face,[31] which results in GaAs(111)B having a lower T_C and thus a greater etch rate than GaAs(111)A at the same T_S.[28] The perimeters of the pits are poorly defined as the pits randomly merge and surface Ga atoms redistribute. The pits deepen with time. Past experiments[24,28,32] on many of the (001) and (111) surfaces of GaAs, InP, InAs, and InSb indicate that, with prolonged sublimation, individual etch pits and the group-III liquid accumulated inside the pits would expand; droplets of Ga or In would then form and move away from the nucleating pits. What we observed is different, even surprising as the group-III liquid forms not only droplets but also thin filaments that run.

During the relatively slow pits expansion, a fast-running filamentary structure appears, seemingly out of nowhere. This is seen as the out-of-focus trail in Figure 1c (dashed arrow). The trail was almost unnoticed because the running front was small, emerged unexpected, zipped across the entire field of view, and appeared at a different focus from the pits in the background. Realizing an unusual dynamic unfolding, we quickly follow the trail and readjust the sample manipulator in order to image

DOI: 10.1021/acs.cgd.7b00707
Cryst. Growth Des. 2017, 17, 4413−4421

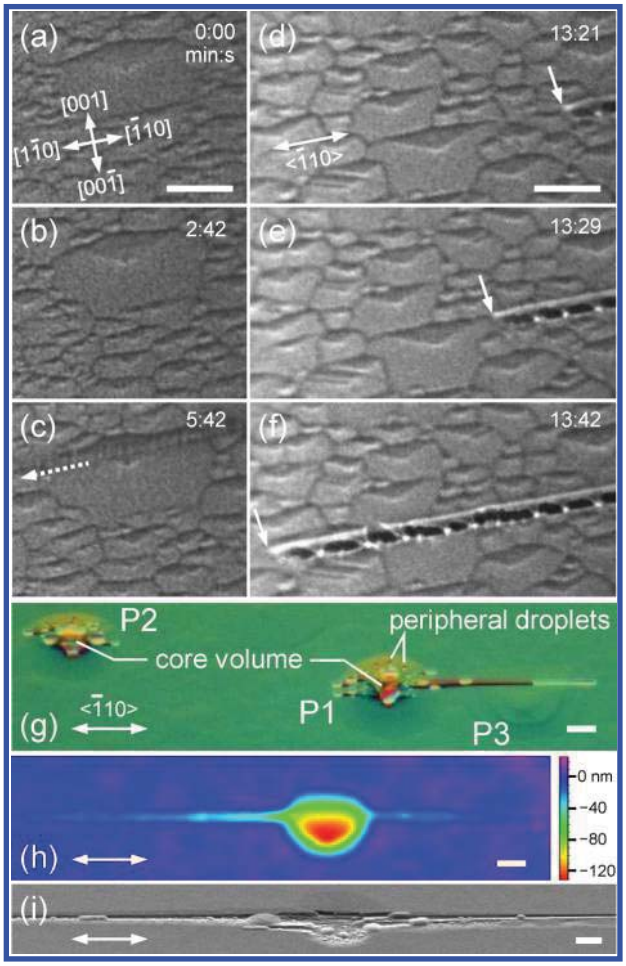

Figure 1. Thermal etch pits and self-assembled wires and grooves on GaAs(110) surface. (a–c) LEEM images (E = 0.3 eV) showing the V-shaped etch pits expanding and coalescing during the 5 min 42 s Langmuir evaporation at 680 °C. In (c), an out-of-focus feature running across the surface (dotted arrow) can barely be seen. (d–f) LEEM images (E = 0 eV) capturing the motion of a liquefying front (arrows) flowing across the surface at a speed of 1 μm/s. The times in (a–f) are relative to (a). (g) DIC image of a lightly sublimated area showing a few large pits from which narrow wires and grooves emerge. (h) WLI image (phase mode) showing the depth profile of a well isolated etch pit. (i) SEM image (tilted ~20° off normal) of an etch pit showing the almost depleted core region and the immediate vicinity. Double-headed arrows point in the ⟨$\bar{1}$10⟩ direction.[30] Scale bars: 5 μm.

other areas. A typical observable event starts off with a liquefying front coming into view, continuing on a straight path, and going out of view as shown in another image series in Figures 1d–f. The liquefying front (arrows) runs across the surface at an approximate speed of 1 μm/s (see also Supporting Video V2), much faster than the expansion rate of the background etch pits. Two questions immediately arise: How is the liquefying front formed, and what is the nature of this running structure?

The first question aims at identifying the origin of liquefying fronts. Despite many repeated experiments the nucleation of liquefying fronts could not be observed *in situ* by LEEM due to limited field of view, shallow depth of focus, and narrow time window. The latter is due to the fact that prolonged imaging while sublimating risks sample damage because As_2 and/or As_4 leave the surface in drove, pushing the system's pressure up to the practical limit of about 10^{-8} Torr where arcing due to high voltage (20 kV electron optics) could occur at any moment of slightest system's instability. Indeed, many samples were damaged by arcing. Only when a sample is minimally sublimated (I_F set to zero when the etch pits seem large, even before the appearance of any liquefying front in LEEM) and only after taking the sample out and viewing the surface *ex situ* could the nucleation sites of these running fronts be identified as the peripheries of the thermal etch pits whose diameters have expanded beyond approximately 40 μm. Figure 1g shows a DIC image of an area with two of such pits. P1, the more prominent pit, is partly filled with Ga, which converges in the center in a V shape, reflecting the LEEM morphology. P1 has straight trails jutting out on both sides in the ⟨$\bar{1}$10⟩ direction. The trails comprise dark (empty groove) and bright, shiny (Ga-filled) segments in roughly equal proportion. Pit P2 is qualitatively similar to but slightly smaller than P1, indicating that both pits evolve in the same manner, but P2 is at a less mature stage than P1. To the right of P1 is P3, which is similar in size but is devoid of Ga, possibly because it competes for Ga with P1, but lost. For a pit to be able to accumulate sufficient liquid Ga for the latter to reach a critical escape size, its depth must be at least 40–50 nm. Figure 1h shows the depth profile (taken using WLI) of a well isolated and well sublimated pit where Ga atoms have vacated the pit. The trough of the pit has a V-shaped profile, consistent with the DIC and LEEM images above. This particular pit is ~120 nm deep, and the trails that jut out horizontally emerged at a depth of ~40 nm. These *ex situ* analyses lead to the conclusion that the liquefying fronts observed *in situ* (Figures 1c–f) originated from large thermal etch pits whose troughs are located below the surface at a certain critical depth estimated at 40–50 nm.

The large V-shaped pits act as liquid Ga reservoirs, and like all reservoirs, their capacities are limited. When overfilled, the liquid inside the pits become unstable and reduce its energy and volume by forming liquefying fronts. This at first seems counterintuitive as one normally expects liquids to ball up, taking a hemispherical shape as observed on GaAs(001), (111)A, and (111)B.[28] This is not the case on GaAs(110). The main reason lies in the pit's profile. Flat-bottomed pits on GaAs(001) and (111) make it energetically favorable for the liquid inside to ball up, forming hemispherical droplets. Pointed-bottomed pits on GaAs(110) in contrast have multiple inclined facets that help stabilize the liquid because the liquid–substrate contact area is greater than the liquid–vapor area (free surface). With increased Ga incorporation from the surrounding and the slow etch rate, balling up is inevitable, but it occurs first around the outer reaches of the V-shaped centers as seen in Figure 1g. As these peripheral droplets (high surface energy γ) grow and touch the core liquid volume (low γ), the latter is momentarily destabilized, and because it is brimming, it quickly transfers some liquid to the former, initiating rapid etching in one of the ⟨$\bar{1}$10⟩ directions. The core liquid volume thus decreases, and while it is not yet empty, the same process can occur at other peripheral sites if more droplets touch the core volume. A single pit thus yields several liquefying fronts. Figure 1i shows the SEM image of a near emptied pit, with some Ga globules remaining in the center and small fractions clinging near the perimeter of the pit, just escaped or about to escape.

The mechanisms affecting the liquid dynamics are various and complex, as are all reactive wetting systems.[33] The driving force acting on the droplets has been explained in terms of

DOI: 10.1021/acs.cgd.7b00707
Cryst. Growth Des. 2017, 17, 4413–4421

chemical potential gradient,[27,34] atomic steps elimination,[35,36] and surface reconstruction.[37,38] It is likely that all these mechanisms, in combination or competition with recrystallization, crystallographic etching,[24,28,39] wetting, and dewetting dominate different stages of the liquefaction.

The second question concerns the nature of the running structures, and the answer to which is best studied from the trails. The trail in Figure 1d–f looks continuous, judging from the straight white line, but the adjacent dark blobs give the impression that the trail could also be discontinuous. Though LEEM imaging is highly surface sensitive, it cannot tell the exact location of Ga as the white/black contrast can be switched by small changes in the electron energy E around the mirroring condition, E = 0 eV. Thus, the images in Figures 1d–f are inconclusive whether the trail is one long wire (should the white line be believed), or one long chain of droplets (dark blobs), or something else.

To elucidate the nature of the trails *in situ*, we illuminate the surface with UV light and study the contrast resulting from photoelectrons. In UV PEEM, areas with low work function (metal) appear bright against dark, high work function (semiconductor) background. Figure 2a shows the LEEM image of an area containing three parallel trails of slightly differing widths but all are at least 55 μm long. When exposed to UV light, the same-area PEEM image in Figure 2b shows that the three trails have different contents: the top (middle) trail is entirely (partially) filled with Ga droplets, but the bottom trail which is the narrowest is only sparingly occupied by a few droplets. These show that some liquefying fronts repeatedly breakup, while some others do not, but instead run as a wire, dragging along liquid Ga, leaving emptied grooves in their trails and intermittently spitting out droplets. The grooves are thus formed without external materials. These self-formed grooves thus differ from and, in terms of cleanliness, are a significant improvement on existing fabrication processes that rely on simultaneous motion of deposited materials (for example, Au droplets formed by annealing thin, evaporated Au films) and substrate etching,[18] particularly by gaseous environment.[40−42]

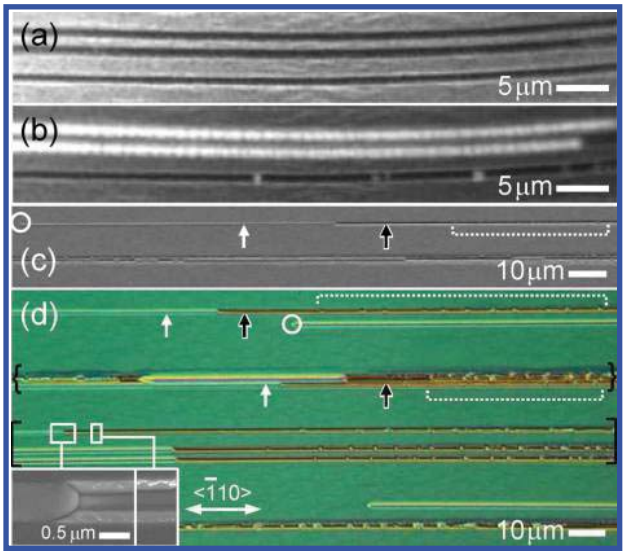

Figure 2. Wires/grooves formed on GaAs(110). (a) LEEM image (E = 0.3 eV) of a selected region showing three parallel trails. (b) UV PEEM image of the same region showing that the top (middle) trail is completely (partially) filled with contiguous droplets each ∼1 μm in diameter, while the bottom trail is only sparingly occupied by droplets. (c) SEM and (d) DIC images of post-sublimated surfaces showing that wires (white arrows) leave behind empty grooves (black arrows) in its immediate vicinity and, a short distance away, grooves that are sparingly occupied by droplets (dotted brackets). Circles mark the tips of wires. In (d), the wires/grooves enclosed in [ ] are well isolated, but those in { } are not and interacted during their formation. The insets in (d) zoom in to show that the width of the groove closest to the wire (left inset) is narrower than those further away (right). The ⟨$\bar{1}$10⟩ direction appears in all images as the horizontal axis.

The behavior of the liquefying fronts depends very much on the width of the bounding structure. For a liquid thread confined in a channel, the narrower the channel, the greater the contact (liquid–substrate) area relative to the surface (liquid–vapor) area. Large surface area has a destabilizing effect, causing liquid threads to break up into similar-sized droplets by Rayleigh instability.[43] Large contact area, in contrast, has a stabilizing effect as it promotes adhesion.[33] This explains not only the contents of the three trails having three different widths in Figures 2a,b but also the contents of trails having slowly varying widths formed when sublimation is terminated as described next.

All liquefying fronts must end, either naturally when they reach the sample edge or prior to that by intentionally cutting off the heating current I_F. In the latter case, long thermal time constants ensure that a liquefying front can still travel a significant distant before T_S drops below T_C, sublimation ceases, and all motions stop. A liquefying front so produced leaves a trail typified by the upper trail in the SEM image in Figure 2c, which exhibits three distinct segments: 1. a groove filled with intermittent droplets (the section highlighted by the dotted bracket), 2. an empty groove (black arrow), and 3. a nanowire (white arrow). Note that the liquefying direction for this particular region of the sample is from right to left. The third segment, the nanowire, is thus the last to form. The circle in Figure 2c marks the end point of the nanowire whose width and length are 200 nm and 80 μm, respectively. The second segment, the empty groove, lies on the same track as the nanowire and has the same width. The first segment contains intermittent droplets, which are not clear in the SEM image in Figure 2c but are obvious in DIC images such as the one shown in Figure 2d. The arrows, the dotted brackets, and the circles in Figure 2c,d highlight the same qualitative structures. The intermittent droplets inside the dotted bracket in Figure 2d are now clearly visible as the contrast is enhanced by interference optics. A few more trails in the middle of Figure 2d (those enclosed in [ ]) also exhibit the same three distinct segments. Closer inspection of the intermittent droplets in these three trails, as well as those in the upper trail, suggests that the droplets in general are smaller and spaced further apart the closer they are to the wires. (Small deviations from this trend are, however, inevitable as the trails traverse a pitted surface.) Since increasing droplet separation indicates a more difficult breakup, or greater liquid–substrate contact area, this means that as liquefying fronts slow down (toward the left of Figure 2d) they are more confined as the constricting channels become narrower, and the break-away droplets get smaller. The two SEM images in the insets taken on the same trail show that the width of the channel next to the wire (left inset) is indeed narrower than those located further away (right). The width of the liquefying front thus affects the content of the trail.

Liquefying fronts especially from the same pit/reservoir are close to one another and may interact if they are not sufficiently

DOI: 10.1021/acs.cgd.7b00707
Cryst. Growth Des. 2017, 17, 4413–4421

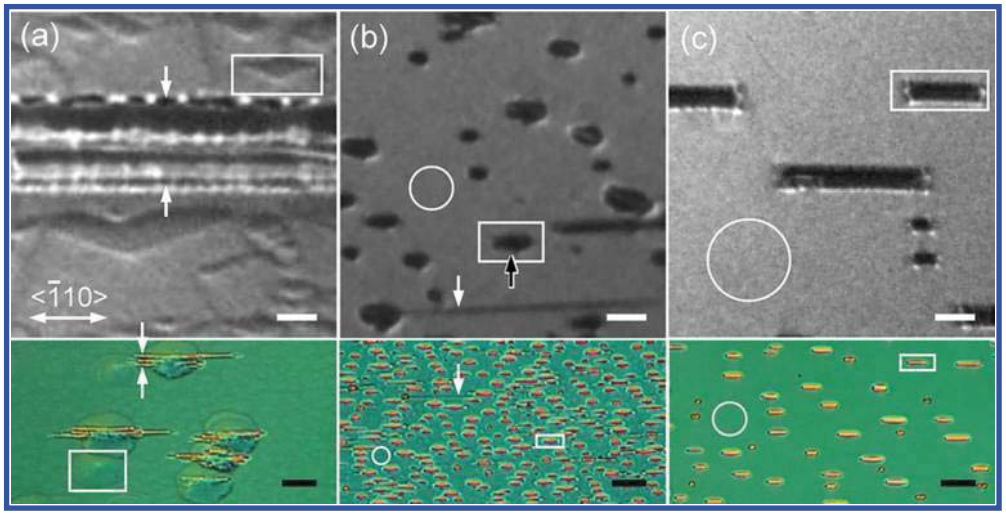

Figure 3. LEEM (upper part, E = 0.2−0.3 eV) and DIC (lower part) images of the (110) surfaces of (a) GaAs, (b) InAs, and (c) InP. The rectangles in (a−c) enclose representative areas of etch pits on each surface, the white arrows in (a,b) point to the nanoscale wires/grooves, the black arrow in (b) points to the nipple discussed in the main text, and the circles in (b,c) highlight the nonpitted areas. Scale bars: white, 2 μm; black, 10 μm. The $\langle\bar{1}10\rangle$ direction appears in all images as the horizontal axis.

separated. When they interact, the resulting morphology can become very complicated, depending on the number of interacting trails and the types of interacting segments. During high temperature sublimation, Ga atoms are very mobile, and despite the recently proposed model of the top few monolayers of liquid Ga being "solid",[44] diffusive transfers of surface atoms between nearby trails must have taken place. In the specific ensemble of trails enclosed by { } in Figure 2d, merging between Ga droplets and between wires on adjacent grooves can be seen, yet the three distinct segments can still be distinguished. In heavily sublimated surfaces, the number of interactions would be so great that no traces of wires and grooves could be identified. Supporting Video V2 contains several instances of trail interaction, showing the complex liquid dynamics as they occur.

The results in this section reveal in detail the transitional structures on sublimating GaAs(110), which include V-bottomed reservoirs, planar wires, and grooves formed without external materials and are naturally aligned in the $\langle\bar{1}10\rangle$ direction. The origin and nature of these self-assembled structures differ significantly from those on GaAs(001) and (111), raising the next logical question: Are these structures specific to GaAs(110), or are they more general?

2. GaAs, InAs, and InP(110). Among the various III−V(110) surfaces investigated, the planar self-assembly of wires and grooves on GaAs are neither the exception nor the rule: It is also found on InAs, but not on InP. To aid visual comparisons, the morphologies of similarly sublimated (110) surfaces of GaAs (T_S = 680 °C), InAs (470 °C), and InP (460 °C) are shown in Figures 3a−c, respectively. These temperatures are slightly higher than the T_C of each surface. In LEEM images in the upper part of the figures, black represents regions occupied by metals (Ga in Figure 3a; In in Figures 3b,c). In DIC images in the lower part, metals appear yellow or golden. The surfaces differ in two main aspects: the thermal etch pits and the running filamentary structures.

First, the etch pits on the three surfaces (representative areas enclosed by rectangles) differ in shapes, sizes, contents, and densities. On GaAs (Figure 3a), the pits take a V shape and appear all over the surface with small amount of Ga spreading inside each pit. The liquid Ga tends to spread due to the low viscosity of molten Ga (0.62 mPa·s)[45] at T_S (680 °C) very much higher than Ga melting temperature (T_m = 30 °C). The pits thus grow principally in-plane, by coalescence, and will ultimately accumulate sufficient materials to reach a critical size, whereby Ga forms droplets and escapes via the liquefying fronts around the peripheries as described in the previous section.

On InAs (Figure 3b), the pits are similarly scattered all over the surface, but the size is smaller than those on GaAs. In each pit, the liquid In tends to form droplets due to the high viscosity of molten In (1.01 mPa·s)[46] at T_S (470 °C) much higher than In melting temperature (T_m = 157 °C). The In droplets are able to etch InAs surface much faster than the Ga droplets are able to etch GaAs surface due to differences in temperature and anisotropic surface diffusion and dissolution. The thermal pits on InAs thus grow in the in-plane and out-of-plane (into the substrate) directions. The pits are circular when small (<1 μm) and rounded rectangular when large. Large pits usually have nipples (black arrow) in the $[00\bar{1}]$ direction as a result of finite etching and subsequent incorporation of In from the slow-etching {111} planes. The nipples do not breakup into separate droplets as the core volume of the droplets elongate in the $\langle\bar{1}10\rangle$ direction. With prolonged sublimation the proportion of the flat, nonpitted areas (circle) decreases as the pits elongate and new droplets/pits are formed.

On InP (Figure 3c), the pits are similar to those on InAs, i.e., they are randomly scattered with flat areas in between, they are filled with In, and they are circular when small (<1 μm) and rectangular when large. The pits grow almost exclusively by elongation along the $\langle\bar{1}10\rangle$ direction. The pits have no nipples, suggesting that the etch rates in the $\langle001\rangle$ direction are symmetrical and are much slower than the $\langle\bar{1}10\rangle$ direction. With prolonged sublimation the flat, nonpitted areas (circle) similarly decrease but remains dominant.

The densities of etch pits on the three surfaces differ due partly to the different T_S required for sublimation and partly to the different nature of oxides and thus oxide desorption. When an oxide desorbs uniformly, the starting surface (before noncongruent sublimation) is smooth; subsequent sublimation would then result in a surface having low-density etch pits and

DOI: 10.1021/acs.cgd.7b00707
Cryst. Growth Des. 2017, 17, 4413−4421

droplets. However, nonuniform oxide desorption would result in high-density etch pits and droplets. The uniformity of oxide desorption depends both on the specific nature of oxides and on the desorption rate. Typically, the greater the desorption rate, the higher the nonuniformity and hence the higher the pit/droplet density. Since the three surfaces are subject to similar temperature ramps, the different densities are attributed mainly to the different nature of the oxides. On InAs(001), it is found that even oxides on "epiready" substrates result in a highly pitted surface that does not provide In droplets sufficient space to run,[32] but when these oxides are etched and replaced by a freshly formed chemical oxide, the latter can be easily sublimated, resulting in a smooth starting surface that provides In droplets ample space to roam.[47]

Second, the running filamentary structures (white arrows in Figure 3) are found on GaAs with greatest density and on InAs at a lower density, but none are found on InP, a trend set by surface roughness. Smooth surfaces have low densities of terraces, ledges, and kinks to which atoms can attach.[48] Energetic atoms on smooth surfaces can thus diffuse with a long mean free time. The smoother the surface, the longer the mean free time, and the greater the diffusion length. On sublimating (110) surfaces that have already nucleated droplets, flat areas would facilitate the growth (elongation) of existing droplets and impede the nucleation of new droplets and liquefying fronts. The availability of flat surfaces scales roughly with the size of the circles depicted in the nonpitted areas in Figure 3: the lowest (none) on GaAs, intermediate on InAs, and the highest on InP.

With maximum flat areas and the lowest pit density, the sublimating InP surface (Figure 3c) allows surface atoms great freedom of movement until they run into droplets. The InP surface thus has the largest, most elongated droplets. The absence of liquefying fronts indicates that the oxides on InP are uniformly and cleanly removed by thermal desorption.

With some flat areas and intermediate droplet density, the sublimating InAs surface (Figure 3b) allows surface atoms some freedom of movement, but the freedom is not great since surface atoms frequently run into droplets. The InAs surface thus has relatively short elongated droplets, with some liquefying fronts formed at local surface inhomogeneities such as pinholes. The liquefying fronts on InAs are elusive as their origin cannot be detected *in situ*, and they occur at low densities: In the LEEM image in Figure 3b only one liquefying front (white arrow) can be clearly identified, whereas in the 96 × 48 μm^2 DIC image, only a few liquefying fronts can be identified, one of which is highlighted by the white arrow pointing to the blurred line.

With no flat areas and the highest pit density, the sublimating GaAs surface (Figure 3a) does not allow surface atoms much freedom of movement. The short adatom diffusion length ensures that Ga atoms are thinly spread across the entire surface, and liquefying fronts can only form when a large number of pits have coalesced, forming V-shaped reservoirs and peripheral droplets as described earlier.

The liquefying fronts on GaAs are much longer than those on InAs due to differences in the background landscapes and how they interact with the invading liquefying fronts. The pits on GaAs are shallow (peak-to-valley height ~5 nm); liquefying Ga fronts (~30−50 nm tall) can thus run through them with ease, forming wires and grooves of great lengths in the process. On InAs, in contrast, the pits are filled with In, which bulges up from the surface by ~50 nm, a relatively large size that easily soaks up approaching liquefying fronts as evidenced by the LEEM image series in Figure 4a−h (see also Supporting Video V3). In Figures 4a−c, a liquefying front (arrows) emerges, runs toward, and merges with droplet *x*; in Figures 4f,g, another front emerges, runs toward, and merges with droplet *y*; and in Figure 4h, droplets *x* and *y* merge, forming droplet *z*. In contrast to these fast-running nanoscale liquefying fronts, the micron scale droplets only slowly elongate or coalesce. Figure 4i is the UV PEEM image of the same area taken after cooldown, confirming the presence of metallic In droplets and wires. An *ex situ* SEM image of a different area shown in Figure 4j captures four typical structures on sublimated InAs surface: 1. a micron scale In droplet, 2. a submicron groove, 3. a nanowire, and 4. a nanogroove. Nipples (black arrows) can also be seen in all micron scale In droplets.

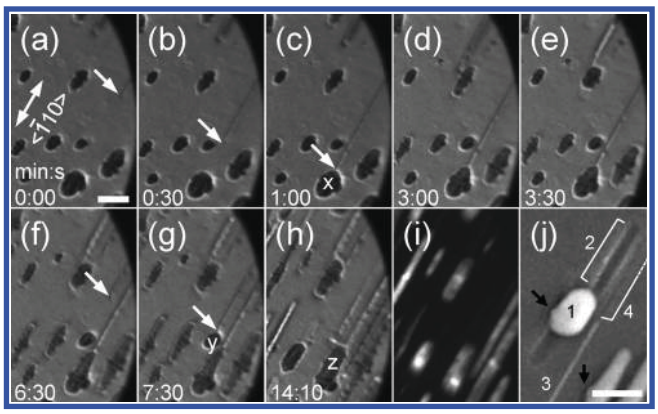

Figure 4. Evolution and interaction of micron-sized In droplets and self-assembled In nanowires during Langmuir evaporation of InAs(110) at 470 °C. (a−h) LEEM images (E = 0.2 eV) of the same area captured during 14 min 10 s. (i) UV PEEM image of the same area after cooldown. Some liquefying fronts, which leave nanoscale trails, are indicated by white arrows in (a−c,f,g). (j) SEM image of a different area showing a typical (1) micron-sized In droplet, (2) submicron groove, (3) In nanowire, and (4) nanogroove. All scale bars are 2 μm. The curved areas to the right of (a−h) are the edges of the imaging plate.

The results in this and the previous sections thus prove that the planar self-assembly of wires and grooves on sublimating III−V(110) surfaces are neither surface specific (present on GaAs and InAs) nor general (not on InP). These wires and grooves are technologically important as they serve as building blocks for various micro- and nanoarchitectures. Their great lengths make them a viable candidate in applications such as diffractive optics, plasmonics, and fluidics, but the self-assembly nature of their fabrication process has a low probability of being applied in mass production for two reasons. First, self-assembly is stochastic. The resulting structures are characterized by random position and a broad size distribution. The latter results in wires and channels having indeterminate diameters in the nanometer to submicron range as seen above. For many applications, wires or channels must be uniform in size and are located at predetermined sites. Second, sublimation is destructive. Though sublimation occurs at the surface, subsurface dopants and interfaces, abundantly found in semiconductor devices, are likely displaced or altered by the high temperature involved. For manufacturing, the process temperature must be low. These two problems, fortunately, can be tackled using the approach described next.

DOI: 10.1021/acs.cgd.7b00707
Cryst. Growth Des. 2017, 17, 4413−4421

3. InP(110) with Surface AuNPs. Taking advantage of Wagner's solid–liquid–vapor (SLV) etching mechanism,[49] the negative counterpart of Wagner and Ellis's VLS growth mechanism,[8] we propose and demonstrate the use of AuNPs as catalysts that are sacrificed to initiate wire self-assembly. The resulting NWs take root from the NPs. NW width is thus dictated by NP diameter. This solves the first problem as NP with well-controlled sizes are commercially available and the technology to place nanoscale structures onto a surface deterministically, for example, by nanoimprint or electron-beam lithography (EBL), exists.[50] Furthermore, NWs form at a lowered temperature, which reduces the second problem.

The proposed sacrificial AuNPs technique to form self-assembled NWs is demonstrated on InP(110), the smoothest and thus the most difficult of the three surfaces to form NWs. Though the following proof-of-principle procedure does not entail the use of deterministic positioning technique such as EBL, its simplicity helps us minimize surface contamination, and the results can be assessed quickly via optical microscopy.

Atomized droplets containing AuNPs (mean diameter 20 nm) are sprayed onto the InP surface and oven-dried before loading into the SPELEEM chamber. The AuNPs cover about 10% of the surface, leaving a large, pristine InP(110) area, which serves as a reference. As the temperature is raised beyond T_C toward 460 °C, the sprayed areas exhibit vibrant activities in stark contrast to the quiet pristine areas. The presence of AuNPs on the surface of the sprayed areas alters the surface chemistry in such a way that decomposition is accelerated, occurring at 5–10 °C lower than the nonsprayed areas. At the NP-populated sites where accelerated decomposition takes place, planar NWs emerge, grow, and even are observed *in situ* (see later).

The NWs so produced are so long and spaced so close together that they can readily be identified by optical microscopy as shown in Figure 5a,b. Figure 5a shows the sublimated InP surface of a sprayed area (labels 1 and 2) and a nonsprayed area (label 3). The perimeter of the sprayed areas 1 and 2 is circular as a result of a spherical, NP-loaded droplet landing on the surface. The division between regions 1 and 2 reflects the different NP densities in a single atomized droplet subject to a stepwise temperature change during oven drying as a means to vary NP density on the same sample. Region 1 has the highest density of NWs and microscopic droplets; Region 2 has lower and 3 much lower NW density. The interface between regions 2 and 3 is demarcated by rectangular droplets. The dashed region in Figure 5a is shown at a higher magnification in Figure 5b, illustrating ensembles of NWs (white arrow) and nanogrooves (black) just outside the sprayed area. The assignment of the light (dark) contrast in the DIC images to NWs (nanogrooves) is confirmed by SEM as shown in a sample image in Figure 5c where a 14 μm-long, 170 nm-wide In NW (white arrow) coexists with a nanogroove (black), which terminates at a rectangular droplet.

The growth of planar In NWs is observed *in situ* and best seen at the interface between the sprayed and the nonsprayed areas (regions 2 and 3, respectively) as shown in the LEEM image series in Figure 5d–g (see Supporting Video V4). Starting from Figure 5d it can be seen that the flat region 3 is separated from the rough region 2 by a row of droplets. Then 4 min 55 s later in Figure 5e two very thin white lines (NWs) emerge, seemingly from the demarcating droplets. The growth fronts of these lines (marked with white arrows) crawl at about the same speed of 1 μm/min as heating continues to 7 min 45 s

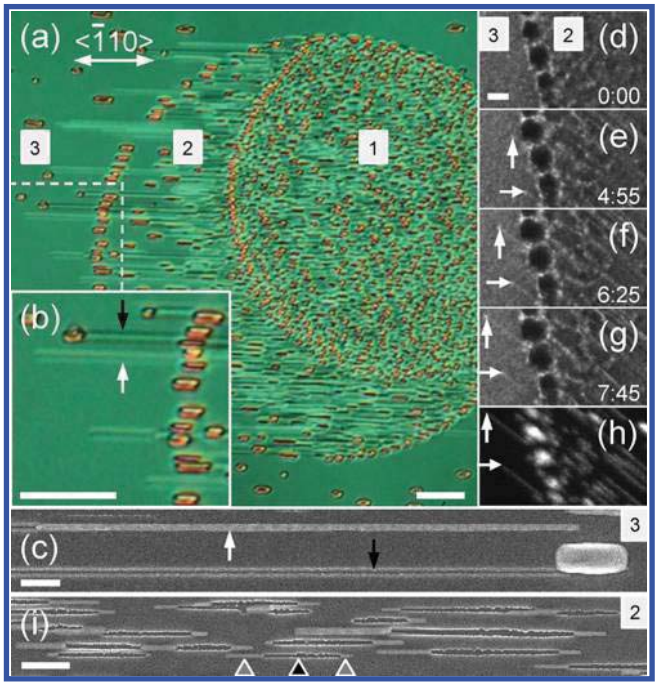

Figure 5. In nanowires and nanogrooves on InP(110) catalyzed by sacrificial AuNPs. (a) DIC image of the post-annealed surface showing regions inside (marked 1, 2) and outside (3) an atomized droplet. (b) Close-up view of the dashed area in (a) where NWs (white arrow) and nanogrooves (black) are prevalent. (c) SEM image of an area in region 3 showing a NW (white arrow) and a nanogroove (black) touching a rectangular, micron-sized droplet. (d–g) LEEM images (E = −0.22 eV) showing the early stages of NW formation at an area bordering regions 2 and 3. The times indicated are in min:s relative to (d). The arrows in (e–g) trace the leading edge of two NWs growing almost identically. (h) UV PEEM image of the same area as those in (g). (i) SEM image of an area in region 2 dominated by long strips each comprising a nanoscale etch pit (▲, dark gray triangle) sandwiched between NWs (light gray triangle). Scale bars: (a,b) 10 μm, (c–i) 1 μm.

as seen in Figure 5f,g. The lines and the demarcating droplets are metallic in nature and are separated as can be seen in the same-area UV PEEM image in Figure 5h. The lines (NWs) thus did not originate from the droplet and are more prevalent in region 2, the sprayed area, than in 3, the nonsprayed area. Far away from the sprayed areas, no NWs exist. Thus, NWs only form where there are AuNPs. Yet unambiguous identification of NW origin cannot be obtained *in situ* due to the limited resolutions imposed by aberrations in low-energy electron optics and by the close proximity of the NPs, which would aggregate to form a cluster as the solution they were in evaporated away during drying. This influences the final yielded structure: the average and the minimum NW widths would increase with aggregation.

The origin of the NWs can be implied, however, using *ex situ* SEM. Focusing on anywhere inside the sprayed area, we found all NWs originate from ⟨1̄10⟩-elongated etch strips as shown in Figure 5i. A typical nucleating strip comprises a central etch pit (black triangle) sandwiched between NWs (gray). This is qualitatively similar to the V-shaped pits and the protruding Ga wires shown earlier in Figure 1i. The In NWs in Figure 5i and the Ga wires in Figure 1i share one important similarity: They emerge from etch pits. Yet in the similarity lies a fundamental difference: The GaAs etch pits are formed solely by heat, necessitating a high surface temperature of at least T_C, but the

DOI: 10.1021/acs.cgd.7b00707
Cryst. Growth Des. 2017, 17, 4413–4421

InP etch pits are formed by thermal *and* catalytic effects, allowing a lower surface temperature. In VLS growth of typical III−V NWs using AuNPs, AuNPs usually remain at the tips of NWs. However, in this case they are absent and instead are replaced by etch pits, indicating a different formation mechanism and that the NPs are sacrificed. (See Supporting Information Figure S1 for morphologies of areas where AuNPs are not sacrificed, and Figure S2 for topographic details correlating the etch depth with the mean diameter of the disappeared NPs.)

The sacrificial role of AuNPs in the etching process and the evolution of wires and grooves can be explained by the schematics in Figure 6. Though an isolated AuNP is shown to

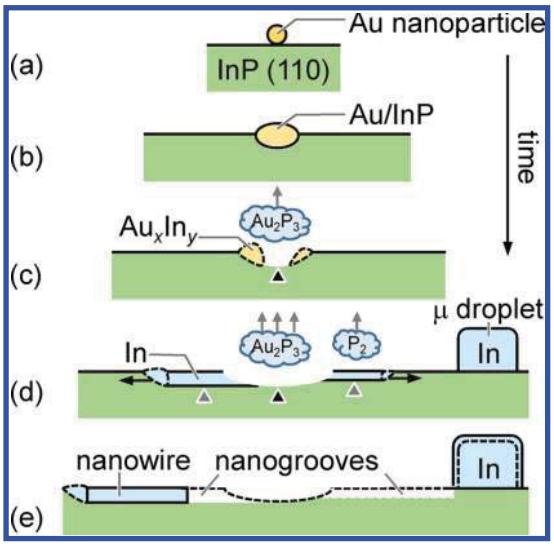

Figure 6. Cross-sectional schematic describing the evolution of AuNP-catalyzed In nanowire and nanogroove as observed in Figure 5. (a) AuNP in contact with InP. (b) AuNP reacts with InP by interdiffusion after which (c) Au_xIn_y alloy is formed before breaking up, leaving an etch pit (▲, dark gray triangle) in between. (d) P continues to diffuse through the alloy, forming volatile Au_2P_3, which after vaporization turns the alloy into pure, liquid In that preferentially etches and advances along the two opposite ⟨$\bar{1}$10⟩ directions (black arrows), creating liquid In NWs (light gray triangle). The left half of (e) illustrates the scenario where the NW advances unobstructed. The right half illustrates the scenario where the NW collides with, and hence is drawn into, a microscopic In droplet, leaving an emptied groove.

be in contact with the InP surface in Figure 6a, in actuality there may be two or more grouped together as is typical in NP-loaded liquid drying. As the substrate temperature increases, the AuNP reacts with and sinks into the InP substrate, forming a Au−InP alloy as shown in Figure 6b. Au is a standard electrical contact to III−V devices and annealed Au−InP ohmic contacts are known to have a rough morphology as a result of etch pits due to material lost,[51] in particular the loss of Au_2P_3, a volatile product of the reaction $2Au + 3InP \rightarrow 3In + Au_2P_3$.[52] The loss of Au_2P_3 and the resulting pit break up the liquid alloy as shown in Figure 6c. As the remaining Au_xIn_y alloy[53] continues to dissolve the substrate, P atoms are incorporated into the alloy resulting in further reaction with Au atoms and the evaporation of Au_2P_3, decreasing the molar fraction of Au and likely transforming the Au_xIn_y alloy into pure liquid In as the latter catapults toward the ⟨$\bar{1}$10⟩ direction as shown in Figure 6d. As In moves away from the nucleating pit, it etches the substrate, which releases P_2.[54] The growth of these In wires is surprisingly sustainable given the daily experience of objects moving through a nonflat surface are likely to be slowed down by friction. *In situ* videos show that this is not the case. Wires are able to grow across the sample if their movements are unimpeded as schematized by the left half of Figure 6e. Many wires, however, would merge with micron scale droplets as schematized by the right half of Figure 6e. At the moment of contact, the liquefying front and the whole body of the wire are quickly drawn into the droplet whose perimeter expands almost instantly (see several collision events in Supporting Video V3), leaving an emptied groove.

The proof-of-principle experiments in this section thus demonstrate the formation of NWs and grooves at random locations using a single type of nanoparticle material having a single average size and a spherical shape. We speculate the following improvements may be made. First, the processing temperature can be reduced further using more reactive catalysts, either by using smaller AuNPs or other NPs that form volatile V-products when in contact with III−V surfaces. AgP_2 is volatile,[55] and Ag could serve as an alternative NP in this regard. Second, it should be possible to create deterministic wires (grooves) using carefully placed AuNPs to initiate (and large microdroplets to terminate) NWs. Third, subsurface dislocation network maybe used to steer the NWs to different directions as dislocation-related stress fields have been shown to be effective at steering even much bigger, micron scale running droplets.[32] The second and third improvements could lead to directed self-assembly and self-integrated nanoscale circuits.[56−58] Finally, the shape of NPs maybe used as an alternative route to control the nucleation and direction of nanowires and grooves. As is often the case with nature, a slight change of shape of the starting nuclei coupled with templated self-assembly can yield final results that are starkly different and complex.[59]

■ CONCLUSION

A planar self-assembly mechanism driving the growth of submicron and nanoscale wires and grooves on sublimating III−V(110) surfaces is observed *in situ* and reported. As a proof-of-principle, AuNPs are shown to be able to accelerate the process, resulting in a decrease in processing temperature and a better geometrical control. The various Ga and In wire and groove morphologies reported here could pave the ways for engineered nano- and microstructures, both in the in-plane and out-of-plane directions, literally pushing the liquid wires and droplets as building blocks toward new directions in fields such as fluidics, plasmonics, optoelectronics, and self-integrated nanocircuits.

■ ASSOCIATED CONTENT

Supporting Information

The Supporting Information is available free of charge on the ACS Publications website at DOI: 10.1021/acs.cgd.7b00707.

Description of the supporting videos, additional images of sublimated InP(110) surface, and topographic details correlating etch depth with NP size (PDF)

Micro- and nanostructure growth dynamics during the sublimation of the (110) surfaces of GaAs (initial stage; AVI), GaAs (intermediate stage; AVI), InAs (AVI), and InP (AVI)

DOI: 10.1021/acs.cgd.7b00707
Cryst. Growth Des. 2017, 17, 4413−4421

AUTHOR INFORMATION

Corresponding Author

*Tel: +66-22186524. Fax: +66-22186523. E-mail: songphol.k@chula.ac.th.

ORCID

Songphol Kanjanachuchai: 0000-0003-4622-4176

Notes

The authors declare no competing financial interest.

ACKNOWLEDGMENTS

Generous access to Elmitec's SPELEEM at Beamline 3.2Ub of the Synchrotron Light Research Institute (SLRI), AuNPs from Prime Nanotechnology Co., Thailand, and technical supports from T. Wongpinij, N. Konkhunthot, N. Jearanaikoon, W. Busayaporn, C. Euaruksakul, and A. Wisitsoraat are gratefully acknowledged. This work is financially supported by Chulalongkorn University, SLRI, and Thailand Research Fund (RSA5880049).

REFERENCES

(1) Lou, C. Y.; Somorjai, G. A. *J. Chem. Phys.* **1971**, *55*, 4554.
(2) Henzie, J.; Lee, J.; Lee, M. H.; Hasan, W.; Odom, T. W. *Annu. Rev. Phys. Chem.* **2009**, *60*, 147.
(3) Pillai, S.; Green, M. A. *Sol. Energy Mater. Sol. Cells* **2010**, *94*, 1481.
(4) Li, X.; Wu, J.; Wang, Z. M.; Liang, B.; Lee, J.; Kim, E.-S.; Salamo, G. J. *Nanoscale* **2014**, *6*, 2675.
(5) Lee, J. H.; Wang, Z. M.; Kim, E. S.; Kim, N. Y.; Park, S. H.; Salamo, G. J. *Nanoscale Res. Lett.* **2010**, *5*, 308.
(6) Heyn, C. *Phys. Rev. B: Condens. Matter Mater. Phys.* **2011**, *83*, 165302.
(7) Yu, P.; Wu, J.; Gao, L.; Liu, H.; Wang, Z. M. *Sol. Energy Mater. Sol. Cells* **2017**, *161*, 377−381.
(8) Wagner, R. S.; Ellis, W. C. *Appl. Phys. Lett.* **1964**, *4*, 89.
(9) Duan, X.; Lieber, C. M. *Adv. Mater.* **2000**, *12*, 298.
(10) Yu, P.; Wu, J.; Liu, S.; Xiong, J.; Jagadish, C.; Wang, Z. M. *Nano Today* **2016**, *11*, 704−737.
(11) Schwarz, K. W.; Tersoff, J. *Phys. Rev. Lett.* **2009**, *102*, 206101.
(12) Schwarz, K. W.; Tersoff, J. *Nano Lett.* **2011**, *11*, 316.
(13) Musin, I. R.; Filler, M. A. *Nano Lett.* **2012**, *12*, 3363.
(14) Tsivion, D.; Schvartzman, M.; Popovitz-Biro, R.; von Huth, P.; Joselevich, E. *Science* **2011**, *333*, 1003.
(15) Fortuna, S. A.; Wen, J.; Chun, I. S.; Li, X. *Nano Lett.* **2008**, *8*, 4421.
(16) Nikoobakht, B.; Wang, X.; Herzing, A.; Shi, J. *Chem. Soc. Rev.* **2013**, *42*, 342.
(17) Xu, M.; Xue, Z.; Wang, J.; Zhao, Y.; Duan, Y.; Zhu, G.; Yu, L.; Xu, J.; Wang, J.; Shi, Y.; Chen, K.; Roca i Cabarrocas, P. *Nano Lett.* **2016**, *16*, 7317.
(18) Curiotto, S.; Leroy, F.; Cheynis, F.; Müller, P. *Nano Lett.* **2015**, *15*, 4788.
(19) Li, S.; Huang, X.; Liu, Q.; Cao, X.; Huo, F.; Zhang, H.; Gan, C. L. *Nano Lett.* **2012**, *12*, 5565.
(20) Mandl, B.; Stangl, J.; Hilner, E.; Zakharov, A. A.; Hillerich, K.; Dey, A. W.; Samuelson, L.; Bauer, G.; Deppert, K.; Mikkelsen, A. *Nano Lett.* **2010**, *10*, 4443.
(21) Bocquet, L.; Charlaix, E. *Chem. Soc. Rev.* **2010**, *39*, 1073.
(22) Snider, G. S.; Williams, R. S. *Nanotechnology* **2007**, *18*, 035204.
(23) Duan, X.; Huang, Y.; Cui, Y.; Wang, J.; Lieber, C. M. *Nature* **2001**, *409*, 66.
(24) Kanjanachuchai, S.; Euaruksakul, C. *Cryst. Growth Des.* **2014**, *14*, 830−834.
(25) Foxon, C. T.; Harvey, J. A.; Joyce, B. A. *J. Phys. Chem. Solids* **1973**, *34*, 1693.
(26) Chatillon, C.; Chatain, D. *J. Cryst. Growth* **1995**, *151*, 91.
(27) Tersoff, J.; Jesson, D. E.; Tang, W. X. *Science* **2009**, *324*, 236.
(28) Kanjanachuchai, S.; Euaruksakul, C. *ACS Appl. Mater. Interfaces* **2013**, *5*, 7709.
(29) Wu, J.; Wang, Z. M.; Li, A. Z.; Benamara, M.; Lee, J.; Koukourinkova, S. D.; Soo Kim, E.; Salamo, G. J. *J. Appl. Phys.* **2012**, *112*, 043523.
(30) Though, strictly speaking, the ⟨$\bar{1}$10⟩ family represents six directions, only two ([$\bar{1}$10] and [1$\bar{1}$0]) are in the (110) surface plane, while the other four ([01$\bar{1}$], [0$\bar{1}$1], [10$\bar{1}$], [$\bar{1}$01]) intersect the plane at an angle and thus are excluded in the discussion.
(31) Gatos, H. C.; Lavine, M. C. *J. Electrochem. Soc.* **1960**, *107*, 427−433.
(32) Kanjanachuchai, S.; Photongkam, P. *Cryst. Growth Des.* **2015**, *15*, 14.
(33) Kumar, G.; Prabhu, K. N. *Adv. Colloid Interface Sci.* **2007**, *133*, 61−89.
(34) Wu, J.; Wang, Z. M.; Li, A. Z.; Benamara, M.; Salamo, G. J. *ACS Appl. Mater. Interfaces* **2011**, *3*, 1817.
(35) Hilner, E.; Zakharov, A. A.; Schulte, K.; Kratzer, P.; Andersen, J. N.; Lundgren, E.; Mikkelsen, A. *Nano Lett.* **2009**, *9*, 2710.
(36) Curiotto, S.; Leroy, F.; Cheynis, F.; Müller, P. *Surf. Sci.* **2015**, *632*, 1.
(37) Datta, S. S. *J. Appl. Phys.* **2010**, *108*, 024307.
(38) Zheng, C.; Tang, W.-X.; Jesson, D. E. *J. Vac. Sci. Technol., A* **2016**, *34*, 043201.
(39) Curiotto, S.; Leroy, F.; Cheynis, F.; Müller, P. *Sci. Rep.* **2017**, *7*, 902.
(40) Nikoobakht, B.; Herzing, A.; Muramoto, S.; Tersoff, J. *Nano Lett.* **2015**, *15*, 8360.
(41) Wallentin, J.; Deppert, K.; Borgström, M. T. *Nanotechnology* **2013**, *24*, 415303.
(42) O'Toole, M.; Boland, J. J. *Appl. Phys. Lett.* **2008**, *93*, 263107.
(43) Lin, S. P.; Reitz, R. D. *Annu. Rev. Fluid Mech.* **1998**, *30*, 85−105.
(44) Phillips, L. F.; Nesbitt, D. J. *Chem. Phys. Lett.* **2012**, *536*, 61−64.
(45) Xiong, L. H.; Wang, X. D.; Yu, Q.; Zhang, H.; Zhang, F.; Sun, Y.; Cao, Q. P.; Xie, H. L.; Xiao, T. Q.; Zhang, D. X.; Wang, C. Z.; Ho, K. M.; Ren, Y.; Jiang, J. Z. *Acta Mater.* **2017**, *128*, 304−312.
(46) Assael, M. J.; Armyra, I. J.; Brillo, J.; Stankus, S. V.; Wu, J.; Wakeham, W. A. *J. Phys. Chem. Ref. Data* **2012**, *41*, 033101.
(47) Dąbrowski, M.; Dai, Y.; Hocevar, M.; Frolov, S.; Petek, H. *Appl. Phys. Lett.* **2016**, *109*, 261602.
(48) Venables, J. *Introduction to Surface and Thin Film Processes*; Cambridge University Press, 2000.
(49) Wagner, R. S. *J. Cryst. Growth* **1968**, *3*, 159.
(50) Schmidt, O. G. *Lateral Alignment of Epitaxial Quantum Dots*; Springer: Berlin, 2007.
(51) Veresegyházy, R.; Pécz, B.; Mojzes, I.; Gombos, G. *Vacuum* **1990**, *40*, 189.
(52) Wada, O. *J. Appl. Phys.* **1985**, *57*, 1901.
(53) Weizer, V. G.; Fatemi, N. S. *J. Appl. Phys.* **1990**, *68*, 2275.
(54) Lowes, T. D.; Zinke-Allmang, M. *Phys. Rev. B: Condens. Matter Mater. Phys.* **1994**, *49*, 16678.
(55) Myers, C. E.; Conti, T. J.; Marley, N. F. *J. Less-Common Met.* **1976**, *48*, 213.
(56) Kumar, P. *Nanoscale Res. Lett.* **2010**, *5*, 1367.
(57) Schvartzman, M.; Tsivion, D.; Mahalu, D.; Raslin, O.; Joselevich, E. *Proc. Natl. Acad. Sci. U. S. A.* **2013**, *110*, 15195.
(58) Oksenberg, E.; Popovitz-Biro, R.; Rechav, K.; Joselevich, E. *Adv. Mater.* **2015**, *27*, 3999.
(59) Ball, P. *The Self-Made Tapestry: Pattern Formation in Nature*; Oxford University Press: Oxford, 2001.

DOI: 10.1021/acs.cgd.7b00707
Cryst. Growth Des. 2017, 17, 4413−4421

Supporting Information

Planar Self-Assembly of Submicron and Nanoscale Wires and Grooves on III-V (110) Surfaces

Songphol Kanjanachuchai[†] *and Pat Photongkam*[‡]

[†]Semiconductor Device Research Laboratory, Department of Electrical Engineering, Faculty of Engineering, Chulalongkorn University, 254 Phayathai Road, Bangkok 10330, Thailand

[‡]Synchrotron Light Research Institute (Public Organization), Ministry of Science and Technology, Nakhon Ratchasima 30000, Thailand

Video V1. Low-energy electron microscopy (LEEM, electron energy E = 0.3eV) video highlighting the surface morphology of sublimating GaAs (110) at the initial stage of wire self-assembly. Snapshots of the video appeared in the main text as Figures 1a-c. The video is created by stitching 12 consecutive images taken at ~30 s interval. The slightly positive electron energy (Start Voltage, V_{st}) provided the best contrast for the V-shaped etch pits in the background, but not the foreground self-assembling wire which emerged in the last frame, unexpected and blurred.

Video V2. LEEM video highlighting the rich dynamics of sublimating GaAs (110) in the midst of wire/groove self-assembling. Snapshots of the video appeared in the main text as Figures 1d-f. The video is accelerated by ~3× (runtime: 1 min 45 s, real time: 5 min) and is created from consecutive images taken at ~1-2 s interval. Note the following when viewing: 1. the field of view changes from 75 μm (scale bar 7.5 μm) to 50 μm (scale bar 5 μm) approximately one-third through the video (i.e. at 10:03:45), 2. image shifts and blurs intermittently as a result of manual sample (manipulator) movements and the inevitable change of optimum focusing condition, and 3. the electron energy E (V_{st} eV) is continually adjusted so as to vary the focus from the background (positive V_{st}) to the foreground (negative V_{st}). Though E varies between −2.5 and 0.7 eV, good quality images are obtained mostly in the 0-0.7 eV range. The video shows i) many newly formed wires emerging from the right and running toward the left side, as discussed in detail and in support of Figure 1 in the main text, and ii) that wires in close proximity interact, resulting in the transfer of liquid metal as discussed in detail and in support of the origin of the wire ensemble shown enclosed in the brackets {…} in Figure 2d in the main text.

Video V3. LEEM video (E = 0.2 eV) of sublimating InAs (110) surface. The rectangle encloses the region of interest which appears in the main text as Figures 4a-h. The video is accelerated by ~40× (runtime: 20 s, real time: 14 min 10 s) and is created from consecutive images taken at ~10-30 s interval. Toward the latter half of the video, droplets are numerous and many have elongated so much that they touch. When two elongated droplets meet, and this can occur head-on (see droplets A and B in Figure S0) or sideway (A and C), part or all of the smaller droplet is usually drawn into the bigger one, resulting in sudden contrast changes. The droplets that gain mass either elongate or bulge up, appearing as rounded rectangles (almost ellipses), with a deep black contrast and thin white strips along the major axis, see label 3 in Figure S0. The droplets that lose mass leave grooves which appear as jagged white lines, see label 2 in Figure S0.

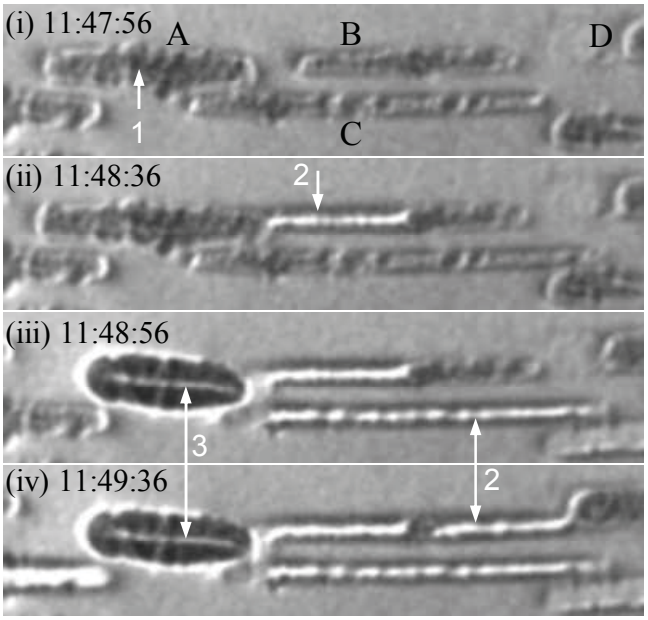

Figure S0. Snapshots taken from Video V3 highligting the different contrasts as droplets A, B, C and D interact:

(i) initial condition, all droplets are quite flat and appear dark grey (label 1).

(ii) A meets B. The left half of B is taken up by A, leaving a groove which appears white (label 2). A elongates.

(iii) A meets C. C is entirely taken up by A. A bulges up (deep black, label 3).

(iv) B meets D. The right half of B is taken up by D. D elongates.

Video V4. LEEM video (E = −0.22 eV) of sublimating InP (110) surface, the upper (lower) part labelled sprayed (non-sprayed) represents a typical area inside (outside) an atomized droplet loaded with Au nanoparticles (AuNPs) which landed on the surface and dried prior to the sublimation experiment. The rectangle encloses the region of interest which appears in the main text as Figures 5d-g. The AuNPs, with 20-nm mean diameter, cannot be resolved in our non-aberration corrected LEEM system.

The catalytic effects of AuNPs cause accelerated decomposition of the InP (110) surface. AuNPs are sacrified in the etching process and nanowires (NWs) are seen to emerge from the resulting etch strips as shown in Figure 5i in the main text. Though the NP disappearance and the NW nucleation are not observed *in situ* due to LEEM's limited lateral resolution, the sacrificial nature of the AuNPs can be deduced from the following observation:

i) AuNPs are completely absent around NWs. Had the AuNPs were present, they would appear much brighter in Figure 5i in the main text. Supporting Figure S1 zooms in on a region where rectangular In droplets coexist with AuNPs. Figure S1c clearly shows that AuNPs are much brighter than In droplets (Au atoms have a greater scattering factor than In atoms), supporting the conclusion drawn in the main text that AuNPs are not present in Figure 5i.

ii) The average etch depth in regions populated by AuNPs is almost the same as the mean diameter of the NPs (20 nm). Supporting Figure S2 shows the WLI height map and a line scan through a section of a sublimated area previously covered by NPs-loaded atomized droplet. The corrugation in and around the center of the atomized droplet is ~20 nm.

The facts that i) AuNPs are absent and ii) replaced by etch pits with an average depth almost identical to the mean diameter of the NPs strongly indicate that AuNPs are sacrified (forming the volatile Au_2P_3) in the etching process.

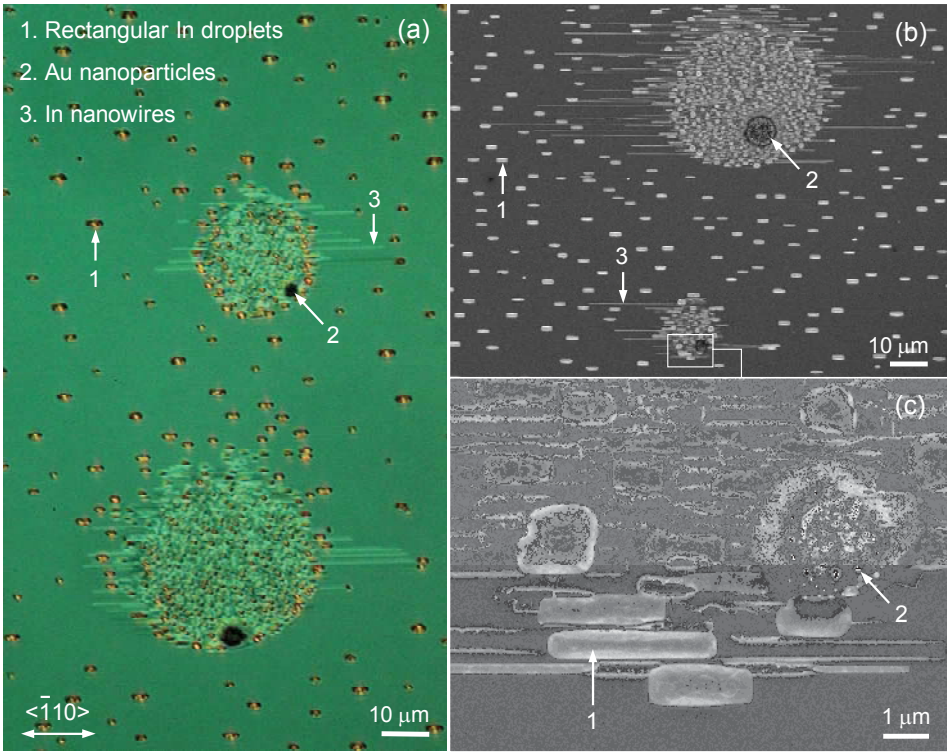

Figure S1. Sublimated InP (110) whose surface was partially covered by atomized droplets containing AuNPs before heating. (a) Differential interference contrast (DIC) image, (b,c) scanning electron microscopy (SEM) images of a different area. For each atomized droplet, high concentration of AuNPs can be found around the spot where the solvent last dried. The AuNPs gravitate toward the bottom half during drying as the sample is not leveled. The AuNP-concentrated spots (label 2) appear dark in DIC images as the spots are highly porous due to NP etching. The SEM images in (b,c) show bright AuNPs in the same vicinity as dark, porous holes resulting from solid-liquid-vapor (SLV) etching as discussed in the main text. Though AuNPs result in In NWs, only a small percentage is seen (label 3) leaving the atomized areas; the majority of NWs either merge among themselves, forming submicron wires, or merge with rectangular In droplets (label 1), leaving grooves.

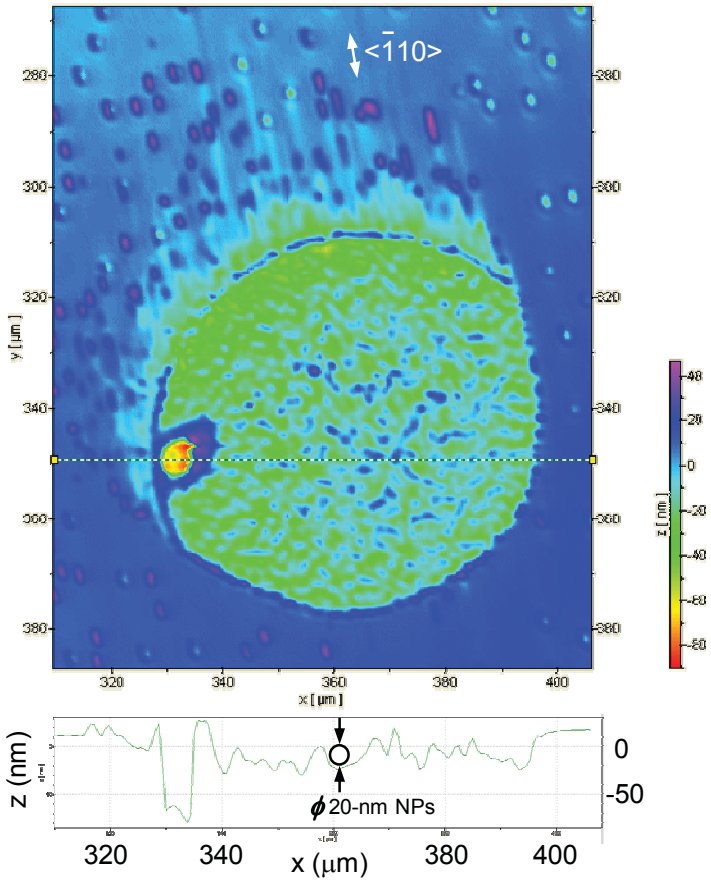

Figure S2. White-light interferometry (WLI) height map of a typical area on InP (110) covered by a AuNP-loaded atomized droplet. The diameter of the atomized droplet is ~70 µm. The mean diameter of the AuNPs is 20 nm. The height profile cuts through the deepest region whose depth is ~80 nm from the surface; this region appears red in the WLI image and corresponds to the dark areas surrounding label 2 in Figure S1. The central segment of the height profile shows that the surface is rough, and the peak-to-valley depth is ~20 nm, the mean diameter of the AuNPs.

ภาคผนวก 3

JOURNAL OF APPLIED PHYSICS **123**, 161570 (2018)

Preferential nucleation, guiding, and blocking of self-propelled droplets by dislocations

Songphol Kanjanachuchai,[1,a)] Thipusa Wongpinij,[2] Suphakan Kijamnajsuk,[3] Chalermchai Himwas,[1,b)] Somsak Panyakeow,[1] and Pat Photongkam[2]
[1]*Semiconductor Device Research Laboratory, Department of Electrical Engineering, Faculty of Engineering, Chulalongkorn University, 254 Phayathai Road, Bangkok 10330, Thailand*
[2]*Synchrotron Light Research Institute (Public Organization), Ministry of Science and Technology, Nakhon Ratchasima 30000, Thailand*
[3]*National Metal and Materials Technology Center, Thailand Science Park, 114 Paholyothin Rd., Klong 1, Klong Luang, Pathumthani 12120, Thailand*

(Received 10 October 2017; accepted 3 January 2018; published online 19 January 2018)

Lattice-mismatched layers of GaAs/InGaAs are grown on GaAs(001) using molecular beam epitaxy and subsequently heated in vacuum while the surface is imaged *in situ* using low-energy electron microscopy, in order to study (i) the nucleation of group-III droplets formed as a result of noncongruent sublimation and (ii) the dynamics of these self-propelled droplets as they navigate the surface. It is found that the interfacial misfit dislocation network not only influences the nucleation sites of droplets, but also exerts unusual steering power over their subsequent motion. Atypical droplet flow patterns including 90° and 180° turns are found. The directions of these dislocations-guided droplets are qualitatively explained in terms of in-plane and out-of-plane stress fields associated with the buried dislocations and the driving forces due to chemical potential and stress gradients typical of Marangoni flow. The findings would benefit processes and devices that employ droplets as catalysts or active structures such as droplet epitaxy of quantum nanostructures, vapor-liquid-solid growth of nanowires, or the fabrication of self-integrated circuits. *Published by AIP Publishing*. https://doi.org/10.1063/1.5008784

I. INTRODUCTION

Elemental metal droplets—particularly the low melting point group-III elements such as Ga and In—have recently gained considerable attention since they are applicable as soft electrical contacts in stretchable/wearable electronics,[1] and they are widely employed in the growth and fabrication of various III-V semiconductor nanostructures such as quantum dots (QD) and rings via droplet epitaxy,[2–4] nanoholes via droplet etching,[5,6] and nanowires (NW) via vapor-liquid-solid growth.[7,8] Once a droplet forms on the surface, it is further processed into an active structure such as QD and NW based on the premise that the position of the final device is the same as those of the starting droplet. If droplets are mobile and their motion can be controlled it may be possible to form self-integrated circuits.[9] Though currently there are no practical means to control the position of liquid droplets after deposition, the droplets under certain circumstances can re-position themselves by the so-called self-propelled or self-running mechanism[10] and this can be harnessed to steer droplets, hence final devices, to desired positions. It must be stated here that self-propelled mechanisms have long been the realm of chemistry with main interest in liquid-liquid systems[11] whereas our interest here lies in liquid-solid interfaces where liquid is limited to the low melting point group-III elements Ga and In, solid to single-crystal III-V semiconductors such as GaAs, and the specific circumstance that leads to the self-propelled motion is Langmuir evaporation, or noncongruent sublimation of III-V surfaces in vacuum. Since the pioneering work of self-running Ga droplets on sublimating GaAs(001) surfaces by Tersoff *et al.*,[10] similar self-propelled droplets have been reported on various III-V surfaces such as GaP, InAs, InSb, and InP and on various orientations.[12–17]

For III-V(001) substrates, the principal direction of self-propelled III,[10] or even non group-III,[18] droplets is [110]. For non-(001) III-V surfaces, the principal running directions vary, dictated mainly by crystallographic orientation.[14,16] For II-VI[9] and IV[19] substrates where self-propelled droplets have been demonstrated, the principal running direction is the same as those found on III-V. Droplets generally prefer to run along the principal direction but as they come across the trails of other droplets they deviate temporarily and only slightly by curving around the obstructing trails.[14] Recently, however, we reported[16] that In droplets running on the (111)B surfaces of InSb and InAs can take sharp, sudden turns from the principal direction—a maneuver which is energetically unfavorable but made possible by the presence of line defects unintentionally formed as a result of plastic relaxation due to mechanical stress. This hints at the possibility of using defects to steer mobile liquid droplets. Relying on a thermomechanical process to create line defects, however, risks irreparable damage as the substrate must be heated while bent, resulting in experiments with low

a)Email: songphol.k@chula.ac.th
b)Present address: Centre de Nanosciences et de Nanotechnologies - site Orsay, UMR 9001 CNRS, Univ. Paris Sud, Univ. Paris-Saclay, Bat 220, rue André Ampère, 91405 Orsay, France

yields, and an unresolved question whether the "self" propelled droplets lend themselves to control, especially by defects.

Using molecular beam epitaxy (MBE) to grow III-V heteroepitaxial films with sufficient misfit to induce interfacial defects, and using low-energy electron microscopy (LEEM) to observe *in situ* the nucleation and dynamics of III droplets on these films, we found that the subsurface line defects not only influence the preferred nucleation sites but also exert control over the dynamics of droplets. In effect, the "self" part of the self-propelled mechanism has diminished importance as the motion is assisted and in some cases dominated by subsurface dislocations. The results to be presented signify the first experimental verification of droplet motion control by subsurface defects in III-V semiconductors. Such maneuver maybe optimized to drive liquids to form grid patterns commonly found in integrated circuits, or even to bounce incoming liquid off—a dynamic with repercussions in fields such as hydrodynamics and earth sciences. After all, exercising control over fluid is a nontrivial task, affecting the survival of many animals and plants,[20] and challenging humankind and civilizations from the earliest historical records.[21]

II. EXPERIMENTAL

The experiments involve the Langmuir evaporation and *in situ* observation of three types of surfaces: (1) epiready GaAs(001) as a controlled surface, (2) a thin InGaAs film grown on epiready GaAs(001), or InGaAs/GaAs for short (referred to hereafter as structure A), and (3) a thick GaAs film grown on InGaAs/GaAs, or GaAs/InGaAs/GaAs for short (structure B).

Epitaxial growth of structures A and B by MBE (Riber's 32P) on epiready GaAs(001) substrates follows the same preparation routine: the substrate is degassed in a preparation chamber, then surface oxides are thermally desorbed at 610 °C in the growth chamber, after which 300-nm GaAs buffer layer is grown at 580 °C. Subsequent layers for structures A and B differ as they serve different purposes. For structure A, a 40-nm $In_{0.15}Ga_{0.85}As$ layer is grown on the GaAs buffer, and growth terminates. For structure B, a 25-nm $In_{0.2}Ga_{0.8}As$ layer is grown on the GaAs buffer, then a 400-nm GaAs layer is grown on the $In_{0.2}Ga_{0.8}As$ layer, then growth terminates. Key growth parameters are temperature of 500 °C, As_4 beam equivalent pressure of 8×10^{-6} Torr, and a nominal V/III flux ratio of 20. Other parameters are typical of III-V arsenides epitaxy and are detailed elsewhere.[22] The InGaAs layers in structures A and B are mismatched to the underlying GaAs substrate and they are thicker than the Matthews-Blakeslee critical thickness θ_c which for $In_{0.15}Ga_{0.85}As$/GaAs is 12.4 nm and for $In_{0.2}Ga_{0.8}As$/GaAs is 8.7 nm.[23] As strain relaxation in (001) heteroepitaxy occurs almost exclusively in the [110] and the orthogonal [1$\bar{1}$0] directions, the InGaAs surfaces appear to have a cross-hatched pattern (CHP) when probed by atomic force microscopy (AFM) or when viewed through a differential interference contrast (DIC) optical microscope. For structure A, the nucleation of droplets on the CHP surface is of interest. For structure B, the dynamics of droplets on the thick GaAs film on the CHP surface is of interest.

To study the nucleation and dynamics of droplets, the three structures are loaded into an Elmitec's LEEM system which allows real-time imaging of surfaces whose backsides are radiatively heated by a tungsten filament. Each sample, mounted on a Mo holder, is pre-heated and left at an overnight standby temperature of ∼200 °C and a base pressure of 2×10^{-10} Torr. To nucleate III droplets, the substrate temperature is ramped up slowly by increasing the filament current I_F. As the temperature reaches a noncongruent sublimation temperature T_C, the III-V surface becomes nonstoichiometric: it loses more of the group V atoms, resulting in an excess of III atoms whose low vapor pressure and melting point allow them to form III droplets. T_C is substrate and orientation dependent: for GaAs(001) it is ∼625 °C,[10] and for $In_xGa_{1-x}As(001)$ it depends on the In molar fraction x and can be estimated by linear interpolation between the GaAs (625 °C) and InAs (440 °C)[24] limits. As each of the sample is heated beyond T_C, the system's pressure increases toward the arcing limit of 10^{-8} Torr. Images are formed either from the low-energy (<5 eV) electrons interacting with the surface (LEEM mode), or from the photoelectrons emitted from the surface by ultraviolet excitation (PEEM mode), or from both types of electrons (PEEM/LEEM mode). While LEEM provides better topographic contrast, PEEM enables workfunction contrast, hence the ability to differentiate III metallic droplets from III-V semiconducting background. In addition to *in situ* LEEM and PEEM, the samples are also studied *ex situ* using scanning electron microscopy (SEM) with energy-dispersive X-ray spectroscopy (EDS). The degrees of misfit of the InGaAs layers are assessed before and after Langmuir evaporation using high-resolution X-ray diffraction (HR-XRD).

III. RESULTS AND DISCUSSION

The results are divided into four subsections. Section III A aims to establish that surface droplets prefer to nucleate on misfit dislocations over flat surfaces. Section III B shows how and explains why dislocations may guide or even block approaching droplets. Thus, Sec. III A concerns the statics, whereas Sec. III B concerns the dynamics aspects of the droplets. Section III C reports unusual motion behaviors. Finally, Sec. III D describes the states of the misfit layers before and after droplet nucleation.

A. Preferential nucleation of droplets on dislocations

Dislocations in single crystals are regions where lattice periodicity is locally disrupted, creating lattice distortions or strain fields emanating in all directions.[25] When close to the free surface, the fields can cause enhanced surface reactivity for both additive (growth) and subtractive (etching) processes. Since the formation of III droplets on III-V surfaces by Langmuir evaporation occurs in conjunction with etching, it is hypothesized that droplet nucleation can be enhanced by dislocation-related strain fields, and thus, it should be possible to influence or even control the positions of droplets. So far, there exists only one report of III droplet control on

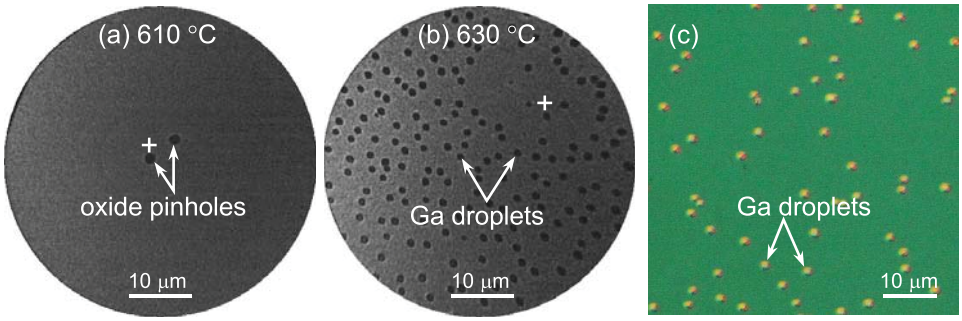

FIG. 1. Formation of Ga droplets upon noncongruent evaporation of GaAs(001) surfaces in vacuum. *In situ* LEEM images (electron energy $E = 0.5$ eV) showing the surface (a) before and (b) after droplet formation. The droplets appear black in LEEM. The + symbol in (a) and (b) marks the same reference position which slightly shifts as the sample drifts during heating. (c) *Ex situ* DIC image of the post-annealed surface of another sample subject to a slower temperature ramp rate. The droplets appear yellow/golden in DIC.

III-V surfaces, using oxide pinholes,[26] but the nature of control is temporal, not spatial. The results in this subsection, in contrast, demonstrate the first successful spatial control of droplets formed by a subtractive process—using a misfit dislocation network intrinsic to structure A.

The results will be explained in the following order. First, random droplet distribution on the controlled surface will be shown, followed by non-random droplet nucleation on the surface of structure A. Finally, a potential application of droplets as a means to decorate dislocations is proposed.

The controlled surface, i.e., epiready GaAs(001), is flat. Sublimating it in vacuum always results in random distribution of Ga droplets. Figure 1(a) shows the LEEM image of the surface at 610 °C, below T_C and before droplet nucleation. The + sign marks the reference/focusing position; the two black features nearby are pre-existing oxide pinholes. As the temperature increases, the oxide is desorbed and Ga droplets emerge. Figure 1(b) shows the LEEM image of the same area (slightly shifted due to thermal drifts) at 630 °C, above T_C and thus a significant number of micron-sized Ga droplets can be seen. The Ga droplets appear in LEEM as black circular features, similar to pinholes. The Ga droplets in Fig. 1(b) are dense and randomly distributed. For GaAs(001) surfaces which are sublimated at the same temperature for a shorter duration, or at a lower temperature (but above T_C) for the same duration, the density of droplets will drop. This is illustrated in the DIC image of a lightly sublimated surface in Fig. 1(c) where reflective metal droplets appear yellow/golden. Thus from Figs. 1(b) and 1(c) it is evident that, regardless of the stages of nucleation, Ga droplets on the controlled surfaces are distributed randomly. It is not possible to predict the droplet nucleation sites on flat GaAs(001).

For structure A, or InGaAs/GaAs, predicting the early positions of droplets on the sublimating InGaAs surface is possible. To understand how this is possible yet is limited to the early stages, it is necessary to understand the nature of the InGaAs layer. Grown by epitaxy, the InGaAs layer is partially relaxed and its surface is not perfectly flat: a cross-hatched pattern in the form of orthogonal lines in the [110] and [1$\bar{1}$0] directions appear as seen in the LEEM image in Fig. 2(a). These lines protrude from the otherwise flat surroundings with heights, measured by AFM, in the order of 1 nm.[27] The × sign in the figure marks the reference/focusing position. Dislocation lines which are well separated are indicated with single-lined arrows (→), while those that appear close to one another are collectively represented by double-lined arrows (⇒).

As the temperature increases beyond $T_C \sim 600$ °C for $In_{0.15}Ga_{0.85}As$, the InGaAs surface becomes nonstoichiometric and is populated by In_xGa_{1-x} droplets. The In molar fraction (x) of the final droplets is below the detection limit of SEM-EDS which means that the droplets are predominantly Ga, consistent with theoretical prediction based on thermodynamics.[28] The droplets first emerge along the dislocations, and shortly after on the flat surroundings. This is observed

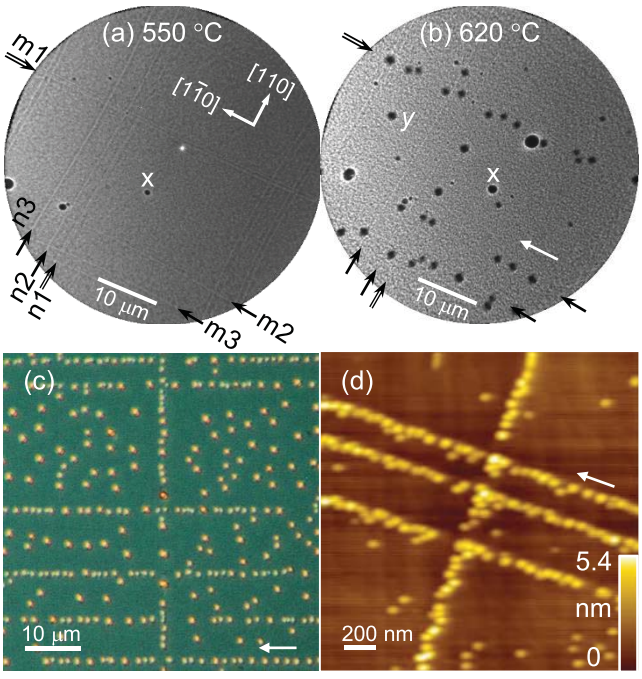

FIG. 2. Dislocation-enhanced nucleation of (a)–(c) droplets upon sublimation of InGaAs/GaAs (structure A), and (d) QDs upon overgrowth on structure A. LEEM images ($E = 0.5$ eV) show (a) the orthogonal dislocations m_i and n_i in the [1$\bar{1}$0] and [110] directions, respectively, and (b) preferential nucleation of droplets on dislocations. The × symbol in (a) and (b) marks the reference position. The letter y in (b) marks a droplet not nucleated on dislocations. (c) DIC image of the surface of structure A after sublimation. (d) AFM image of the surface of A after the growth of InAs QDs. Dislocations are the preferred nucleation sites for droplets and QDs alike. The white arrows in (b)–(d) point in the [1$\bar{1}$0] direction.

in situ and at 620 °C many of the dislocation lines in Fig. 2(a) are decorated with droplets as shown in Fig. 2(b). This behavior is qualitatively the same as those observed in solid-state dewetting using templates.[29]

Droplet nucleation on the [110] and [1$\bar{1}$0] dislocations is anisotropic. The [1$\bar{1}$0] dislocations such as m1-m3 in Fig. 2(b) are decorated with many droplets. In contrast, the [110] dislocations such as n1-n3 are decorated with only a few droplets. Droplets thus prefer to nucleate along the [1$\bar{1}$0] over the [110] dislocations. Closer inspection of Fig. 2(b) indicates that even dislocations in the same direction do not have the same nucleation probabilities. Closely spaced dislocations are better able to nucleate droplets than well-separated dislocations: In the [1$\bar{1}$0] direction, it is seen that dislocation m1 has more droplets per length than m2 or m3, and in the [110] direction, n1 has more droplets per length than n2 or n3. In fact, the [110] dislocations seem to be able to nucleate droplets better when they intersect [1$\bar{1}$0] dislocations, suggesting that droplets that are located at intersections are due more to the [1$\bar{1}$0] than the [110] dislocations. While the majority of [110] dislocations are still void of droplets, some droplets already emerge on flat surfaces; for example, see droplet *y* in Fig. 2(b). Thus it can be concluded that, in general, droplets prefer to nucleate on—with decreasing probability—[1$\bar{1}$0] dislocations, the flat regions not traversed by dislocations, and [110] dislocations. This is more evident in the DIC image in Fig. 2(c) which shows a much greater number of densely populated dislocation lines in the [1$\bar{1}$0] than the [110] directions.

The preferential nucleation of droplets along one dislocation direction is surprising. Why should [1$\bar{1}$0] dislocations be preferred over the flat surface, while [110] dislocations are discriminated against? Dislocations are known to cause strain fields which, for epitaxy, drive surface atoms toward them indiscriminately. Figure 2(d) shows the AFM topography of a surface obtained by growing InAs QDs on the surface of structure A. The QDs populate areas along the orthogonal dislocations without discrimination regardless of the thickness and In fraction in the InGaAs layer.[30] Even thin two-dimensional platelets have been shown to similarly populate the orthogonal dislocations.[31]

To understand the physical origin of the preferential nucleation of droplets along the [1$\bar{1}$0] over the [110] dislocation, it is necessary to consider the combined effects of dislocation-related strain fields and anisotropic diffusion of surface atoms. The surface stress fields arise from the subsurface dislocation core 40 nm below, at the InGaAs/GaAs interface. As one side of the dislocation is under compression and the other is under tension (with respect to the dislocations-free areas), the V atoms along the compressive side of the dislocation will be sublimated at a greater rate than those on the dislocation-free area, leaving III atoms to line up on the surface immediately above the dislocations. This is due to the increase (decrease) in the binding energy of adatoms to the underlying layer when the latter is under tension (compression).[32] If these atoms linger, they will aggregate and form droplets to reduce surface energy. But if they diffuse away quickly, few or no droplets will be observed. The strong presence of III droplets on [1$\bar{1}$0] dislocations and the near absence on [110] dislocations [see Figs. 2(b) and 2(c)] thus indicate that once III atoms are freed along [1$\bar{1}$0] dislocations they do not migrate far from their original sites, but if they are freed along [110] dislocations they would diffuse away quickly. This lopsided behavior is due to anisotropic diffusions of surface Ga atoms: the diffusion coefficient along [110] is greater than [1$\bar{1}$0], and the disparity increases with temperature.[32,33] The Ga atoms freed from the surface above the [110] dislocation will thus diffuse toward those lingering on the orthogonal [1$\bar{1}$0] dislocation or the flat region, until a sufficient number of atoms arrive to nucleate droplets. This explains why at a relatively low growth temperature of 500 °C, QDs equally populate the [110] and [1$\bar{1}$0] dislocations as seen in Fig. 2(d), but at a high sublimation temperature of 620 °C, droplets prefer to populate the [1$\bar{1}$0] dislocation.

When micron-sized droplets decorate dislocations, they allow standard optical microscopes to identify buried dislocations with ease, even without interference contrast enhancement. This serves as a great utility for heteroepitaxy of novel materials where quick assessments of crystalline quality are needed more often than detailed defect analyses which necessitate the use of transmission electron microscopy (TEM) and thus destructive and time-consuming sample preparation. This utility is particularly suited to low-mismatched heteroepitaxy as dislocation density is low, making analyses by TEM impractical due to the limited field of view. To illustrate the power of this approach in the identification of defects in low-mismatched areas, a few sample cases are given below.

Figure 3(a) shows the DIC image of a wide area having nine [1$\bar{1}$0] dislocation lines L1-L9. Most lines traverse the entire horizontal length, except L4 and L8 which are terminated near the vertical center of the figure. Zooming in on the boxed region of L4, upper inset, one finds an oval defect caused by Ga spit during the growth of the InGaAs epilayer.[34] This defect could help the strain to relax at the InGaAs/GaAs interface, injecting dislocation lines on both sides, possibly serving as the source of L4. The boxed region of L8, middle inset, is either an edge dislocation or a threading dislocation that terminates at the surface. The dislocation could originate from a pre-existing dislocation in the substrate or from the growing film such as when a half-loop dislocation is formed. Regardless of the source, it is clear that dislocation terminations can be easily identified and can be used to study various aspects of dislocation nucleation and interaction.

Linear and non-linear dislocations are equally susceptible to such decoration. Figure 3(b) shows another wide area DIC image having three dislocation lines L10-L12, and one curved dislocation L13 which terminates at an oval defect pair shown expanded in the inset. The droplets associated with the two oval defects have merged, creating a single, elliptical droplet which possibly serves as a Frank-Read multiplication source given the curved character of L13.

These examples merely illustrate the ease of droplet decoration, the clarity of the results, and the potential benefits to dislocation studies. By no means can these surface morphologies alone describe the true nature of buried

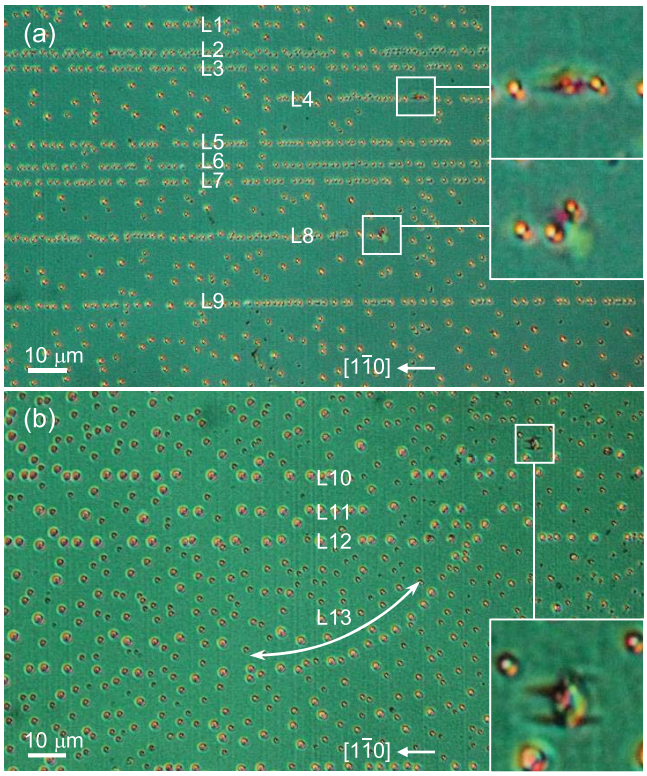

FIG. 3. Decoration of dislocations by droplets as seen on the sublimated surface of structure A. DIC images illustrate increased droplet density along (a) [1$\bar{1}$0] dislocations L1-L9 and (b) [1$\bar{1}$0] dislocations L10-L12 and curved dislocation L13. The insets are expanded views around (a, upper inset) an oval defect, (a, lower inset) a dislocation termination, and (b) a pair of oval defects.

dislocations, however. Without corroborating with independent data, particularly with Burgers vector analyses by TEM which are beyond the scope of this work, the above explanation regarding the nature of the dislocations in Figs. 3(a) and 3(b) remains speculative. Nevertheless, the power of the technique to simultaneously decorate misfit, threading, and edge dislocations—the most common dislocation types in heteroepitaxy—makes it highly appealing as a complementary technique for dislocation studies.

Dislocation decoration by droplets has one important limitation: it is applicable only during the early stages of noncongruent sublimation. If overly sublimated, the droplets on the surface would enter late-stage coalescence.[35] The surface would be filled with randomly distributed droplets of all sizes. Statistical analyses of droplet densities and the identification of individual dislocations from droplets would then be very difficult or impossible. The narrow temperature and time windows severely restrict quantitative studies such as the temperature dependence of the droplet nucleation imbalance between the [110] and [1$\bar{1}$0] directions.

B. Guiding and blocking of running droplets by dislocations

Given time and energy (sustained heating), the droplets described above will grow as they incorporate more III atoms from in-plane diffusion and from the dissolution of the underlying liquid-solid (droplet-substrate) interface. Finally, they will attain a critical size and move in the principal direction which for (001) surfaces is [110]. Diversion from this principal direction has been reported for daughter or secondary droplets formed along the trails left by primary droplets which have moved in the principal direction, leaving secondary droplets to move orthogonally, but briefly, before returning to the principal direction.[36] Such diversion is, however, not by design as primary droplets still run in the principal direction. Here, the first experimental results of primary droplets that, by design, deviate from this trend are demonstrated using structure B.

The results will be explained in the following order. First, the motion of droplets along a single principal direction on the controlled surface will be shown, followed by the motion of droplets along two principal directions on the surface of structure B. Some surprising motion patterns are found and will be explained in Sec. III C. It is implicit that the following results are observed, while surfaces are held at temperatures $T > T_C$ throughout.

On the controlled surface, GaAs(001), as Ga droplets grow and reach a diameter of $\sim 2\,\mu$m, they will all run along one principal direction, [110], as seen in the LEEM image in Fig. 4(a). Droplets appear black in the figure. The driving force F_μ responsible for the self-propelled motion of droplets is due mainly to chemical potential gradient $\Delta\mu$,[10] assisted by surface reconstruction,[37,38] atomic steps elimination,[12,39] and crystallographic etching.[14,16,19] The majority of droplets in Fig. 4(a) run to the right, i.e., [$\bar{1}\bar{1}$0], while the minority run to the left, i.e., [110]. The degree of imbalance varies

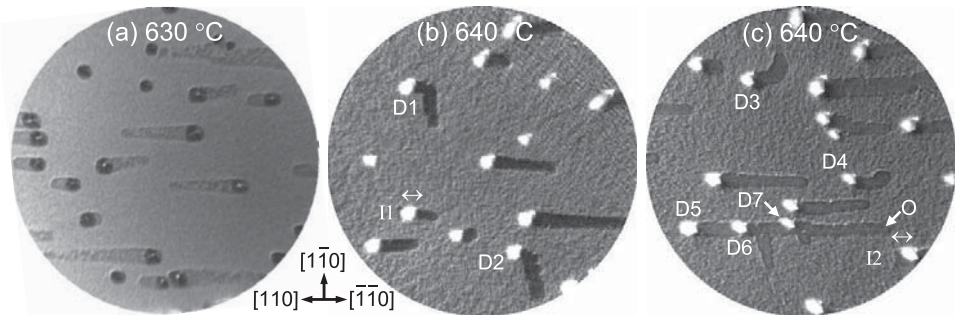

FIG. 4. *In situ* electron images of self-propelled Ga droplets on (a) GaAs (controlled surface) taken in LEEM mode ($E = 0.3$ eV), (b) and (c) GaAs/InGaAs/GaAs (structure B) taken in PEEM/LEEM mode ($E = 0.04$ eV). The movements of droplets D1-D7 and I1-I2 in (b) and (c) are described in the main text. Due to sample tilt and non-optimized imaging conditions, the images in (b) and (c) are slightly distorted in the [1$\bar{1}$0] direction. Field of view: (a) 25 μm, [(b) and (c)] 50 μm.

from wafer to wafer and is due to a slight miscut (±0.5° according to the wafer's supplier). For perfect on-axis surfaces (miscut ±0.1°), droplets would run equally in both directions.[10] Regardless of the degrees of miscut and motion imbalance, all primary droplets on GaAs(001) run along the [110] principal direction.

On structure B, or GaAs/InGaAs/GaAs, primary droplets on the top GaAs surface run in two principal directions, [110] and [1$\bar{1}$0], as seen in the PEEM/LEEM image in Fig. 4(b). Droplets appear bright, reflecting the large number of photoelectrons from Ga contributing in the PEEM mode. From the start, the majority of droplets run to the left, i.e., [1$\bar{1}$0], but two droplets (D1 and D2) run to the top, i.e., [1$\bar{1}$0]. The high-contrast background in Fig. 4(b), obtained in the LEEM mode, serves to affirm that the movement of D1 and D2 along [1$\bar{1}$0] is not due to scratches, surface roughness, or topographical defects of any kind. The importance of this simple-looking result lies in the fact that [1$\bar{1}$0] is energetically unfavorable on flat GaAs(001) yet is, from the start, the preferred direction of droplets D1 and D2 on structure B. This means that both droplets must be guided by out-of-plane forces stronger than the in-plane force F_μ which would have otherwise driven them in the [110] direction. The out-of-plane forces, however, have temporary effects as Fig. 4(b) shows that after D1 and D2 have been guided up for ∼7 μm, they turn left, joining other droplets in running toward the [110] direction. Two questions immediately come to mind: What pushes the droplets up in the first place, and why the droplets switch direction shortly after?

Since the only difference between the controlled surface (GaAs) and structure B (GaAs/InGaAs/GaAs) is the partially relaxed InGaAs layer, specifically the misfit dislocation network at the InGaAs/GaAs interface, the latter thus must play the central role in pushing the surface Ga droplets up the [1$\bar{1}$0] direction. To understand how this is possible and why only temporarily, the stress fields around orthogonal dislocations and their effects on approaching droplets will be discussed next.

Orthogonal dislocations are merely a network of dislocation intersections each comprising a [110] dislocation intersecting a [1$\bar{1}$0] dislocation at a point. Since in zinc-blende crystals each of the [110] and [1$\bar{1}$0] dislocations can have four possible Burgers vectors, the stress around an intersection can take 16 different forms, though some are redundant by symmetry.[40] To illustrate, the stress map of the surface above a hypothetical intersection between a [110] dislocation with Burgers vector $\mathbf{b} = \frac{1}{2}$ [$\bar{1}$01] and a [1$\bar{1}$0] dislocation with $\mathbf{b} = \frac{1}{2}$ [011] is shown in Fig. 5(a); the intersection is at the center. The surface stress σ_{yy} ($x = 0$) is given in units of $10^{-3}G$ where G is the shear modulus of the film. The simulation geometry is shown in Fig. 5(b) and the material is assumed to be isotropic for simplicity. The orthogonal dislocation lines (⊥) are buried at the InGaAs/GaAs interface, 400 nm below the surface. Typically, for each dislocation line located at a depth h below the surface, the surface stress can be determined analytically from[41]

$$\sigma_{yy} = \frac{4G}{\pi(1-\nu)} \frac{yh\left(b_\perp h - b_{//} y\right)}{\left(y^2 + h^2\right)^2},$$

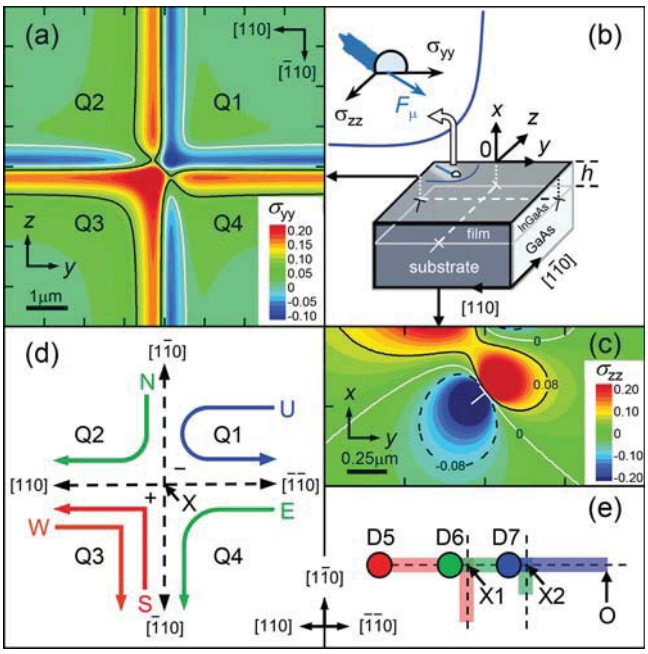

FIG. 5. Stress fields and their effects on self-propelled droplets. (a) Map of surface stress above a hypothetical dislocation intersection in the center of the figure between a [110] dislocation with Burgers vector $\mathbf{b} = \frac{1}{2}$ [$\bar{1}$01] and a [1$\bar{1}$0] dislocation with $\mathbf{b} = \frac{1}{2}$ [011]. (b) Schematic cross-sectional drawing of the simulated geometry showing dislocations running in the [110] direction (black ⊥ symbols) and [1$\bar{1}$0] directions (white ⊥ symbols). The self-propelled droplet and the forces acting on it are detailed in the inset. The in-plane stress on the surface plane σ_{yy} (z-y coordinates) is shown in (a), while the out-of-plane stress σ_{zz} for the [1$\bar{1}$0] dislocation (x-y coordinates) is shown in (c). The grey scales of the stresses σ_{yy} and σ_{zz} in (a) and (c) are in units of $10^{-3}G$ where G is the shear modulus of the film. (d) Schematic drawing showing the running paths N, E, W, and S taken by droplets on the surface in (a) running toward the intersection X from the north, east, west, and south, respectively. Path U means a U-turn. The + and − signs in (d) indicate roughly the positions in quadrants Q3 and Q1 with maximum compressive and tensile stresses, respectively. (e) Schematic drawing showing the current positions and trails of droplets D5-D7 in Fig. 4(c), highlighting the strong guiding effects of the underlying dislocations (dashed lines).

where ν is the Poisson ratio, y is the distance from the dislocation, and $b_{//}$ and $b_\perp$ are the Burgers vector components parallel and perpendicular to the interface, respectively. The stress map in Fig. 5(a), obtained by the superposition of the orthogonal stress fields, shows that the region around the intersection comprises four quarters (Q1-Q4) with three qualitatively different profiles looking into the intersection: 1. Q1 is bounded by orthogonal lines having negative stress (blue, under tension), 2. Q3 is bounded by orthogonal lines having positive stress (red, compression), and 3. Q2 and Q4 are bounded by orthogonal lines having opposite stress signs.

The effects that stress fields from multiple dislocations have on a droplet can be estimated from the superposition of the effects from individual dislocations where each dislocation exerts on an approaching droplet a stress-dependent force tensor F_σ with in-plane (σ_{yy}) and out-of-plane (σ_{zz}) components.[16,41] σ_{yy} is shown in Fig. 5(a). σ_{zz} for [1$\bar{1}$0] dislocation is shown in Fig. 5(c); σ_{zz} for [110] is similar in form (not shown). The colors in Figs. 5(a) and 5(c) reflect the stress state and are thus indicative of motion: Red (blue) represents regions under compression (tension) toward which droplets accelerate (decelerate) as a result of Marangoni flow

driven by stress gradients.[42] Under the sole influence of in-plane components σ_{yy}, if a droplet approaches the $[1\bar{1}0]$ dislocation in Fig. 5(a) from the compressive (left hand) side it will be further driven toward the dislocation by the combined effects of σ_{yy} (Marangoni effects) and F_μ (chemical potential effects). But if the droplet approaches the dislocation from the tensile side, it could be halted, deflected, or even reflected (see later). The influence of the out-of-plane stress σ_{zz} on a droplet is more complicated. The cross-sectional profile of σ_{zz} in the x-y plane in Fig. 5(c) shows that as a droplet approaches the point immediately above the dislocation core ($\perp$) the base of the droplet will experience stress reversal along the zero-stress contours on both sides of the dislocation. This means that for a droplet approaching the $[1\bar{1}0]$ dislocation from the left hand side σ_{zz} will first attract it, only to later stop and possibly push it away by repulsion from below [the lower zero-stress contour in Fig. 5(c)] and the right hand side (upper). In the case that droplets are nucleated immediately above the dislocation core, they will be bounded by these zero-stress contours and once they reach a critical size they will thread along the dislocation, i.e., run in the $[1\bar{1}0]$ direction. This describes the behaviors of D1 and D2 in Fig. 4(b) during their early stages, before they run into an intersection.

When a droplet approaches a [110]-$[1\bar{1}0]$ dislocation intersection, it will have to navigate through a complex stress terrain. Considering that surface atoms are likely to collect along the compressive side of dislocation lines, droplets thus generally approach an intersection from four directions. Using the stress map in Fig. 5(a) as an example, the following four scenarios and the accompanying diagram in Fig. 5(d) describe how a droplet nucleated on the compressive area (red) is affected by the underlying stress as it approaches the intersection from the:

1. South, or $[\bar{1}10]$. By virtues of σ_{yy}, the droplet will feel a strong attractive force toward the darkest red spot (hereafter red peak, marked +) in Q3, but only slightly ahead it will feel an equally strong repulsive force centered at the darkest blue spot (blue peak, −) in Q1. In addition, the droplet is attracted to the left by the orthogonal dislocation line. Keep in mind that while in motion, the direction of F_μ acting on the droplet is the same direction as the trail. The least resistant path for this droplet to take is thus the right-angled, red segments in Q3, schematically shown by the path S in Fig. 5(d). This is the motion pattern of droplets D1 and D2 in Fig. 4(b).
2. North, or $[1\bar{1}0]$. As the droplet moves toward the intersection, the driving force that keeps the droplet on the $[1\bar{1}0]$ dislocation decreases but the force pushing it sideway (from Q1) increases. It thus moves sideway into Q2, unable to cross over to Q3 as it is blocked by the repulsive stress wall at the Q2-Q3 dividing line. In this case there is no sharp, continuous stress boundary as in the previous case and the droplet only turns slowly and continuously as shown schematically by the path N in Fig. 5(d). This is the motion pattern of droplets D3 and D4 in Fig. 4(c).
3. East, or $[\bar{1}\bar{1}0]$. The stress field in Q4 is the mirror image of those in Q2 (NE-SW line as the mirror plane), thus by symmetry a droplet in Q4 running to the intersection should behave in the mirrored manner as a droplet in Q2 running to the same intersection: it should slowly bend toward the South as shown by the path E in Fig. 5(d). Most large droplets running from East to West in Fig. 4(c), however, are not deflected but run through intersections. This indicates that droplets which move in the [110] direction toward the intersection are driven by a force $F_{\mu m}$ sufficiently large to push them over the repulsive stress wall. Such a large force is likely due to substrate miscut which introduces extra surface steps that create motion imbalance in the [110] direction in the first place. The subscripts μ and m in $F_{\mu m}$ represent and thus acknowledge the importance of chemical potential μ and the miscut, respectively. Although absent in Figs. 4(b) and 4(c), the motion pattern following the path E is present in Fig. 6 to be described later.
4. West, or [110]. Again by symmetry, a droplet moving from the West to the intersection should take a right-angled, right turn to the South, mirroring a droplet moving from the South which takes a right-angled, left turn to the West. The mirrored paths W and S are shown schematically in Fig. 5(d). This motion pattern will be evident in Fig. 6 to be described later.

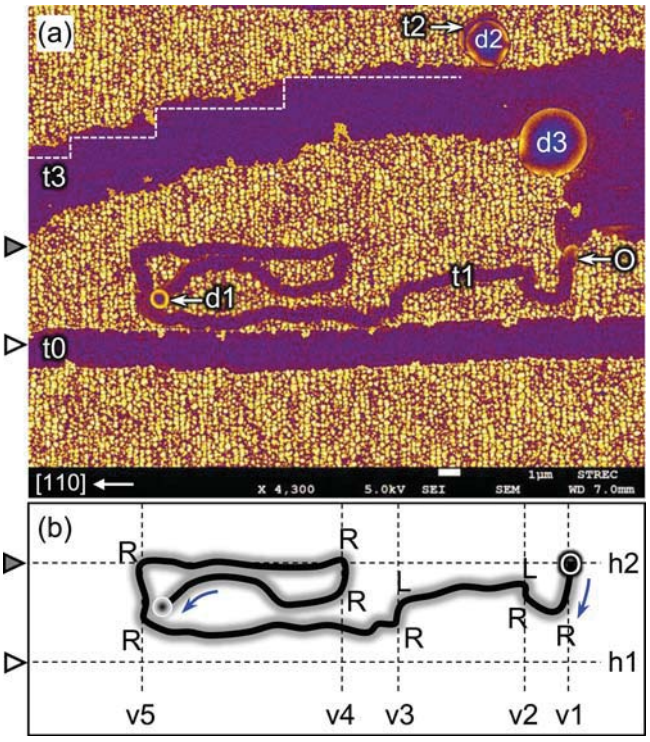

FIG. 6. Dislocations and their effects on small (d1), medium (d2), and large (d3) running droplets. (a) SEM micrograph of a selected area on the surface of structure B after sublimation. Prominent features include bright Ga nanodroplets in the foreground, droplets d1-d3 and trails t0-t3. Trail t3 comprises etched areas due to droplet d3 and another droplet which has moved out of view. The white steps slightly offset below the upper boundary of trail t3 exemplify the jumpy movements of large droplets discussed in the text. (b) Schematic drawing of the path taken by droplet d1, traced from its current position to its origin O following the trail t1. Along the path, R and L mark right and left turning points, respectively. Each turn results from a dislocation intersection in accordance with Fig. 5(d); thus, it is postulated that d1 is bounded by at least two horizontal (h1-h2 in [110]) and five vertical (v1-v5 in $[1\bar{1}0]$) dislocations. Other dislocations may exist but are not resolved.

For all of the paths, although the droplets are said to thread along the dislocations the centers of the droplets when projected into the substrate do not coincide with the dislocation cores, but shifted sideway by a distance commensurate with the epilayer thickness. For example, the strain profile in Fig. 5(c) indicates that the surface droplets would populate the y position where σ_{zz} is at its maximum, i.e., shifted from the dislocation core ($\perp$) by $y \approx 0.25\ \mu$m. This horizontal offsets have previously been observed in heteroepitaxial growth of QDs on dislocation networks where STM,[43] AFM, and TEM[44] results confirm that QDs are formed on one side of misfit dislocations. The sharp boundary of InAs QDs on only one side of the dislocation lines in Fig. 2(d) is a case in point, but the contrast is not as clear as the atomically resolved results obtained by STM.[43]

C. Unusual droplet motions

The coexistence of the in-plane and out-of-plane forces simultaneously acting on droplets on the surface of structure B gives rise to three motion behaviors or characteristics starkly different from those on flat surfaces.

First, the violation of the trail-avoiding rule. Ga droplets on flat GaAs(001) surfaces always avoid the trails of other droplets. This is due mainly to the chemical potential gradient $\Delta\mu$ between the flat trails and the rough surroundings which always drive droplets toward new grounds. The trail-avoiding rule is observed on many low-index surfaces of GaAs and other III-V compounds.[14–16] On the surface of structure B in Fig. 4(c), however, three droplets (D5-D7) are present on the same [110] dislocation line and two of them (D6, D7) violate the trail-avoiding rule. The current positions of droplets D5-D7 and the trails suggest the chronology schematized in Fig. 5(e): D5 on a $[1\bar{1}0]$ dislocation first goes up the intersection X1 and turns left, then D6 on another $[1\bar{1}0]$ dislocation goes up the intersection X2 and turns left, and finally D7 which nucleated at O moves left toward X2 and passes it. It is clear, in Fig. 4(c), that D6 (D7) does not avoid but run over the trail of D5 (D6). This is partly due to the miscut discussed earlier and partly because D6 and D7 are guided by the [110] dislocation which exert on them a stress-related force F_σ greater than F_μ. Such strong stress may be due to the proximity between the surface and the dislocation, such as when the dislocation lies at the upper interface (GaAs/InGaAs).

Second, the rectangular maze pattern exhibited by a limited number of small droplets. Small droplets do not normally run, but under certain circumstances they do and when they do they reveal a wealth of information unavailable from large running droplets. The reason that small droplets do not normally run is because the driving force varies linearly with diameter[10,12] and on flat GaAs(001) a droplet has to reach a semi-empirically determined critical diameter $D_c \sim 1.9\ \mu$m before running.[45] Some droplets on structure B, in contrast, run even when their diameters are smaller than D_c. Figure 6(a) shows an area having three droplets of various sizes and behaviors on a background of bright Ga nanodroplets and dark trails. The droplet of interest is d1. Its 1-μm diameter is about half of d2 which in turn is about half of d3. But d1 has moved a combined distance of 48 μm (measured from its trail t1, starting from O to its current position), while d2 has moved by only 0.5 μm (from its trail t2). The behavior of d2 is expected since its diameter of $\sim$2 μm just exceeds D_c; thus, it only begins to move. The behavior of d3 is also expected since its size is much larger than D_c and it moves relatively freely. If the driving force depends solely and linearly on D, then d1, being smaller than d2 and particularly D_c, should not have moved. The fact that d1 moves before d2 does indicate that a certain force is acting on d1 but not d2. So, what local force is aiding d1, abetting it to break the minimum D_c threshold?

The answer again lies in the subsurface stress field which gives rise to a force F_σ that not only frees d1 from its nucleation point O, but also guides it throughout. The field is qualitatively similar to Fig. 5(a), but quantitatively different in terms of size, and the number and location of [110] and $[1\bar{1}0]$ dislocations.[46] Specifically, there must be a $[1\bar{1}0]$ dislocation beneath d1 at its origin O, exerting a force F_σ from below, nudging it off its etch pit. This $[1\bar{1}0]$ dislocation is the line v1 in Fig. 6(b). Judging from the trail t1, it is clear that, on moving from O to its present position, d1 takes seven right and two left turns, noted in Fig. 6(b) by R and L, respectively. Each turn marks a dislocation intersection, in accordance with the behavior of a droplet on approaching an intersection as described above and schematized in Fig. 5(d). Thus, it is estimated that at least five vertical (v1-v5) and two horizontal (h1-h2) dislocations exist, bounding d1 as shown in Fig. 6(b). Each segment along the trail is not perfectly straight, indicating that d1's motion is influenced by the background nanodroplets incorporated into d1. The motion of small droplets in general is necessarily jagged as a result of capillarity and merging. Far from dislocations, capillarity dominates and the path is jagged. Close to dislocations, subsurface strain fields dominate and the path is straight. The dominance of the driving subsurface strain field scales with the droplet size. For large droplets, the incorporation of background material constitutes a small percentage increase in mass and hence the trail of a large droplet on a guiding dislocation (t0, for example) is straight. For very large droplets, the percentage increase in mass is negligible but the diameter of the droplet maybe so large that it overlaps many dislocations simultaneously. In other words, large droplets may be guided by many dislocations and intersections and their movements become jumpy when the average line density of dislocations is in the same order of magnitude as the average diameter of droplets. Typically, the trail of a very large droplet such as t3 in Fig. 6(a) consists of multiple straight segments with many jumps (see white steps at the upper boundary of trail t3) dictated by the underlying dislocation network. Thus, large droplets are affected by a large number of dislocations, whereas small droplets are guided by individual dislocations, revealing the details of subsurface stress fields with greater resolution.

Third, the 180° I- and U-turns. The 180° I-turn is so named because a droplet running on a dislocation, especially a [110] direction, heading toward a highly repulsive orthogonal stress wall (hereafter block wall) can bounce back, on its own trail, on the same dislocation. This contradicts with the

path E in Fig. 5(d) and is possible if the plane of the guiding dislocation is so close to the surface that the stress-related attractive force does not let the droplet slip away. Examples of droplets that have made one I-turn are I1 and I2 in Figs. 4(b) and 4(c), respectively. Tersoff *et al.*[10] reported similar 180° I-turn but only after prolonged sublimation that the surface and the trails are both rough, and thus, the reversing droplets are chemical potential driven, not dislocation driven as observed here.

The 180° U-turn is so named because some droplets, upon hitting block walls, bounce back, but this time not on their own trails. In other words, they perform a self-avoiding walk 180° turn. U-turns are most likely observed on large droplets that have moved a significant distance from the nucleating sites. Figure 7(a) shows the SEM image of an area where many droplets move along the [110] principal direction in irregular patterns. Specifically, they wiggle and make U-turns. To better illustrate the dynamics and chronology of the droplets, the SEM image is processed using an edge detection algorithm in ImageJ and the results are shown with pseudocolors and different shades of grey in Fig. 7(b). The resting positions of the droplets are shaded darker than the trails. All droplets wiggle as they run over dislocations and dislocation intersections and as such their paths are affected by the underlying stress fields. The wiggling trails comprise multiple short steps up and down, similar to the trail t3 in Fig. 6(a) and consistent with a dense cross-hatch pattern profile expected of the embedded InGaAs layer.[30] In addition to wiggling, some droplets make U-turns. Of particular interest in Fig. 7(b) are droplets U1, U2, and U3 which make one, two, and three U-turns, respectively.

U-turns are possible under two main circumstances: (i) when a droplet approaches an intersection from a quarter that repels it from all sides, such as from Q1 as shown by path U in Fig. 5(d), and (ii) when a droplet is deflected by a barrier, particularly the trail of other droplets. For U1, no surface irregularity such as a trail is found at the turning point; thus, the cause of the U-turn must be subsurface in origin. This is attributed to the subsurface dislocations v6 and h3, seen superimposed onto the processed SEM image in Fig. 7(b). The presence of h3 is corroborated by the presence of droplet D8, whereas the presence of v6 is corroborated by the effects it has on droplet U3 and the presence of droplet D9 which stuck at the v6-h4 intersection (but has slipped out of view). For U2, the first U-turn is due both to the presence of the block wall v7 and the trail t4. The second U-turn is due to repulsion by the block wall v8. For U3, the first U-turn is due to the block wall v6 and the trail t5; the second and third U-turns are due to the attempt of U3 to avoid the trails t6 and t7 rather than the repulsion by block walls.

All in all, Secs. III B and III C show the various nonlinear motions of surface droplets driven, principally or at least in part, by interfacial misfit dislocation whose presence is clearly visible in various micrographs but whose strain states have so far been ignored.

D. The misfit layers

As high temperatures are necessary to induce surface droplets, the misfit InGaAs layers must somehow be affected. But to what degree? It is important to answer this question as the misfit layers are responsible for the droplets' motion, yet it is unclear whether the forces acting on the droplets are due to the starting misfit dislocation network, or to additional dislocations formed by further strain relaxation during the high-temperature processing.

Three scenarios are plausible. The misfit layers either remain intact, relax further completely, or relax further partially. To evaluate the prevailing scenario, the symmetric (004) HR-XRD is used as a quick check for the integrity of the interfaces, whereas the asymmetric (115) reciprocal space map (RSM) is used to gauge the misfit degree of each structure before and after sublimation. The following discusses XRD spectra of structure A, followed by B.

For structure A (InGaAs/GaAs), the sublimated surface is the misfit InGaAs layer itself. The misfit layer is thus eliminated in the process and should not be detected by XRD. Figure 8(a) shows the (004) rocking curves of the structure before and after sublimation and it is clear that while the substrate peak (GaAs at $2\theta \approx 66°$) remains, the layer peak (InGaAs at $2\theta \approx 64.8°$) disappears after sublimation. The quality of the Pendellösung fringes of the structure before sublimation is not high since only the bottom interface (InGaAs/GaAs) is atomically sharp but the top interface (air/InGaAs) is not. The GaAs peak is not as sharp as those that might be expected of single-crystal GaAs substrates because the peak results from the starting substrate and a 300-nm GaAs smoothening layer grown immediately before the InGaAs layer.

For structure B (GaAs/InGaAs/GaAs), the sublimated surface is the GaAs layer. The sublimated thickness is estimated from the etch depth of the trail as measured by AFM

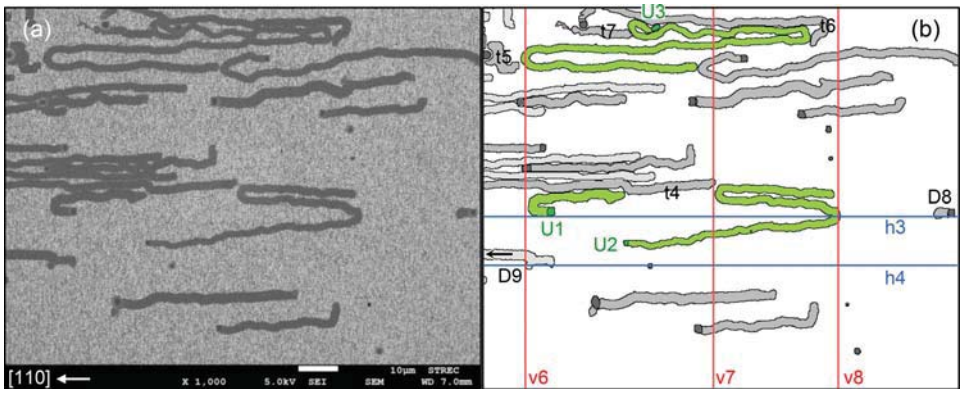

FIG. 7. Droplets wiggle and U-turn, as observed on the post-sublimated surface of structure B. (a) The original SEM image. (b) The processed image highlighting the droplets U1-U3 and trails t4-t7. In running from the starting to the current positions, U1, U2, and U3 take one, two, and three U-turns, respectively, in addition to the wiggling motion. Each U-turn results from droplet interaction with either a block wall (v6-v8), or a trail (t4-t7), or both.

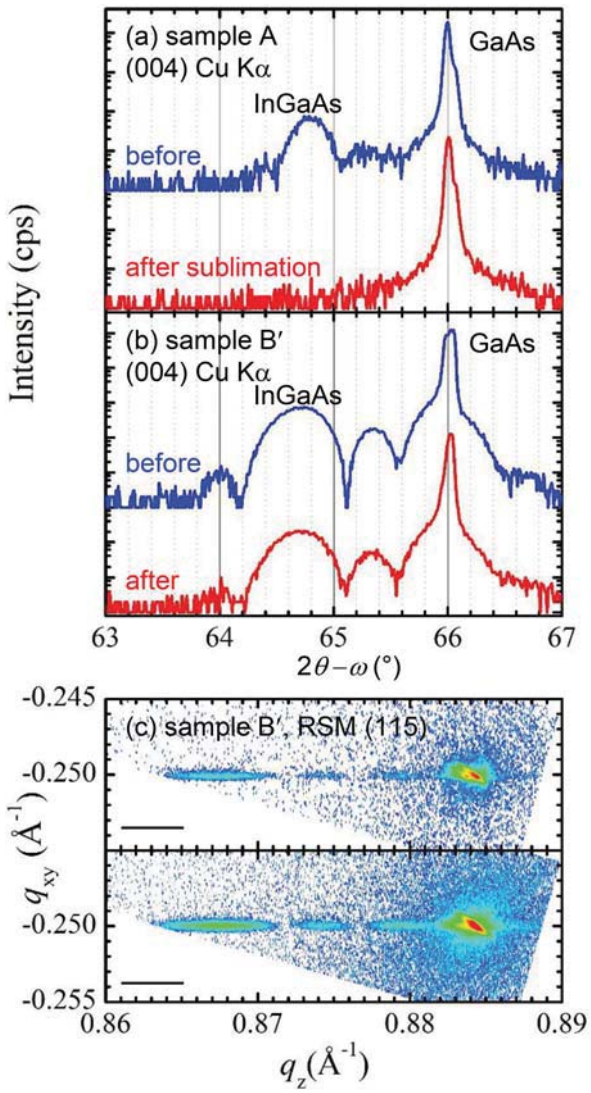

FIG. 8. XRD spectra of the misfit layers. (004) rocking curves of structure (a) A or 40-nm $In_{0.15}Ga_{0.85}As$/GaAs and (b) B′ or 350-nm GaAs/25-nm $In_{0.2}Ga_{0.8}As$/GaAs before (blue, upper curves) and after (red, lower curves) the sublimation of the top layer. Curves are offset for clarity. (c) (115) reciprocal space maps of structure B′ before (upper) and after (lower) sublimation. The scale bars are 0.004 Å^{-1}.

to be 50 nm, much thinner than the 400-nm GaAs layer. The thickness of the underlying InGaAs layer is thus unaffected. Figure 8(b) shows the (004) rocking curve of a slightly different structure B′, similar to B, before and after sublimation. The only difference between B′ and B is that the thickness of the top GaAs surface in B′ is 350 nm, as opposed to 400 nm in B. Both structures are subject to the same sublimation and the droplet dynamics are qualitatively the same. Since the thickness of GaAs in B′ is thinner, the embedded InGaAs layer in B′, particularly the upper interface (GaAs/InGaAs), would deteriorate faster than those in B. Figure 8(b) however shows that after the sublimation and despite the slight decrease in thickness, the substrate and the layer peaks remain practically unchanged. Apart from a slight reduction in overall intensity (due to the presence of surface Ga droplets), both the peak positions and the quality of the Pendellösung fringes remain intact, indicating that the upper and lower interfaces of the buried misfit layer are not affected by the sublimation. The (115) reciprocal space maps of structure B′ before and after sublimation as shown in Fig. 8(c) provide further proof that the integrity of the misfit layers remains intact.

As the buried misfit layer does not undergo further relaxation during the sublimation of the surface, it is thus conclusive that the preferential nucleation of droplets in Sec. III A and the guiding and blocking of running droplets in Sec. III B arise from the starting misfit dislocation network.

IV. CONCLUSION

GaAs/InGaAs/GaAs structures grown by molecular beam epitaxy are sublimated in vacuum and the resulting morphological changes are observed *in situ* via low-energy electron microscopy. Initially, the disproportionate loss of group-V atoms results in the formation of group-III droplets which preferentially nucleate on the surface immediately above dislocations, aided by the dislocation-related stress fields. Later, the droplets grow and run in two principal directions, [110] and [1$\bar{1}$0], as they are guided by the same stress fields. Small droplets are guided by individual dislocations. Large droplets are affected by several dislocations and intersections. This gives small droplets the ability to probe the presence of subsurface dislocations at greater resolution than large droplets. In the end, all running droplets will approach intersections with insurmountable repulsive stress walls and respond by abruptly changing paths, for example, by taking 90° turns, or by bouncing off the stress barriers, returning to their own trails (I-turn) or veering off slightly (U-turn). Abrupt 90° and 180° turns for liquid flowing on flat surfaces are unusual and demonstrate new avenues of applications that employ defects to do mechanical work. X-ray diffractions reveal that the misfit InGaAs layers are unaffected during sublimation, suggesting that the predesigned misfit dislocation network (and their associated stress fields) can be used to steer surface droplets, which would be of great utility in droplet-based growth and fabrication of optoelectronic devices. As a possible extension of this work in other fields, we speculate that the defect-liquid flow relationships established here maybe applicable in a wider range of systems and in a broader context of shear-flow aero- or hydrodynamics. For example, a properly designed dislocation network on a landscape (seafloor) should be able to redirect or reverse the overflowing air (waves).

ACKNOWLEDGMENTS

Generous access to Elmitec's LEEM III system at Beamline 3.2Ub of the Synchrotron Light Research Institute (SLRI), to Rigaku's TTRAX III diffractometer at MTEC, and technical support from W. Busayaporn, C. Euaruksakul, S. Sopitpan, and S. Thainoi are gratefully acknowledged. This work was financially supported by AFOSR/AOARD (Grant No. FA2386-16-1-4003), NSTDA Research Chair Grant (No. FDA-CO-2558-1407-TH), Chulalongkorn University, SLRI, and Thailand Research Fund (RSA5880049).

[1]M. D. Dickey, Adv. Mater. **29**, 1606425 (2017).
[2]J. Wu and Zh. M. Wang, J. Phys. D: Appl. Phys. **47**, 173001 (2014).

[3]S. Sanguinetti, N. Koguchi, T. Mano, and T. Kuroda, J. Nanoelectron. Optoelectron. **6**, 34 (2011).
[4]N. Koguchi, S. Takahashi, and T. Chikyow, J. Cryst. Growth **111**, 688 (1991).
[5]Zh. M. Wang, B. L. Liang, K. A. Sablon, and G. J. Salamo, Appl. Phys. Lett. **90**, 113120 (2007).
[6]C. Heyn, Phys. Rev. B **83**, 165302 (2011).
[7]A. Fontcuberta i Morral, C. Colombo, G. Abstreiter, J. Arbiol, and J. R. Morante, Appl. Phys. Lett. **92**, 063112 (2008).
[8]B. Mandl, J. Stangl, E. Hilner, A. A. Zakharov, K. Hillerich, A. W. Dey, L. Samuelson, G. Bauer, K. Deppert, and A. Mikkelsen, Nano Lett. **10**, 4443 (2010).
[9]M. Schvartzman, D. Tsivion, D. Mahalu, O. Raslin, and E. Joselevich, Proc. Natl. Acad. Sci. U.S.A. **110**, 15195 (2013).
[10]J. Tersoff, D. E. Jesson, and W. X. Tang, Science **324**, 236 (2009).
[11]C. C. Maass, C. Krüger, S. Herminghaus, and C. Bahr, Annu. Rev. Condens. Matter Phys. **7**, 171 (2016).
[12]E. Hilner, A. A. Zakharov, K. Schulte, P. Kratzer, J. N. Andersen, E. Lundgren, and A. Mikkelsen, Nano Lett. **9**, 2710 (2009).
[13]M. Dąbrowski, Y. Dai, M. Hocevar, S. Frolov, and H. Petek, Appl. Phys. Lett. **109**, 261602 (2016).
[14]S. Kanjanachuchai and C. Euaruksakul, ACS Appl. Mater. Interfaces **5**, 7709 (2013).
[15]S. Kanjanachuchai and C. Euaruksakul, Cryst. Growth Des. **14**, 830 (2014).
[16]S. Kanjanachuchai and P. Photongkam, Cryst. Growth Des. **15**, 14 (2015).
[17]S. Kanjanachuchai and P. Photongkam, Cryst. Growth Des. **17**, 4413 (2017).
[18]B. Nikoobakht, A. Herzing, S. Muramoto, and J. Tersoff, Nano Lett. **15**, 8360 (2015).
[19]S. Curiotto, F. Leroy, F. Cheynis, and P. Müller, Sci. Rep. **7**, 902 (2017).
[20]Y. Cui, D. Li, and H. Bai, Ind. Eng. Chem. Res. **56**, 4887 (2017).
[21]M. Gad-el-Hak, Appl. Mech. Rev. **49**, 365 (1996).
[22]S. Kanjanachuchai, M. Maitreeboriraks, C. C. Thet, T. Limwongse, and S. Panyakeow, Microelectron. Eng. **86**, 844 (2009).
[23]P. Bhattacharya, *Properties of Lattice-Matched and Strained Indium Gallium Arsenide* (INSPEC, London, 1993).
[24]M. Yano, H. Yokose, Y. Iwai, and M. Inoue, J. Cryst. Growth **111**, 609 (1991).
[25]D. Hull and D. J. Bacon, *Introduction to Dislocations*, 5th ed. (Butterworth-Heinemann, Oxford, 2011).
[26]J. Tersoff, D. E. Jesson, and W. X. Tang, Phys. Rev. Lett. **105**, 035702 (2010).
[27]T. Limwongse, S. Panyakeow, and S. Kanjanachuchai, Phys. Status Solidi C **6**, 806 (2009).
[28]A. N. Alexeev, S. Yu Karpov, M. A. Maiorov, V. E. Myachin, Yu V. Pogorelsky, and I. A. Sokolov, J. Cryst. Growth **166**, 167 (1996).
[29]F. Leroy, Ł. Borowik, F. Cheynis, Y. Almadori, S. Curiotto, M. Trautmann, J. C. Barbé, and P. Müller, Surf. Sci. Rep. **71**, 391 (2016).
[30]C. C. Thet, S. Sanorpim, S. Panyakeow, and S. Kanjanachuchai, Semicond. Sci. Technol. **23**, 055007 (2008).
[31]W. Eiwwongcharoen, N. Nakareseisoon, S. Thainoi, S. Panyakeow, and S. Kanjanachuchai, CrystEngComm **18**, 5852 (2016).
[32]E. Penev, P. Kratzer, and M. Scheffler, Phys. Rev. B **64**, 085401 (2001).
[33]M. Rosini, P. Kratzer, and R. Magri, J. Phys. Condens. Matter **21**, 355007 (2009).
[34]K. Takahashi, H. Kawada, S. Ueda, M. Furuse, and S. Shirayone, J. Vac. Sci. Technol. A **9**, 854 (1991).
[35]K. Shorlin and M. Zinke-Allmang, Surf. Sci. **601**, 2438 (2007).
[36]J. Wu, Zh. M. Wang, A. Z. Li, M. Benamara, and G. J. Salamo, ACS Appl. Mater. Interfaces **3**, 1817 (2011).
[37]S. S. Datta, J. Appl. Phys. **108**, 024307 (2010).
[38]C. Zheng, W. X. Tang, and D. E. Jesson, J. Vac. Sci. Technol. A **34**, 043201 (2016).
[39]S. Curiotto, F. Leroy, F. Cheynis, and P. Müller, Surf. Sci. **632**, 1 (2015).
[40]J. E. Ayers, *Heteroepitaxy of Semiconductors: Theory, Growth, and Characterization* (CRC Press, Boca Raton, 2007).
[41]A. M. Andrews, R. LeSar, M. A. Kerner, J. S. Speck, A. E. Romanov, A. L. Kolesnikova, M. Bobeth, and W. Pompe, J. Appl. Phys. **95**, 6032 (2004).
[42]F. Brochard, Langmuir **5**, 432 (1989).
[43]A. Ohtake and N. Koguchi, Appl. Phys. Lett. **89**, 083108 (2006).
[44]S. Y. Shiryaev, F. Jensen, J. L. Hansen, J. W. Petersen, and A. N. Larsen, Phys. Rev. Lett. **78**, 503 (1997).
[45]J. Wu, Zh. M. Wang, A. Z. Li, M. Benamara, J. Lee, S. D. Koukourinkova, E. S. Kim, and G. J. Salamo, J. Appl. Phys. **112**, 043523 (2012).
[46]S. Kanjanachuchai and T. Limwongse, J. Nanosci. Nanotechnol. **11**, 10787 (2011).